UNIVERSITÀ DEGLI STUDI DI PADOVA

EUV Experimental Physics of Extreme Ultraviolet

RWTH AACHEN UNIVERSITY

Sede Amministrativa: Università degli Studi di Padova

Consiglio nazionale delle ricerche, Istituto di Fotonica e Nanotecnologie (CNR-IFN), Padova

---

Dipartimento di Ingegneria dell'Informazione

Faculty of Mathematics, Computer Science and Natural Sciences

SCUOLA DI DOTTORATO DI RICERCA IN: Ingegneria dell'Informazione

INDIRIZZO: Scienza e Ingegneria dell'Informazione

CICLO: XXXI

TESI IN COTUTELA

Design, development, and characterization of thin-film filters for high brilliance sources in the EUV-soft x-ray spectral range

Direttore della Scuola: Ch.mo Prof. Andrea Neviani

Coordinatore d'indirizzo: Ch.mo Prof. Andrea Neviani

Supervisore: Ch.mo Prof. Piergiorgio Nicolosi

Supervisore: Chiar.mo Prof. Dr.rer.nat. Joachim Mayer

Dottoranda: Kety Mayelin Jimenez Tejeda

2019

Design, development, and characterization of thin-film filters for high brilliance sources in the EUV-soft x-ray spectral range

Von der Fakultät für Mathematik, Informatik und Naturwissenschaften der RWTH Aachen University zur Erlangung des akademischen Grades eines Doktors der Naturwissenschaften genehmigte Dissertation

vorgelegt von

Kety Mayelin, Jimenez Tejeda; M.Sc.

aus

Santo Domingo, Dominikanische Republik

Berichter: Univ.-Prof. Dr. rer. nat. Joachim Mayer

Prof. Dr. Piergiorgio Nicolosi

Dr. Larissa Juschkin

Tag der mündlichen Prüfung: 11.12.2019

UNIVERSITÀ DEGLI STUDI DI PADOVA

RWTH AACHEN UNIVERSITY

DESIGN, DEVELOPMENT, AND CHARACTERIZATION OF THIN-FILM FILTERS FOR HIGH BRILLIANCE SOURCES IN THE EUV-SOFT X-RAY SPECTRAL RANGE

Ph.D. Thesis by:

Kety Mayelin Jiménez Tejeda

A thesis presented for the degree of

Erasmus Mundus Joint Doctorate, EXTATIC

To the:

Faculty of Mathematics, Computer Science and Natural Sciences

RWTH Aachen, Germany

and

Department of Information Engineering

University of Padova, Italy

Supervisors: *Prof. Piergiorgio Nicolosi, Prof. Joachim Mayer.*

Abstract.

This thesis addresses research works on the design, fabrication development, and characterization of thin-film transmittance filters for high brilliance sources in the Extreme Ultraviolet (EUV) and soft X-ray spectral regions. The development and fabrication of thin-film filters for extreme ultraviolet (EUV) and soft x-ray high brilliance sources are strongly required in many applications. In the case of third and fourth generation light sources, high order harmonic generation (HHG) sources, the extreme ultraviolet (EUV) and soft x-ray thin-film filters are used to remove multiple-order radiation. Furthermore, those filters must be suited to face the high peak power of these kinds of sources.

In the EUV and soft-X ray spectral range region materials have high absorption, so finding proper materials or combinations of materials that fulfill the requirements of the filters is quite challenging. Using simulations of the transmittance performance of a variety of materials, based on the theoretical values of their optical constants, and taking in account their mechanical properties, Nb and Zr were chosen as core elements for the fabrication and study of free-standing filters.

The first development part of this thesis is focused on the bottom-up fabrication technique of Nb, Zr, Nb/Zr, and Zr/Nb thin films of 100 nm thickness, deposited on silicon nitrate membrane windows by magnetron sputtering technique, pursuing to achieve free-standing filter after reactive ion etching of the membrane; Nb and Nb/Zr free-standing filters were produced. These samples were characterized using Rutherford backscattering, AFM images, and transmittance characterization in the EUV between 4-20 nm using synchrotron radiation at the Bear Beamline, ELETTRA, Italy and in Optical Beamline at BESSY synchrotron, Berlin, Germany. Also, the samples were characterized in the same range using a plasma source based on puff gas target as a secondary technique of transmittance characterization.

The second part is the structural characterization of the filters using TEM, SEM, HRSTEM, and EDX analysis.

The third development part of this thesis is focused on the study of high-intensity EUV radiation damage of Nb, Zr, Zr/Nb, and Nb/Zr 100 nm thick free-standing filters. For this part of the experiment, the samples were deposited on silicon nitride windows using e-beam deposition technique, showing more stable structures, free-standing filters of each type were achieved after reactive ion etching. Samples were characterized before and after exposure using X-ray photoelectron spectroscopy (XPS) technique, AFM images, X-ray diffraction technique, and transmittance characterization in the EUV spectral range performed with synchrotron radiation at Bear Beamline. For radiation exposure, a high peak intensity set-up based on a plasma discharge source was used at 13.5 nm wavelength. Also, transmission electron microscopy and scanning electron microscopy characterization were used as complementary techniques to study the sample's structures and interface properties.

Abstrakt.

Die vorliegende Dissertation befasst sich mit den wissenschaftlichen Daten zum Design, zur Herstellungsentwicklung und zur Charakterisierung von Dünnschichttransmissionsfiltern für Quellen mit hoher Brillanz im extremen Ultraviolett (EUV) und im weichen Röntgenspektralbereich. Die Entwicklung und Herstellung von Dünnfilmfiltern für extrem ultraviolette (EUV) und weiche Röntgenquellen mit hoher Brillanz sind in vielen Anwendungen dringend erforderlich.

Im Fall der dritten und vierten Generation werden Lichtquellen, Quellen zur Erzeugung von Harmonischen hoher Ordnung (HHG), Dünnfilmfilter für extrem ultraviolettes Licht (EUV) und weiche Röntgenstrahlen verwendet, um Strahlung mehrfacher Ordnung zu entfernen. Darüber hinaus müssen diese Filter für die hohe Spitzenleistung dieser Art von Quellen geeignet sein. Materialien im EUV- und im weichen Röntgenspektralbereich weisen eine hohe Absorption auf. Daher ist es eine große Herausforderung, geeignete Materialien oder Materialkombinationen zu finden, die die Anforderungen der Filter erfüllen. Unter Verwendung von Simulationen des Transmissionsvermögens einer Vielzahl von Materialien, basierend auf den theoretischen Werten ihrer optischen Konstanten und unter Berücksichtigung ihrer mechanischen Eigenschaften, wurden Nb und Zr als Kernelemente für die Herstellung und Untersuchung von freistehenden Filtern ausgewählt.

Der erste Teil dieser Arbeit befasst sich mit der Bottom-up-Herstellungstechnik von 100 nm dicken, Dünnfilmen aus Nb, Zr, Nb / Zr und Zr / Nb, die durch Magnetron-Sputtern auf Siliziumnitrat- Membranfenstern abgeschieden wurden. Nach reaktivem Ionentiefenätzen wurden freistehende Nb- und Nb / Zr-Filter erhalten. Diese Proben wurden mittels Rutherford-Rückstreuung, AFM-Bildern und Transmissionscharakterisierung im EUV zwischen 4 und 20 nm unter Verwendung von Synchrotronstrahlung (Bear Beamline, ELETTRA, Italien; Optical Beamline, BESSY Synchrotron, Berlin, Deutschland) charakterisiert. Dieselben Proben wurden im gleichen nm Bereich unter Verwendung einer Plasmaquelle, basierend auf ein Puffgas-Target, als sekundäres Verfahren zur Transmissionscharakterisierung, charakterisiert.

Der zweite Teil dieser Arbeit befasst sich mit der strukturellen Charakterisierung der Filter mittels TEM-Analyse.

Der dritte Entwicklungsteil dieser Arbeit befasst sich mit der Untersuchung von Schäden an 100 nm dicken freistehenden Nb-, Zr-, Zr / Nb- und Nb / Zr-Filtern verursacht durch EUV-Strahlen hoher Intensität. Für diesen Teil des Versuchs wurden Probe auf ein Siliziumnitritfenster unter Verwendung der Elektronenstrahl-Abscheidungstechnik abgeschieden, die stabilere Strukturen aufwiesen. Nach reaktiven Ionentiefenätzen wurden freistehende Filter jedes Typs erhalten. Die Proben wurden vor und nach Bestrahlung mittels Röntgenphotonenspektroskopie (XPS), AFM-Bildern, Röntgenbeugungstechnik und Transmissionscharakterisierung im EUV-Spektralbereich mit Synchrotronstrahlung (Bear Beamline, Italy) charakterisiert. Für die Bestrahlungsaussetzung

wurde ein hochdichte Aufbau in einer Plasmaentladungsquelle bei einer Wellenlänge von 13,5 nm verwendet. Transmissionselektronenmikroskopie und rasterelektronenmikroskopische Charakterisierung wurden ebenfalls als komplementäre Techniken zur Untersuchung der Probenstrukturen und Grenzflächeneigenschaften verwendet.

Sommario.

La tesi presenta un lavoro di ricerca svolto sulla progettazione, lo sviluppo della fabbricazione e la caratterizzazione di filtri a membrana sottile per la trasmissione di fonti di alta luminosità nelle regioni spettrali dell'ultravioletto estremo (EUV) e dei raggi x molli. Lo sviluppo e la fabbricazione di filtri a membrana sottile per le fonti di alta luminosità nelle regioni spettrali dell'ultravioletto estremo (EUV) e dei raggi x molli è fortemente richiesto in molte applicazioni. Nel caso delle fonti di alta luminosità di terza e quarta generazione, ovvero la generazione di fonti di armoniche di alto livello (HHG), sono richiesti filtri a membrana sottile per l'ultravioletto estremo (EUV) e i raggi x molli per rimuovere radiazioni di ordine multiplo. Inoltre, questi filtri devono essere adatti per affrontare la potenza di alto picco proveniente da questo tipo di fonti.

Nella regione del campo spettrale delle fonti di armoniche di alto livello (HHG) e l'ultravioletto estremo (EUV) i materiali hanno alto assorbimento, pertanto trovare materiali adatti o combinazioni di materiali che soddisfano i requisiti dei filtri è molto impegnativo. Utilizzando simulazioni sulla prestazione della trasmissione di una varietà di materiali, basate sui valori teorici delle loro costanti ottime, e considerando le loro proprietà meccaniche, sono stati scelti il Nb e il Zr come elementi base per la fabbricazione e studio di filtri indipendenti.

La prima parte dello sviluppo di questa tesi si concentra sulla tecnica di fabbricazione bottom-up di filtri a membrana sottile di Nb, Zr, Nb/Zr e Zr/Nb con spessore di 100 nm depositati su finestre di membrane di nitruro di silicio tramite la tecnica della polverizzazione catodica (Magnetron sputtering), con l'obiettivo di ottenere un filtro indipendente in seguito alla collisione con ioni reattivi; sono stati ottenuti filtri indipendenti di Nb e Nb/Zr. Questi campioni sono stati caratterizzati usando la tecnica del backscattering di Rutherford, immagini AFM e la caratterizzazione della trasmittanza nell'ultravioletto estremo (EUV) nell'intervallo 4-20 nm utilizzando radiazioni del sincrotrone al Bear Beamline, ELETTRA, in Italia e l'Optical Beamile e del sincrotrone BESSY, a Berlino, in Germania. Inoltre, i campioni sono stati caratterizzati nella stessa gamma utilizzando un bersaglio gass puff e una fonte di plasma come tecnica secondaria per la caratterizzazione della transmittanza.

La seconda parte correspode alla characterizazione structurale dei filtri utilizando TEM, SEM, HRSTEM and EDX Analisis.

La terza parte dello sviluppo di questa tesi si concentra sullo studio dei danni delle radiazioni dell'ultravioletto estremo (EUV) ad alta densità di Nb, Zr, Zr/Nb e Nb/Zr dei filtri indipendenti con spessore da 100nm. Per questa parte dell'esperimento i campioni sono stati depositati su finestre di membrane di nitruro di silicio usando la tecnica di deposizione e-beam, mostrando strutture più stabili, sono stati prodotti free standing filtri per ciascun tipo in seguito alla collisione con ioni reattivi (RIE). I campioni sono stati caratterizzati prima e dopo l'esposizione usando la tecnica fotoelettronica a raggi x (XPS), immagini AFM, la tecnica di diffrazione a raggi x e la caratterizzazione della trasmissione nel raggio spettrale dell'ultravioletto estremo

(EUV) fatta usando le radiazioni del sincrotrone al Bear Beamline. Per l'esposizione alle radiazioni è stata usata una configurazione di base ad alta densità in una fonte di scarica al plasma a lunghezza d'onda di 13.5 nm. Inoltre, sono stati usati un microscopio elettronico a trasmissione e la scansione microspia elettronica come tecniche complementari per studiare la struttura dei campioni e le proprietà dell'interfaccia.

Acknowledgment.

Firstly, I would like to express a sincere and deepest gratitude to my advisors Prof. Piergiorgio Nicolosi, Prof. Larissa Juschkin, and Prof. Joachim Mayer for their support and guidance during the Ph.D. study and related research, for their immense patience, constant motivation, and vast knowledge. Besides my official advisors, I would like to sincerely thank Dr. Paola Zuppella for her continuous and dedicated support during these three years and for always having kind words to keep me going.

The author wishes to thank Dr. Serhiy Danylyuk and all colleagues from ILT Institute, RWTH Aachen University, and the Juelich Forschungszentrum, for giving me the opportunity to work in their labs and for all the knowledge passed to me during the mobility period. Of course, immense gratitude to the administrative staff of the department of information engineering (DEI Padova) and Juelich Forschungszentrum. An enormous thanks to Marta Lipinska and Maximilian Kruth from the Ernst Ruska-Center (ER-C), for all the help received from both of you with the TEM measurements and analysis.

I thank my fellow partner in the EXTATIC program for having insightful discussions during the welcome weeks and conferences, especially to my direct colleagues from the program: Mewael Sertsu, Ahmed Gaballah, and Nadeem Ahmed for their support and friendships.

Furthermore, I also like to extend the acknowledgments to the financial support from The Education, Audiovisual, and Culture Executive Agency (EACEA), Erasmus Mundus Joint Doctorate, EXTATIC Program under framework partnership Agreement No. 2012-0033.

Finally, I would like to divide the dedication of this thesis into two families:

To my family, who during all my years of studies have been near me, in heart to keep me going and encourage me to achieve my goals; principally to my dear sister Patricia who always knows the precise words to motivate me.

To the Serbanoiu Family, they took me as part of their own during these years, showing me kindness and love, especially to my dear friend Dan who introduced me to the whole family. I am very grateful to all of you; you kept my heart warm during the cold weather and the distance from my own family.

Publications and Conference Presentations.

Publications during the Ph.D. program.

1. **K. Jimenez**, P. Nicolosi, L. Juschkin, N. Ahmed, A. E. H. Gaballah, E. Cattaruzza, M. G. Sertsu, A. Gerardino, A. Giglia, G. Mussler, P. Zuppella. "EUV free-standing transmittance filters, for high brilliance sources, based on Nb/Zr and Zr/Nb thin films on Si3N4 membranes; Design, fabrication, optical and structural characterization. Thin Solid Films, ISSN: 0040-6090, Vol: 695, Page: 137739, (2020). https://doi.org/10.1016/j.tsf.2019.137739
2. **K. Jimenez**, A. E. H. Gaballah, N. Ahmed, P. Zuppella, P.Nicolosi. "Optical and structural characterization of Nb, Zr, Nb/Zr, Zr/Nb thin films on Si3N4 membranes windows." SPIE Proc. 10236, Damage to VUV, EUV, and X-ray Optics (2017).
3. A. E. H. Gaballah, P. Zuppella, N. Ahmed, **K. Jimenez**, G. Pettinari, A. Gerardino, P. Nicolosi. "A tabletop polarimetric facility for the EUV spectral range: implementations and characterization." Proc. 10235, UV and X-ray Optics: Synergy between Laboratory and Space (2017).
4. A. E. H. Gaballah, P. Nicolosi, N. Ahmed, **K. Jimenez**, G. Pettinari, A. Gerardino, P. Zuppella. "EUV polarimetry for thin film and surface characterization and EUV phase retarder reflector development." Rev. Sci. Instrum. 89, 015108, (2018).
5. A. E. H. Gaballah, P. Nicolosi, P. Zuppella, N. Ahmed, **K. Jimenez**, G. Pettinari, A. Gerardino, P. Nicolosi. "Vacuum ultraviolet quarter wave plates based on SnTe/Al bilayer: design, fabrication and ellipsometric characterization." Appl. Surf. Sci. 463 (2018) 75–81. doi:10.1016/j.apsusc.2018.08.190.
6. N. Ahmed, P. Nicolosi, A. E. H. Gaballah, **K. Jimenez**, P. Zuppella "EUV reflective ellipsometry in laboratory: determination of the optical constants and phase retarder properties of at hydrogen Lyman-alpha." Submitted to Materials Research Express.

I. Other publications by Author.

1. **K. Jimenez**, J. Luciano, S. Rodriguez, O. Vega, F. Torres, C. Laboy, J. Santana & Luis G. Rosa. Surface Shearing Effects on Langmuir–Blodgett Thin Films of P(VDF-TrFE) Ferroelectric Surface, Ferroelectrics, 482:1, 3445, (2015). DOI: 10.1080/00150193.2015.1056699.

II. Presentations at Conferences and Workshops.

- EXTATIC Welcome Week **(workshop)**, 11-15 January 2016 at University of Southampton, UK. Design, Development, and characterization of thin-film filters for high brilliance sources in the UV-X-ray Spectral range. (**Oral presentation**).
- *Design, Development, and characterization of thin-film filters for high brilliance sources in the UV-X-ray Spectral range.* PXRNMS 2016, Multilayer-**workshop** 2016 (TNW), November 2016, Twente University, Twente, Holand. **(Poster presentation)**.
- Training and measurements (**workshop**) in Bear Beamline at Elettra Synchrotron, Trieste; November 2016.
- *Optical and structural characterization of Nb, Zr, Nb/Zr, Zr/Nb thin films on Si3N4*, SPIE Optics + Optoelectronics, April 2017, Prague, Czech Republic. **(Poster presentation).**
- Extatic Welcome Week (**workshop**), 16-20 January 2017 at the International Centre for Theoretical Physics in Trieste, Italy. *Optical and structural characterization of Nb, Zr, Nb/Zr thin films on Si_3N_4 membranes windows*. (**Oral Presentation**).
- Final EXTATIC welcome week **(workshop)**. 2017, CTU Prague. Oral presentation "*Optical and Structural Characterization of Nb, Zr, Nb/Zr, Zr/Nb Thin Films on Si3N4 Membranes Windows".* (**Oral Presentation**).
- 3rd International Workshop on Frontiers of X&XUV Optics and its Applications. October 4-6/ 2017. Prague, Czech Republic. "*Optical and Structural Characterization of Nb, Zr, Nb/Zr, Zr/Nb Thin Films on Si3N4 Membranes Windows"* (**Poster Presentation).**
- PTB's 304. Seminar "VUV and EUV Metrology. Helmholtz-Building of the Berlin-Charlottenburg campus site of PTB. Abbestr. 2-12, 10587 Berlin. "*Optical Characterization of Nb, Zr, Nb/Zr, Zr/Nb thin films for transmittance filters application."* **(Poster Presentation)** 2017.
- Training and Transmittance Characterization **(workshop)** at BEAR beamline, ELETTRA synchrotron 2018.

Acronyms.

UV	Ultraviolet
EUV	Extreme Ultraviolet
XRR	X-ray reflection
ML	Multilayer
EUVL	EUV lithography
GI-EUVR	Grazing incidence EUV reflection
BEAR	Bending magnet for Emission, Absorption, and Reflectivity
SR	Synchrotron Radiation
FELs	Free electron lasers
RF	Radiofrequency
DC	Direct current
E-beam	Electron beam
PVD	Physical Vapor Deposition
AFM	Atomic force microscopy
TEM	Transmission electron microscopy
SEM	Scanning electron microscopy
STEM	Scanning Transmission microscopy
HAADF	High angle annular dark-field
HRTEM	High-resolution transmission microscopy
SADP	Selected Area Diffraction Pattern
BF	Bright field
keV	Kilo electron volt
GDP	Gas Discharge plasma
Bcc	Body-centered cubic
Fcc	Face-centered cubic

Hcp	Hexagonal closest packed
HHG	High harmonic generation
RIE	Reactive Ion Etching
FIB	Focused Ion Beam
XPS	X-ray Photoelectron Spectroscopy

Contents.

Chapter 1.

Introduction.

1.1 Motivation.

The development and fabrication of thin-film filters for extreme ultraviolet (EUV) high brilliance sources is strongly required in many applications. In the case of free-electron laser (FELs), one of the critical technical problems is related to the rejection of higher harmonics, seed laser, first stage photons, and diffuse light [1-7]. Let's take one example of a FELs facility: FERMI.

FERMI is the free-electron laser located at ELETTRA synchrotron scientific campus in Trieste, Italy. The full FERMI facility consists of a linear accelerator plus two principal FEL beamlines in an experimental hall in the complex environment of a multi-beamline user facility provided by the Elettra synchrotron light source. FERMI is based on a seeded source. The FERMI facility comprises two separate coherent radiation sources, FEL-1 and FEL-2. FEL-1 operates in the wavelength range between 100 and 20 nm via a single cascade harmonic generation, while the FEL-2 line operates at shorter wavelengths (20-4 nm) via a double cascade mechanism [8-9]. In FEL-1, an initial signal, seeded by a high peak power pulsed laser operating a certain wavelength region at the electron bunches repetition frequency, passes through a first undulator magnet called modulator to overlap the electron beam. Then after the laser field modulates the electron bunch energies at its frequency, the electrons go through a disperse section where the modulation is converted into bunch charge spatial modulation. Finally, an intense coherent FEL radiation, at the frequency of one of the higher harmonics of the seed laser wavelength contained in the frequency spectrum of those charges modulated electron bunch, can be obtained by passing the modulated bunch through a second set of undulators called "radiator", tuned to select and amplify the chosen harmonic; The complete system it refers to one cascade mechanism.

For the FEL-2 beamline to reach the shortest foreseen design wavelength of 10 nm, a second undulator stage must be added to a first stage similar to FEL-1, consisting of a modulator plus a dispersive section plus a radiator, tuned to and seeded by the first stage output radiation [8]; this is what it means double cascade mechanism**.**

In FERMI as in others FELs facilities with similar technology, the light at the selected wavelength that reach the experimental chamber is mixed with a small fraction of the seed photons. Furthermore, in the case of double cascade sources, the radiation is also combined with photons from the first stage and with a fraction of the higher harmonics, so transmittance filters (bandpass filters) must be introduced to ensure the specific wavelength range that the experiment demands and to improve the quality of the beam delivered by these sources [8, 9]. *In figure 1.1* a schematic design of the FERMI sources, FEL-1 and FEL-2 light delivered system is shown. We can observe

some aluminum filters placed in different points of the light path together with other optical systems, in order to ensure desired properties of the beam delivered.

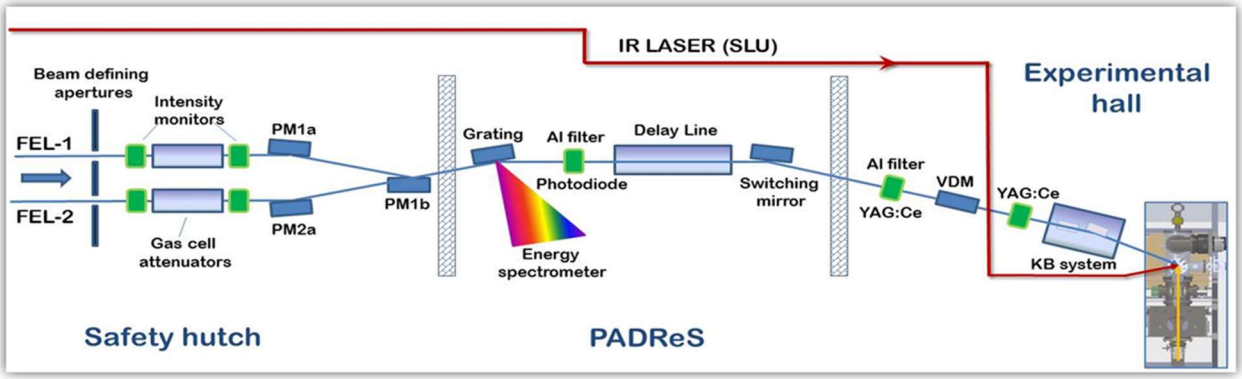

Figure 0.1: *Schematic representation of the FEL light delivery system. Photons are delivered to the end-station through the PADReS (Photon Analysis, Delivery, and Reduction System) [9]. Transmittance filters are placed in different strategic points to ensure the quality of the beam delivered.*

In several applications requiring high-brilliance sources, thin-film filters for extreme ultraviolet and soft x-ray photons are used to remove higher-order radiations and are suited to face a high peak power of around 1-5 GW and a fluence associated to pulses of about 100 femtoseconds. They are also often used as gas barriers; in this case, the filters could interact with contaminant gases that can react with their surface causing damage or affecting their performance [10-13]. For these reasons, the material selected for the fabrication of the filters should be highly resistant, both chemically and structurally, to high power radiation. Thin-film filters are applied in other fields like EUV lithography and spectroscopy; for space experiments where they are used to select suitable spectral bands where spectral emission lines are used to derive the plasma's physical parameters, through spectroscopic diagnostic techniques [14-17].

Since materials have high absorption in the EUV spectral range, filters must be very thin to achieve good transmittance performances, so, considering their optical, chemical, and mechanical properties only a few materials demonstrate to be good candidates for transmittance filters. We are particularly interested in thin-film transmittance filters for the spectral range between 4-20 nm, which is the range covered by FEL 2. Materials as Beryllium and some Rare Earth elements are suggested to be good candidates for transmittance filters in this range, but the toxicity of rare Earth materials makes complicated and dangerous the fabrication of such filters. Combination of metal materials in the form of bilayers or multilayer filters have been presented before for the EUV region, most of them supported by metal mesh but also some fabricated in freestanding architectures [18-23].

1.2 Extreme ultraviolet and soft X-rays.

The electromagnetic spectrum is divided into different identified regions; the precise boundaries that separate one region from another are not always perfectly defined. The extreme ultraviolet (EUV) is located between the photon energies of about 30 eV to 250 eV (wavelengths from about 40 nm to 5 nm) fading into the soft x-ray region (SXR) that could extend from about 250 eV to several thousands eV (wavelengths from 5 nm to about 0.3 nm). A detailed description of the physics and applications of EUV and SRX radiation is given in the book of D. Attwood [24], and only a brief introduction will be presented in this section. *In Figure 1.2,* we can appreciate the whole electromagnetic spectrum with a focus on the ultraviolet and X-ray regions.

These photon energies regions are important because of two main reasons: First, these energies are comparable with the binding energies of the core electrons in atoms; Second, the wavelength of EUV-SXR photons approaches atomic dimensions, making them ideal for studying physical and chemical properties of molecules and atoms.

Because in the EUV most materials exhibit significant absorption and also because there are not many available high-intensity EUV light sources (compact sources), experiments to study the optical properties of materials in the EUV represent still a big challenge. With strong absorption and low normal incidence reflectivity, in this region, experiments are best done using thin films as filters.

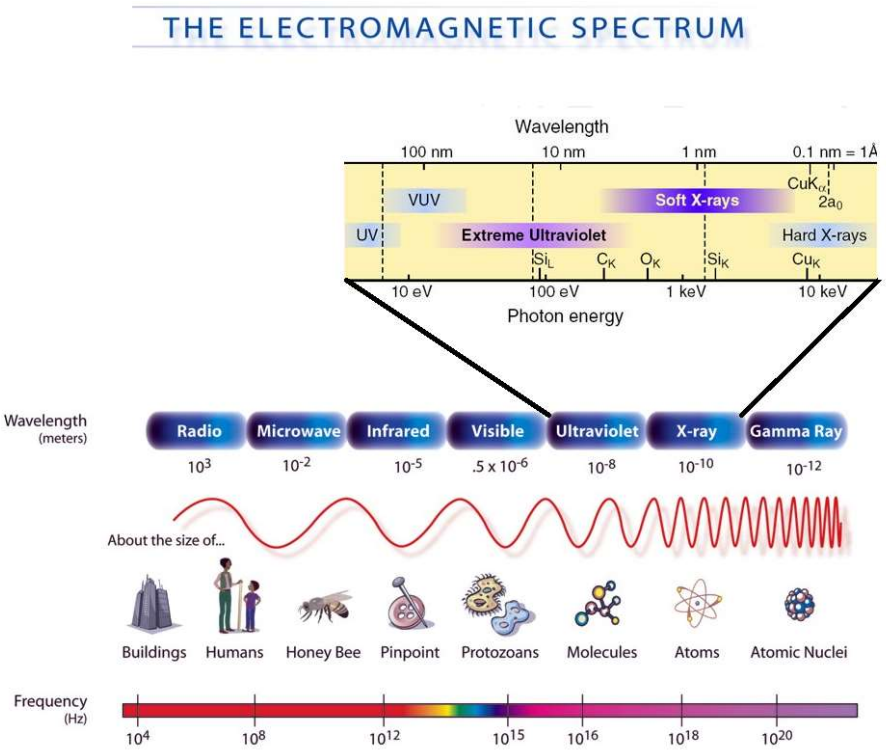

Figure 1.2: *Electromagnetic spectrum, identified regions and their properties can be observed, focusing on the fading boundaries between EUV and SXR.*

EUV radiation is nowadays widely used in several applications. Most of these applications such as lithography, nanotechnology, material sciences, biology, and imaging, require high brilliance light sources, some of those applications need spatial coherence and enough monochromaticity to be able to study and analyze materials and their behavior at the molecular and atomic level. EUV can be generated in different ways, such as hot plasma emission, synchrotron radiation, and high harmonic generation. In laboratory-scale experiments, most sources for EUV radiation are based on the emission of hot plasma; among the sources are Discharge-Produced Plasmas (DPP) and Laser-Produced Plasmas (LPP). The use of synchrotron radiation has made growth of the scientific research utilizing the vacuum ultraviolet to soft x-ray regions. The emission of EUV radiation from FELs, also based on synchrotron radiation [25], has taken a significant consideration as a light source for EUV lithography and other applications due to the tunability, coherence and the availability of high-power accelerators.

1.3 The interaction of EUV radiation with the matter.

There are two models to explain the interaction mechanisms of EUV radiation with matter:

1. The photo-absorption
2. The coherent scattering.

In photo-absorption, the energy of the incoming photon exceeds the ionization energy of the bound electron. When the photon energy is not enough to ionize atoms, the most frequently occurring process is a coherent scattering of the photon without energy loss [24]. Accordingly, the electron-photon interactions model can describe the interaction of EUV radiation and soft X-ray with matter through the concept of scattering cross-sections by multi-electron atoms as follows:

$$\sigma(\omega) = \frac{8\pi}{3} |f^0(\omega)|^2 = \left[\frac{8\pi}{3} r_e^2\right] \times \left[\sum_{S=1}^{N} \frac{-g_s \omega^2}{\omega^2 - \omega_s^2 + i\gamma\omega}\right]^2 \qquad 1.1$$

Where γ is the damping factor due to the absorption, ω_s is the frequency of resonance of the atomic transition and ω is the frequency of the incident radiation. g_s is the parameter related to the oscillatory strength of the electronic transition. The scattering cross-section refers to the effective number of free electrons contributing to the scattering. The $f^0(\omega)$ is wavelength-dependent complex scattering factor, which can be presented into its real and complex components as is given in EUV and soft X-ray.

$$f^0(\omega) = f_1^0(\omega) + i f_2^0(\omega) \qquad 1.2$$

where f_1^0 and f_2^0 correspond to the atomic scattering factors of an element, which are associated with the reflection and absorption, respectively.

Each material shows distinctive interaction with EUV radiation, and it can be described by the concept of the complex optical constant or complex index of refraction ($\boldsymbol{n}$) as:

$$\boldsymbol{n} = n - ik \qquad 1.3$$

where *n* and *k*, are the optical constants and these can be experimentally derived by applying methods based on reflectance and transmittance measurements combined with an optimized algorithm for fitting analysis.

$\boldsymbol{n}$ depends strongly on the frequency. The real part is called the refractive index (n), and k is known as the extinction coefficient [25]. In the EUV, the complex refractive index $\boldsymbol{n}$ can also be described in terms of the atomic scattering factors f_1^0 *and* f_2^0 as:

$$\boldsymbol{n} = n - ik = \frac{n_a r_e \lambda^2}{2\pi} f^0(\omega) \qquad 1.4$$

Where n_a is the atomic density per unit volume, and λ is the wavelength of the EUV radiation and r_e is the classical electron radius which is defined as:

$$r_e = \frac{e^2}{4\pi\varepsilon_0 m_e C^2} = 2.82\ x\ 10^{-1}\ m \qquad 1.5$$

Leading us to the following relationship between the real and imaginary parts of the scattering factor with the optical constants:

$$n = 1 - \frac{n_a r_e \lambda^2}{2\pi} f_1^0(\omega) \qquad 1.6$$

and

$$k = \frac{n_a r_e \lambda^2}{2\pi} f_2^0(\omega) \qquad 1.7$$

In the EUV, the real part of the optical constants (*n*) is smaller than one compared to the visible light. The absolute values of n and k decrease for higher energies, the complex index of refraction of all materials approaches unity. The photons with energy near to the energy necessary to excite an electron from its orbital lead to resonance at that precise energy. The effect of this resonance is manifested themselves in the complex index of refraction ($\boldsymbol{n}$), more significant at n (the real part of the optical constant) since its dependence with the frequency is very acutely; therefore, the optical constants change significantly near the absorption edges. If there is change in composition of material, density of materials and slight variation in effective electron density, the near edge optical response would vary drastically. In contrast with the other energy ranges of the electromagnetic spectrum where resonances occur (between infrared and visible, between the visible and the ultraviolet), the EUV results may be more complicated since the wavelengths are on the same scale not only of the atomic dimensions but also of the size of the physical and structural features of the materials. The nanoscale imperfections or nanoscale structural changes

in films or coatings do not represent significant changes in the optical performance of the device in the other ranges of light, while in the EUV their presence can change it completely [25].

1.4 Reflection and transmission at an interface.

The level of absorption of a material is included in the refractive index in the imaginary part of the equation 1.3. The transmission of light through an absorbing medium, such as thin-film transmittance filter (*figure 1.3*), with thickness χ, assuming that the reflectance is negligible, is determined by the Beer-Lambert law:

$$I_T = I_0 e^{-\mu\chi} \qquad 1.8$$

Where I_0 *and* I *is* the radiation irradiance that enters and exits the medium, respectively. μ corresponds to the absorption coefficient, which is related to the extinction coefficient k through:

$$\mu = \frac{4\pi k}{\lambda} \qquad 1.9$$

Here λ is the wavelength of the radiation in vacuum.

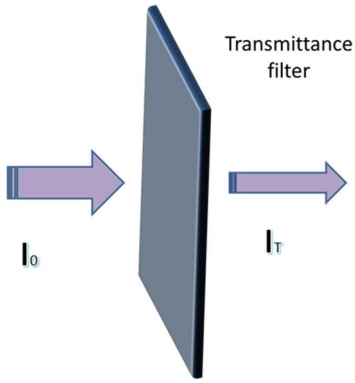

Figure 1.3: *A schematic drawing of a thin film transmittance filter.*

In an idealized interface, as in *figure 1.4*, we consider the interface between two semi-infinite media, where the complex index of refraction of both regions is given as $\boldsymbol{n_i}$ and $\boldsymbol{n_j}$. The radiation, with electric-field amplitude $\mathbf{E_i}$, enters to the second media with an angle $\boldsymbol{\theta_i}$ with respect to the Z-axis. The amplitude of the reflected and transmitted electric fields, $\mathbf{E'_i}$ and $\mathbf{E_j}$, respectively, are given by the famous Fresnel equations.

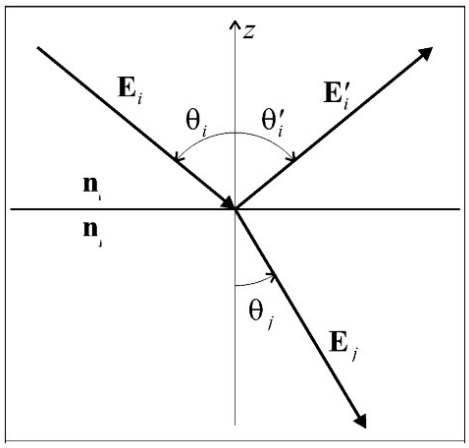

Figure 1.4: *Description of an incident plane wave at the interface between two different materials.* [28].

For s polarization, that is perpendicular to the plane of incidence we will have:

$$\frac{|E_i'|}{|E_i|} = \frac{\boldsymbol{n}_i cos\theta_i - \boldsymbol{n}_j cos\theta_j}{\boldsymbol{n}_i cos\theta_i + \boldsymbol{n}_j cos\theta_j} \equiv r_{ij}^s \qquad 1.10$$

$$\frac{|E_j|}{|E_i|} = \frac{2\boldsymbol{n}_i cos\theta_i}{\boldsymbol{n}_i cos\theta_i + \boldsymbol{n}_j cos\theta_j} \equiv t_{ij}^s \qquad 1.11$$

In the case of p polarization, the Fresnel equations are given by:

$$\frac{|E_i'|}{|E_i|} = \frac{\boldsymbol{n}_i cos\theta_j - \boldsymbol{n}_j cos\theta_i}{\boldsymbol{n}_i cos\theta_j + \boldsymbol{n}_j cos\theta_i} \equiv r_{ij}^p \qquad 1.12$$

$$\frac{|E_j|}{|E_i|} = \frac{2\boldsymbol{n}_i cos\theta_i}{\boldsymbol{n}_i cos\theta_j + \boldsymbol{n}_j cos\theta_i} \equiv t_{ij}^p \qquad 1.13$$

Where $\boldsymbol{\theta_j}$ is the angle of refraction, which is determined from Snell's law; $\boldsymbol{r_{ij}}$ and $\boldsymbol{t_{ij}}$ are the Fresnel reflection and transmission coefficients.

Let's consider a multilayer structure, meaning a series of N layers with N+1 interfaces, where the *i*th layer has thickness $\mathbf{d_i}$, interfacial roughness or diffuseness $\boldsymbol{\sigma_i}$, and optical constants $\boldsymbol{n_i}$, see *figure 1.5*. For the general case, the ambient is the entering region with optical constants $\boldsymbol{n_a}$, and the last region is a substrate with optical constant $\boldsymbol{n_s}$. For our particular case, we are studying thin films free-self-standing filters, so in that case, in the transmittance's calculations presented in the next chapters, $\boldsymbol{n_s = n_a}$ was assumed. For the general case, under the mentioned conditions, the net reflection (r_i) and transmission (t_i) coefficients of the *i*th layer are given by:

$$r_i = \frac{r_{ij}+r_j e^{2i\beta_i}}{1+r_{ij}r_j e^{2i\beta_i}} \qquad 1.14$$

$$t_i = \frac{t_{ij}t_j e^{2i\beta_i}}{1+r_{ij}r_j e^{2i\beta_i}} \qquad 1.15$$

Where $\beta_i = 2\pi d_i \boldsymbol{n}_i cos\theta_i/\lambda$; The roughness or inter-diffusion between the interfaces can cause losses in the specular reflectance, that losses are taken into account in the modified Fresnel reflection coefficients r'_{ij}.The modified Fresnel reflection coefficients must be calculated from the Fresnel reflection coefficients r_{ij} multiplied by the Fourier transform of the interface profile function which depends of the average value in the Z direction of the dielectric function.

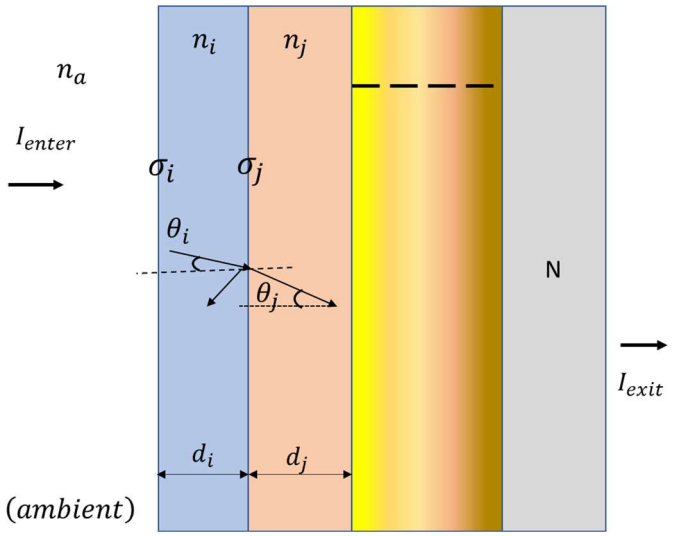

Figure 1.5: *Plane-wave entering in a system of N layers and (N+1) interfaces, where the ith layer has thickness d_i, interfacial roughness σ_i and optical constant n_i.*

The energy reflected from or transmitted through the film is measured by the reflectance R and transmittance T, respectively, as is shown in equations 1.16 and 1.17.

$$R = |r|^2 \qquad 1.16$$

$$T = Re\left\{\frac{\boldsymbol{n}_s cos\theta_s}{\boldsymbol{n}_a cos\theta_a}\right\}|t|^2 \qquad 1.17$$

1.5 High brilliance sources for EUV and soft X-ray radiation.

Sources based on synchrotron radiation (SR) such as free-electron lasers (FELs) are now widely used in multiples scientific applications, they high energies photons are remarkable probes for exploring the atomic and electronic structures of the materials.

A synchrotron is a particle accelerator that produces light with very high-intensity, ultra-bright radiation. The synchrotron radiation is emitted by an electron traveling nearly speed of light when its path is bent by a magnetic field when passing through different magnetic devices such as undulators, wigglers, and bending magnets. The radiation is produced ten billion times brighter than that supplied by conventional sources. The radiation can be emitted over a wide wavelength range depending on the facility, going from the infrared to hard x-rays. Finally, the radiation reaches the experimental stations (beamlines), where different analytical and processing techniques are available.

On the other hand, FEL consists of an electron beam propagating through a periodic magnetic field called a wiggler or undulator. In FELs, the SR light is used to feed an undulator to produce the optical amplification. Depending on the facility, FELs can produce radiation with wavelength ranging from the terahertz region until the hard X-ray region. Today such lasers are used for research in materials science, chemical technology, biophysical science, medical applications, surface studies, and solid-state physics. FELs are designed to produce very fast bunches of light with extremely high peak brightness. The major advantage of FELs is that they produce coherent light many orders of magnitude brighter than the incoherent light produced in synchrotrons, which were used for the previous third generation of light sources [26].

One significant advantage of FELs is the free tunability of the wavelength by simply changing the electron energy. The tunability range, depending on the facilities, can go from 100 to 0.1 nm; in case of X-ray FELs from 10 to 0.1 nm [27, 28], but more than that, FELs light provides beneficial properties like:

- Transverse and longitudinal coherence
- High peak power, tens to hundreds of GW
- Short pulse length, 1 to 100 fs

In the EUV and x-ray range, FELs opens the door to the ultra-small and ultra-fast word. Some application of FEL's are:

- The transverse coherence and the large number of photons make it possible to image periodic and non-periodic structures at the nanometer and sub-nanometer scale.

- The very high peak brilliance and a photon-pulse time structure in the femtosecond-time regime, make it possible to perform coherent imaging experiments and studies of systems out of equilibrium by using stroboscopic-based time-resolved spectroscopies [29, 30].

- Using fast, single-shot imaging, one can follow the dynamics of these phenomena, and overcome the limit set by sample damage.

- Nonlinear phenomena and high energy density systems can be studied using the short pulse duration and considerable peak power.

- The X-ray FEL can be used to explore matter at the atomic-molecular scale with unprecedented space-time resolution [28].

Furthermore, with the advances in seeded FELs, it is possible to study advanced systems as "quantum materials" including 2D materials, unconventional superconductors, colossal magnetoresistance compounds. Moreover, the full coherence of seeded FELs pulses opens the path for studying the statistical properties of an X-ray beam after the interaction with matter, measuring the properties of the coherent state of matter both in and out of equilibrium [30, 31].

Chapter 2.

Thin-film transmittance filters: design

2.1 Choosing Materials.

The optical properties of any filter depend, of course, on the materials chosen to fabricate them; The selection of the materials is made to comply with the requirements of the source. For our research, these requirements are such:

- **Target wavelength range (Bandwidth)**: Our target spectral range for the fabrication of the filters is between 4-20 nm. The filters could be suitable, as an example, for FEL-2 at FERMI. As it was mentioned in section 1.1, FEL-2 works in that spectral range.

- **Exposure time to high energy and aging:** High brilliance sources are unique because of their high power and high peak intensity radiation. High-energy power sources could cause damages and induce accelerated aging of the materials. The chosen materials have to guarantee high mechanical and thermal stability to high power to ensure excellent performance and a larger useful life period [14].

- **Mechanical stability**: Since materials possess high absorption in the EUV spectral range, the transmittance of the filters increases with the decrease of the thickness of the materials, but with a small thickness the fragility of the material increases. So, the materials chosen should be tough enough to ensure the mechanical stability of nanometric thin films, with the correct thickness able to select suitable spectral bandwidth or reject harmonics.

- **Contamination due to oxidation and carbon growth**: Filters are exposed to different sources of contamination during their use. Contamination from air, water, carbon can reduce the performance of the filters and it can contribute to the production of second harmonics photons. Since Carbon and Oxygen K-edge are contained in the EUV and soft x-ray range, the resonance of the respective atoms can occur. When soft X-ray pulses from a free-electron laser enter the material, they excite inner-orbital electrons in the carbon atoms; for carbon atoms making up a graphite interface, these excitations can produce a photon with twice the energy of the incoming photons [32].

  The chosen materials should be resistant to corrosion and not reactive when they are exposed to those types of contaminants [10, 12]. Another option is adding a protective coating to the filter.

In summary, the designed filters must guarantee the following: 1) The filter window will need to provide the highest possible transmittance between 5 – 20 nm). 2) Reduce out-of-band radiation in the ultraviolet, and hard x-ray. 3) Partially protect the optics from debris from the radiation source and any outgassing from the materials; Outgassing from the filters must be minimal, and

they must survive handling as well as pressure differentials during pump-down operation, and return-to-atmospheric pressure. 4) EUV filters must operate in a harsh vacuum environment. 5) To survive temperature increases due to the absorption of the out-of-band radiation while are irradiated with high energy EUV light.

We proceed to simulate the transmittance performance of different materials in the targeted wavelength range.

Simulations are done using an open-access software product called IMD package, developed by Windt [33, 34]. IMD is a versatile software that allows, among other options, to model the layers of your filters device and simulate their transmittance, reflection, and absorption response in the desired wavelength range. Reflection and transmission of electromagnetic waves incident on an interface of two media with different indices of refraction are described by the Fresnel equations, shown in section 1.4. IMD calculates the Fresnel coefficients for each interface in a recursive manner (the Parratt formalism), using the optical constants of the different elements located in their database. These optical constants can be based on theoretical calculations or experimental data added by different scientists over the years.

As we mentioned before, since materials have high absorption, finding materials that can fulfill all the requirements to be applied at high-brilliance sources is quite challenging. Some materials such as Beryllium and some rare earth elements are suggested to be good candidates for transmittance filters in the spectral range of interest, but the toxicity of rare earth materials makes the fabrication of such filters very difficult and dangerous.

In *Figure 2.1* and *Figure 2.2,* we can appreciate the theoretical transmittance response of different materials. The optimization parameter was the thickness of the layers. All simulated filters have 100 nm thickness.

Aluminum is one of the most used material for filters in the EUV, but its transmittance in the out-band region is not acceptable. Boron Carbide (B_4C) and Ytterbium (Y) are very promising materials, but again, they are not a good fit for the desired wavelength target. We realized that Zr and Nb are the best candidates for the fabrication of such filters. Zr has a higher transmittance response, in the targeted wavelength range, but Nb is more robust and more thermally stable. Using the evaluation of the transmittance performance together with the mechanical strength of the materials, the possibility of fabrication in the available facilities for the project, the toxicity-free of the elements, Zr and Nb were selected as chosen materials for the fabrication. Moreover, instead of going for single layer transmittance filters, we decided to fabricate bilayer structures, combining Zr and Nb in order to enhance their best properties and obtain filters with excellent transmittance, good mechanical strength, and thermal stability.

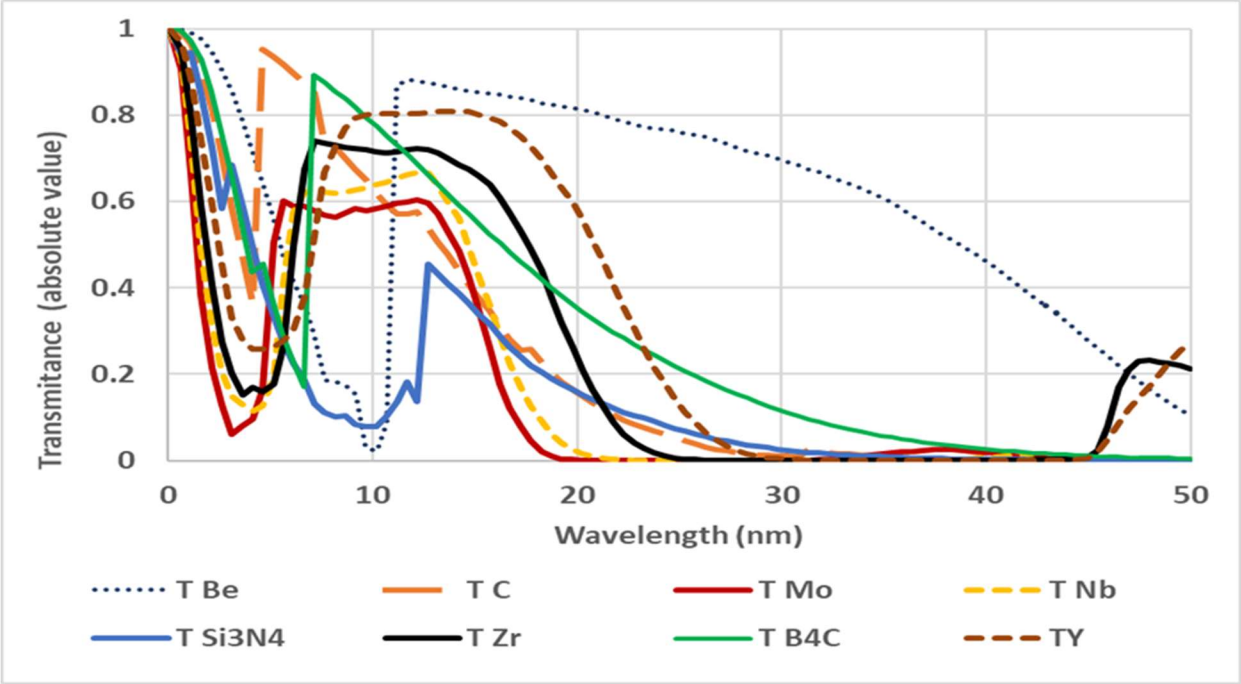

Figure 0.1: *IMD simulations of transmittance of filters of different materials, from 2 to 50 nm spectral range. The total thickness of each filter is 100 nm.*

In *figure 2.2* is shown the comparison of the transmittance response of the bilayer structures Zr/Nb and Nb/Zr in contrast with other single layer filters. Single-layer filters of Zr and Nb will also be studied in order to understand better the optical and mechanical performance of the bilayer structures filters.

For the fabrication of the filters, we have used Si_3N_4 membranes as substrates, which provides extra mechanical support to the samples during fabrication process. In *figure 2.3*, a schematic diagram of the structural design of the filters is presented. We have shown the bilayer structures formed by Nb/Zr and Zr/ Nb and the single layer of Nb and Zr on Si_3N_4, the detailed fabrication steps will be presented in the next chapter.

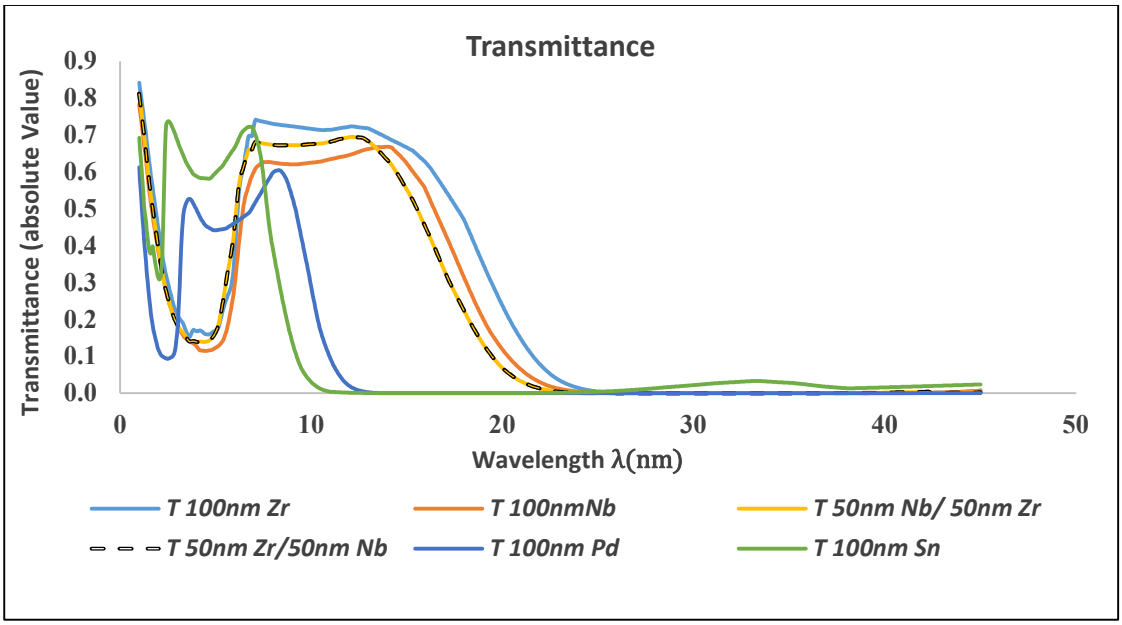

Figure 2.2: *IMD simulations of transmittance performances for a total thickness of 100 nm filters of different materials, some single layer, and some bilayer filters, from 2 to 45 nm spectral range. Bilayer structures of Nb/Zr and Zr/Nb are shown.*

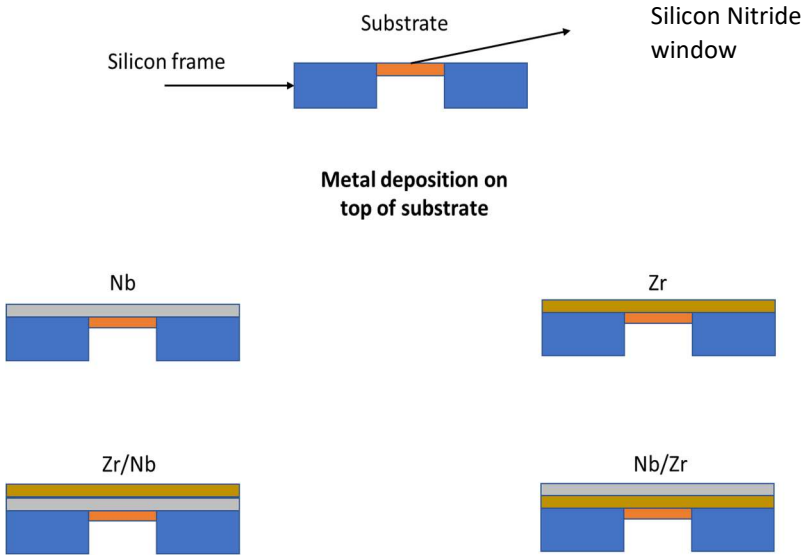

Figure 0.3: *The structural design of the samples. Four types of samples were prepared. Single-layer of Nb and Zr and bilayer structures Zr/Nb and Nb/Zr.*

2.2 Niobium and Zirconium.

Zr and Nb are transition metals with atomic numbers 40 and 41 respectively. They have a higher melting point and better thermal stability than other materials like Palladium or Tin, also used for thin-film filters [10, 13, 35]. Nb is also a refractory metal, refractory metals are known because of their extreme resistance to heat and wear. Those properties are necessary because of the high temperatures that filters can reach when they are irradiated by FEL light.

Zirconium has silver-gray color, very strong but malleable, ductile, and easily forms stable compounds. It is flammable in powder form, and highly resistant to corrosion and heat but oxidizes very fast in contact with air. The most common oxidation state in the thin film is ZrO_2.

Niobium is crystalline and very ductile. Pure Niobium has a hardness like the pure titanium. Niobium oxidizes in the earth's atmosphere very slowly. Niobium has high thermal conductivity, high melting point, good corrosion resistance, low neutron capture cross-section, and good biological compatibility. The most common oxides formed in thin films is Nb_2O_5 [36, 37].

Both, Zr and Nb, are suited for e–beam deposition and sputtering techniques and they are two of the few materials with proper optical, chemical, and mechanical properties for being an option for transmittance filters in the range 4-20 nm wavelength.

Principal chemical properties of Nb and Zr are listed in *table 2.1*.

Table 2.1: Principal properties of Zr and Nb. [36, 37, 38].

	Zr	Nb
Group	**4**	**5**
Period	**5**	**5**
Block	**d**	**d**
Atomic number	**40**	**41**
State at 20°C	**Solid**	**Solid**
Electron configuration	**[Kr] 4d25s2**	**[Kr] $4d^4 5s^1$**
Melting point	**1854°C, 3369°F, 2127 K**	**2477°C, 4491°F, 2750 K**
Boiling point	**4406°C, 7963°F, 4679 K**	**4741°C, 8566°F, 5014 K**
Density (g cm−3)	**6.52**	**8.57**
Relative atomic mass	**91.224**	**92.906**
Key isotopes	**90Zr, 92Zr, 94Zr**	**93Nb**

2.3 Nb and Zr, transmittance filters background.

Single foils of Zr and Nb are being used as transmittance filters and have been tested in different wavelength ranges, for applications of extreme ultraviolet high-volume lithography instrumentation and in FELs [12, 16, 17, 22-25, 33]**,** but Zr/Nb (Zr top layer) or Nb/Zr (Nb top layer) bilayer structures have not been tested yet for any of these applications.

In 2001 Forbes R. Powel and Terry A. Johnson presented Zr films of around 100 nm supported by a Ni mesh reporting 48% of transmittance at 13.4 nm, used as filter windows for lithography application [14].

In 2007 V.P. Belik et al. showed some results for 100 nm Nb and Zr filters supported by Si_3N_4 membranes with a transmittance peak of 30% around 13 nm. They also presented a 240 nm thick Nb/Si multilayer (6 nm Nb, 6 nm Si; 20 pairs), supported by a gold mesh with 18% of transmittance near 11 nm and approximately 45% around 13 nm, as a filter for nanolithography [22].

Furthermore, Wu Heyun, also in 2007 presented self-supporting Zr filters, for soft x-ray laser applications, but with higher thicknesses 300, 400, and 500 nm; the thinnest one, shows the highest, 35% peak transmittance around 13.5 nm [20]**.** In 2011 Yonggan Wu et al. presented Zr filters supported by a Polyamide film with 10.5% transmittance around 13 nm and 14% around 11 nm, looking for filter materials for soft x-ray [23].

In addition, in 2011, N.I. Sckhalo et al., fabricated different multilayers structures based on $Mo/ZrSi_2$ combinations, with a transmittance peak of around 72% near 13 nm, but very low transmittance for the range between 5-10 nm [21]. In 2012, S. Brose et al. achieved free-standing Nb filters tested at 11 nm with 48% of transmittance [15]. In 2015, C. Tarrio fabricated Zr filters of 250 nm supported by Cu mesh, pursuing a better mechanical structure; These filters have a maximum peak transmittance of 48% [10].

Chapter 3.

Experimental, part 1: Filters fabrication.

The following chapter covers in detail the fabrication of the samples. The sample fabrication procedure was not the same for all experiments. Hence first a typical process is introduced, then deviations from this process for individual experiments are explained.

The fabrication procedure is shown in the following schematic diagram, *figure 3.1.*

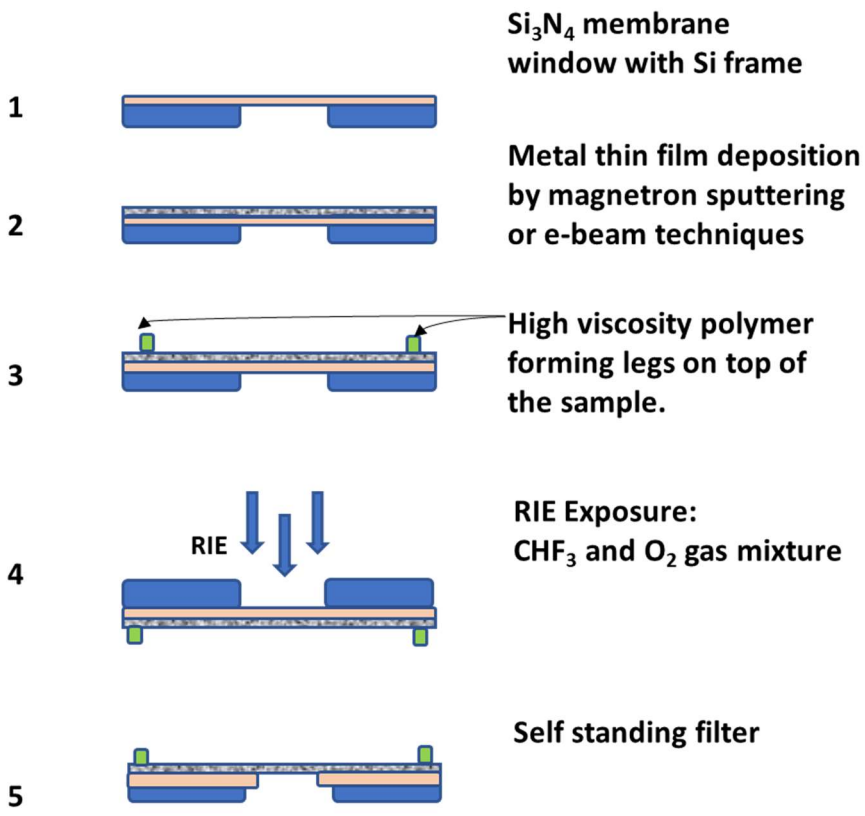

Figure 3.1: *Schematic diagram of the simplified fabrication process of the free self-standing filters.*

Using a Si_3N_4 membrane as substrate (step 1), we proceed with the deposition of the metal layers on top of the substrate by magnetron sputtering (step 2) or E-beam evaporation technique. Four polymer dots are deposited with a small needle to protect the front of the top layer of the filter since the filter must be turned over in other to proceed with the RIE process in the backside of the sample (step 3). To obtain a free self-standing filter, the Si_3N_4 substrate must be etched. Reactive ion etching (RIE) (step 4) has been applied on the membrane backside in order to open a window in the silicon nitride. In the following we will describe in detail step by step the fabrication process.

3.1 Step 1. The Substrate.

Silicon nitride (Si_3N_4) membranes from Silson Ltd, Company specialized in the fabrication on this kind of membranes, were used as a substrate for the fabrication of several Zr, Nb, Nb/Zr and Zr/Nb thin films filters with different thicknesses. The substrate area has a square Si_3N_4 membrane window of 3 mm X 3 mm surrounded by a silicon frame, for a total area of 7.5 mm X 7.5 mm. The Si_3N_4 membrane window is about 100 nm thick while the silicon frame is about 200 µm.

Since membranes windows are very fragile, we designed custom-made holders that were used to handle the samples during both the metal deposition and the characterization procedures. Holders were fabricated of aluminum (body part) and bronze (clamps). The design of the holder is presented in *figure 3.2.*

Membranes were bought in packages of 50 membranes. AFM not-contact images of one membrane have been taken to analyze the topography of the filter substrate; *Figure 3.3* shows an AFM image of one of the membranes measured and the histograms analyzed to obtain the roughness results. Different areas of the membrane were scanned; the roughness on the membrane was about 1.2 +/- 0.2 nm.

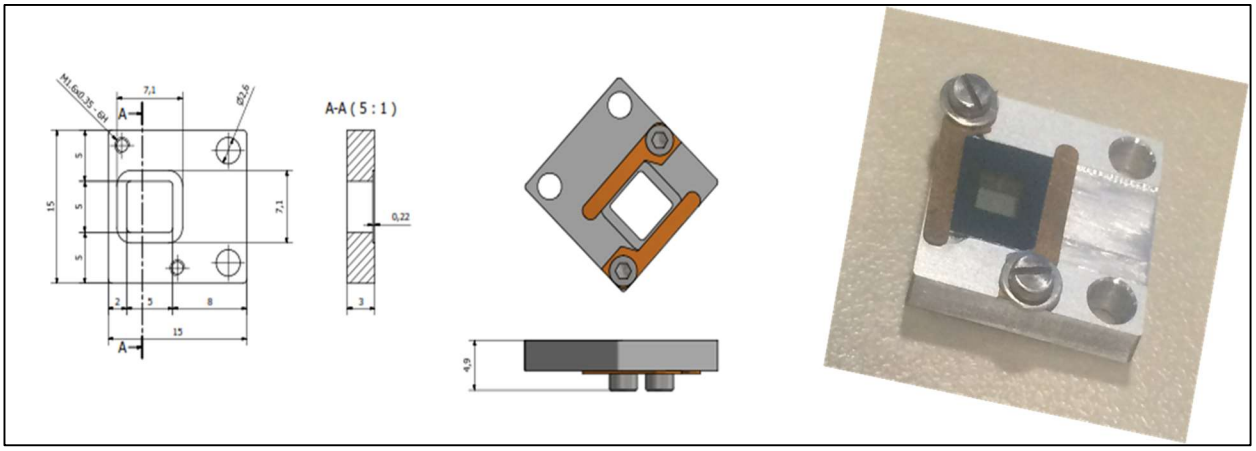

Figure 3.2: *Custom-made aluminum holder with adjustable bronze clamps. It has two extra screw holes, so the holder can be assembled with a specific sample holder adapted for synchrotron measurements.*

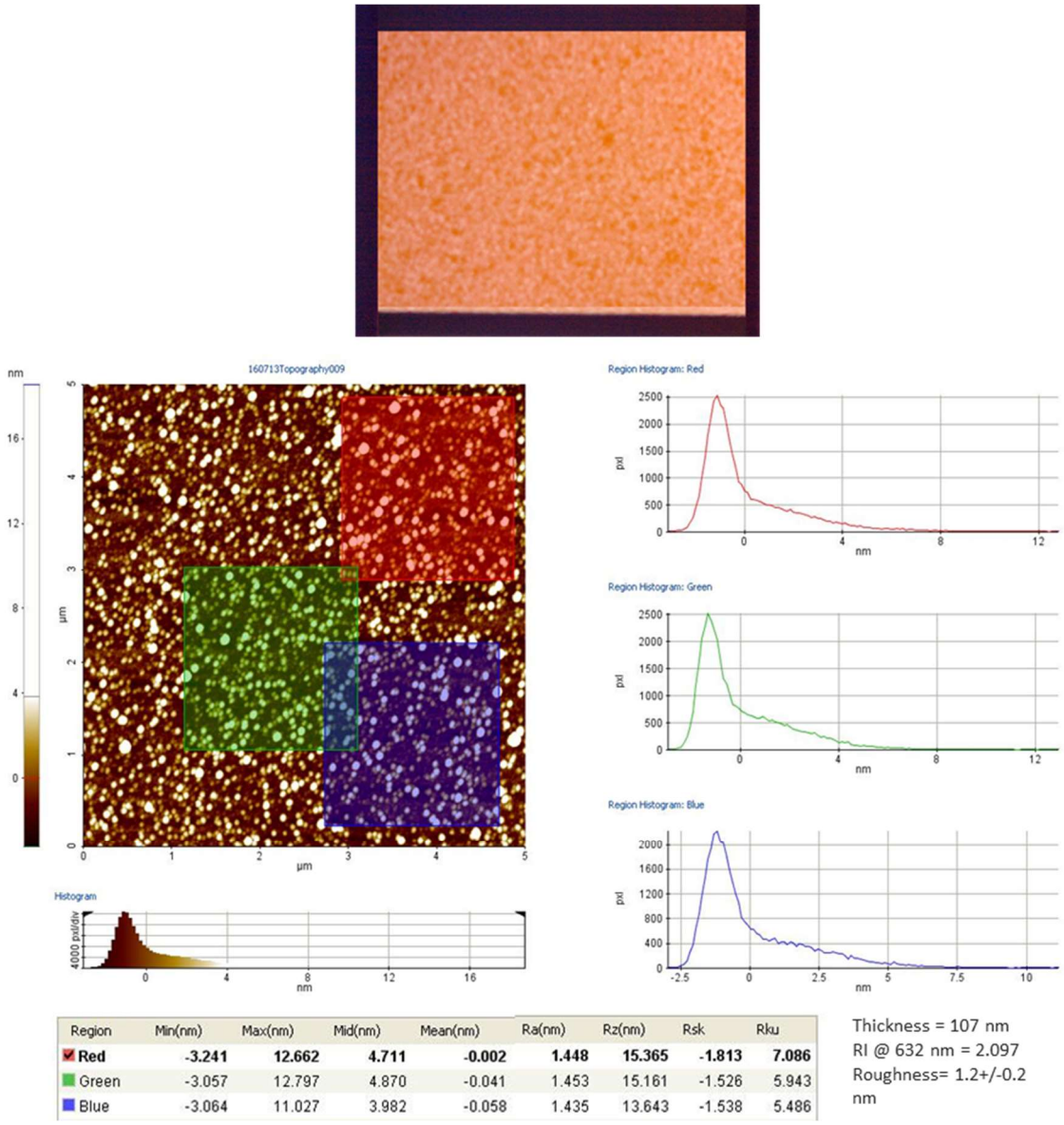

Figure 3.3: *Top: an optical microscope image of a Si_3N_4 membrane used as a substrate for the fabrication of the filter samples. Bottom: AFM image and roughness measurement on the membrane. The histograms of the three chosen areas (colored squares) to be analyzed are shown.*

3.2 Step 2. Metal deposition of the thin film layers.

Of the many methods that can be applied for the deposition of metal materials, magnetron sputtering, and electron beam evaporation are the most widely used. These two methods are the ones we have used to fabricate the samples utilized in different experiments.

- Magnetron RF sputtering technique was used to fabricate all the examples of experiment 1 (described in chapter 5).

- E beam evaporation technique was used for the fabrication of the rest of the samples, samples utilized in the TEM structural characterization (chapter 6) and experiment 2 (chapter 7).

Further discussion and description of these two methods are provided in the subsequent sections.

3.2.1 RF Magnetron Sputtering deposition technique.

Magnetron sputtering is a Physical Vapor Deposition (PVD) process, it is one of the most versatile techniques used for the deposition of metallic films when high-quality films are required. The principle of this technique is shown in *figure 3.4*, left. Substrates are placed in a vacuum chamber facing the target, which is composed of the material to be deposited. The metallic target is set on a magnetron in an inert gaseous atmosphere. The magnetron generates plasma at the surface of the target, the gas ions present in the discharge knock off the target material with sufficient force to dislodge and eject atoms from the target which consequently will condense on the substrate that is placed in proximity to the magnetron sputtering cathode (where the substrate is placed). The plasma is generated in an argon atmosphere at pressures typically between 1 and 10 mTorr. By controlling the argon flow, power, deposition time, and substrate temperature, the film thickness and deposition rate can be tailored. This technique allows for a wide range of film thicknesses from tens of nanometers to a few micrometers.

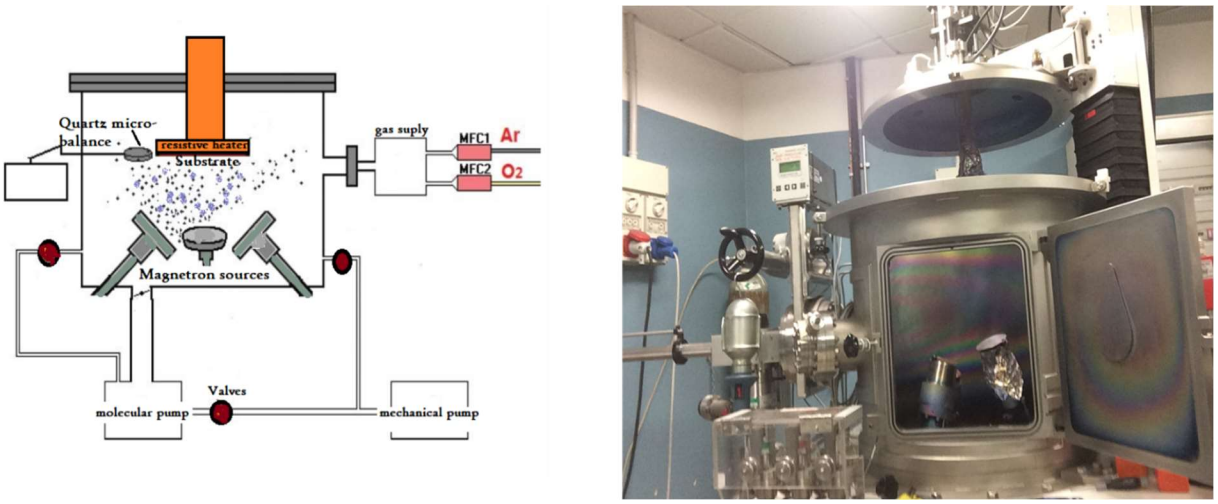

Figure 3.4: *Left: A schematic diagram of a magnetron RF sputtering. On the right: magnetron RF sputtering used for the deposition of the samples at the Department of Molecular Sciences and Nano-systems, Ca' Foscari University of Venice, Italy.*

Magnetron sputtering process produces films with high purity, well-controlled composition, and provides films with better adhesion and homogeneity and permits good control of film thickness [39-42].

3.2.2 Magnetron sputtering set-up and deposition process.

A set of samples were fabricated using magnetron sputtering evaporation technique at the *Sputtering Lab of the Department of Molecular Sciences and Nano-systems, Ca' Foscari University of Venice, Italy.* A picture of the set-up is shown in Figure 3.4, right. Sputter depositions were performed in a custom-built radiofrequency (RF) magnetron sputtering system (13.56 MHz), equipped with three independent circulars (2-inch in diameter), water-cooled, planar magnetron sources, and an rf-biased sample holder. The cylindrical process chamber (equipped with a load-lock system) has both the diameter and the height equal to 60 cm; it is evacuated by the concurrent action of a turbomolecular pump and a cryogenic one. Throttle valves are placed between the pumps and the chamber to control the pumping speed. The base pressure in the chamber was in the range $1–10 \times 10^{-5}$ Pa. Depositions were performed using pure Ar (99.9995%) at a total working pressure around 50×10^{-2} Pa. The working pressure was maintained by the cryogenic pump; during the deposition, an additional and masked magnetron sputtering DC source (loaded with a pure Ti target) was also working to decrease the partial pressure of residual reactive gases, mainly oxygen, present in the vacuum chamber. The targets used on the two independent rf-sources were 2-inch diameter Nb (99.95%) and Zr (99.5%) metallic disks, ¼-inch thick each. The lower purity of Zr target is mainly due to the well-known difficulty to produce Hf-free zirconium: the presence of Hf atoms in all the Zr-deposited films was confirmed by Rutherford backscattering spectrometry (RBS), showing in all films a Hf/Zr ratio of about 1%. The rf-power applied to the targets was 30 W, for deposition time ranging from 85 to 350 min. The two sources were both operated in an unbalanced-magnetron configuration. Film deposition was performed at room temperature in an off-axis configuration; the 4 inches diameter substrate holder, rotating at 10 rpm, was placed above the sources. At first, sources were conditioned for 20 min at the operating conditions to remove residual surface contaminations on the targets. For both sources, the deposition rate was about 30 nm/h. Twelve depositions were performed, three for each kind of composition: Zr, Nb, Nb/Zr, and Zr/Nb considering two different thicknesses for each layer; several samples were deposited at the same time, for a total of **30 samples analyzed**.

3.2.3 E-beam evaporation technique.

Electron beam evaporation (E-beam) is a Physical Vapor Deposition (PVD) technique. The E-beam machine consists of two main sections: an electron source (electron gun) and the deposition chamber. The high-vacuum EB deposition system has a main chamber pumped using an ion pump and a Ti sublimation pump, and a load-lock chamber pumped using a turbopump and a rotary

pump. The background pressure of the main chamber was 4×10^{-9} Pa with the use of a liquid N_2 shroud.

The deposition rate and the thickness of the layer can be controlled using a quartz crystal- thickness controller. In this technique, an intense electron beam is generated from a charged tungsten filament and steered via electric and magnetic fields to strike source material at the crucible and vaporize it within a vacuum environment. At some point as the source material is heated via this energy transfer, it's surface atoms will have enough energy to leave the surface [42, 43]. Atoms will traverse the vacuum chamber at thermal energy (less than 1 eV) and will be deposited at the substrate positioned above the evaporating material. The average working distances are 300 mm to 1000 mm. The deposition geometry mainly influences the final film, uniformity []. A schematic drawing of an E-beam evaporator is shown in *figure 3.5*, Left.

.

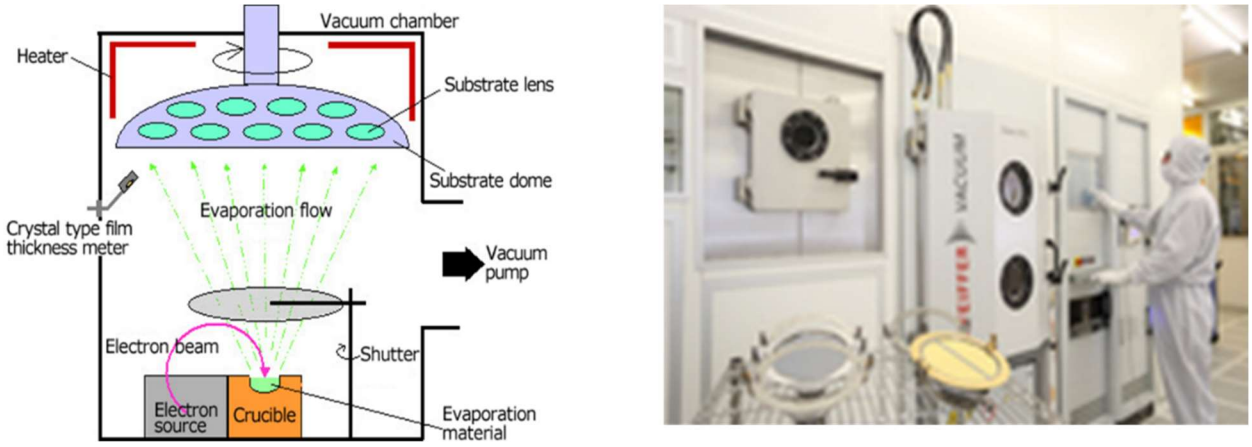

Figure 3.5: *Left, a schematic diagram of an Electron Beam evaporation device, image is taken from https://www.jeol.co.jp/en/science/eb.html. On the right, E-beam evaporator Balzers (Pfeiffer) PLS 500, used for the deposition of the samples. The device is located at the Helmholtz Nano Facility (HNF), Forschungszentrum Juelich, Germany.*

The differences between these two types of deposition techniques are summarized in table 3.1.

Table 3.1: *The main differences between a sputter deposition system and E-beam evaporation system* [42-45].

Parameters	Sputtering	Evaporation
Vacuum	Low	High
Deposition rate	Low (except for pure metals and dual magnetron)	High (up to 750,000 A min^{-1})
Adhesion	High	Low
Absorption	High	Less absorbed gas into the film
Deposited species energy	High (1–100 eV)	Low (~0.1–0.5 eV)
Homogeneous film	More	Less
Grain size	Smaller	Bigger
Atomized particles	More Dispersed	Highly directional

3.2.4 E-Beam evaporation set-up and deposition process.

Two sets of samples were successfully fabricated by using e-beam evaporation instrument: high vacuum Balzers (Pfeiffer) PLS 500 at the cleanroom of the Helmholtz Nano Facility (HNF), Forschungszentrum Juelich, Germany. A picture of the set-up is shown in *Figure 3.5 right*.

Nb and Zr layers were deposited without heating the substrate in this experiment. Nb pellets of 10 mm with the purity of 99.9% and Zr pellets of 8 mm with the purity of 99.2% were used for the evaporation of this set of samples. The deposition rate of Nb and Zr was 0.3 nm/s. The pressure during evaporation was kept on the order of $\sim 10^{-7}$ Pa. The machine was working at 25% of maximum power, the high output voltage was 9.99 kV and current at the source was of 174 mA.

At first, different sets of membranes were deposited with Zr and Nb (single layer and bilayers) to try out the etching procedure until we reached the perfect parameter for the correct etching of the samples. Finally:

- One set of six samples was used for XRD and TEM structural study; these samples were not etched.
- One set of six samples was used for experiment 2, Study of EUV radiation damage on free self-standing Nb, Zr, Nb/Zr, and Zr/Nb thin-film filters, described in chapter 7.

A comparison between the samples deposited using magnetron sputtering versus samples deposited using e-beam is shown in *figure 3.6.* The mechanical properties of the filters are influenced by the deposition conditions such as deposition rate and vacuum level during deposition; samples presented a different kind of stress on the surfaces depending on what type of deposition technique was used.

Different from the samples deposited using Magnetron sputtering technique, Zr, Nb, Nb/Zr, Zr/Nb, and Nb/Zr/Nb samples, of about of 100 nm total thickness on Si_3N_4 membrane substrate, deposited with E-beam resulted with flat and smooth surfaces. It seems that the ultra-high vacuum e-beam evaporation offers better conditions for the deposition of the materials resulting in filters that are more mechanically stable.

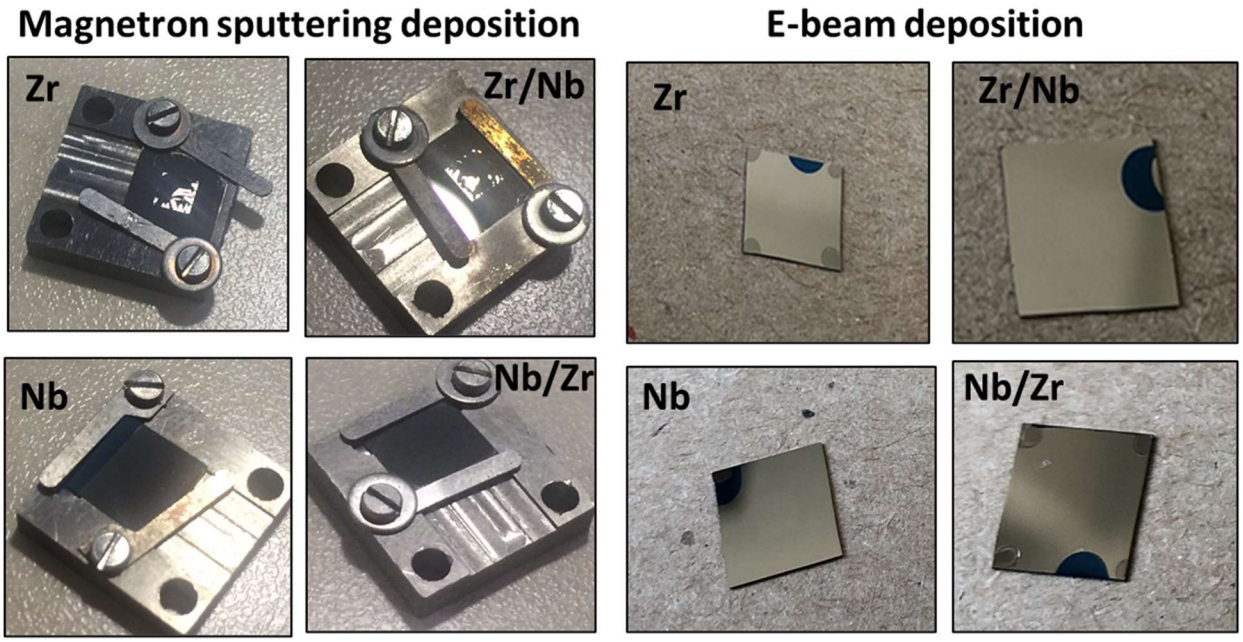

Figure 3.6: *Samples deposited using magnetron sputtering versus samples deposited using e-beam. All samples deposited with e-beam show flat and smooth surfaces while only Nb and Nb/Zr samples deposited using magnetron sputtering are smooth, Zr and Zr/Nb show wrinkled surfaces.*

3.3 Step 3. Placement of polymer "legs."

High viscosity polymer dots were placed in the four corners of the top layer of the sample to avoid that the surface of the sample gets damage during the RIE process, see *figure 3.7.* The polymer legs prevent the contact of the top layer with the RIE cathode plate of the chamber. For the RIE process samples must be turned over with the backside facing up, so it can be hit by the plasma of a mixture of gases to etch the membrane. PMMA AR-P was used to form the polymer "legs." The polymer dots were placed with the help of a rounded needle.

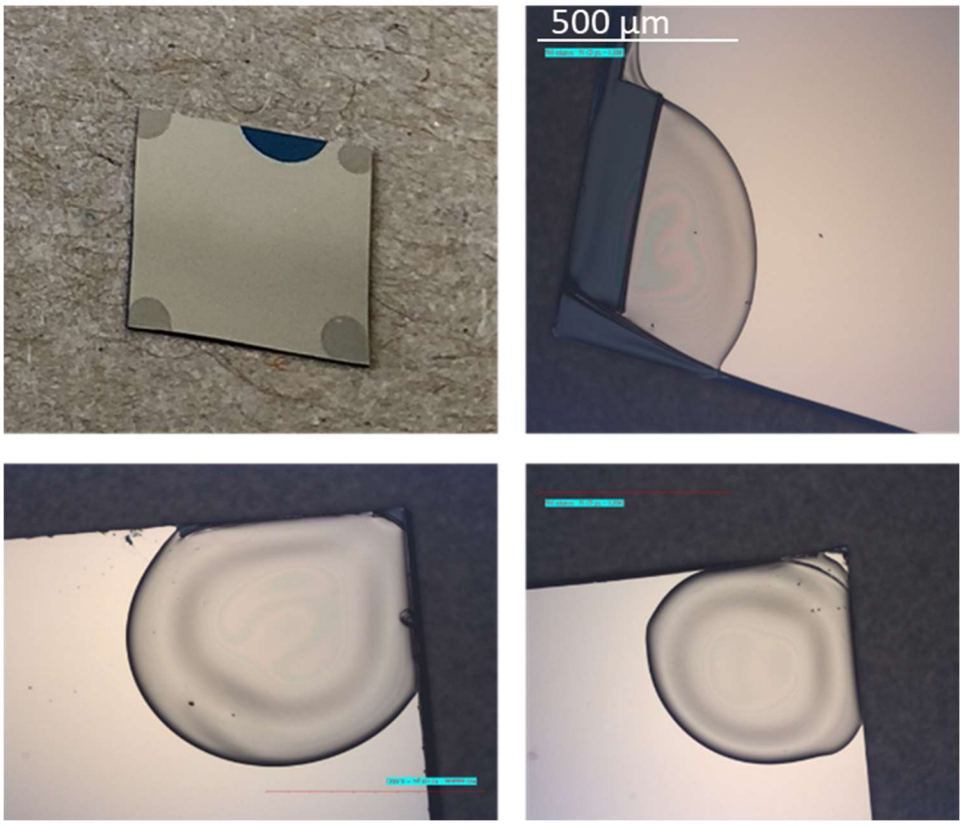

Figure 3.7: *In the left top image, the four polymer dots can be appreciated; the three other images are optical microscopy images of the samples showing each one a corner with the polymer dots.*

3.4 Step 4. Etching the membrane.

In a reactive ion etcher, the samples are placed on a cathode which is capacitively coupled to a radio-frequency generator, while the anode is grounded. Free electrons, which are accelerated with an electric field collide with the gas molecules, ionize them and initiate a plasma of a mixture of gases. Ions and reactive neutral radicals start to bombard the surface almost at normal direction and etch the exposed part of the surface.

In the first experiment, for the samples fabricated using magnetron sputtering technique, the etching procedure to free the thin metal films from the silicon nitride membrane substrate was performed at the Institute for Photonics and Nanotechnologies (CNR - IFN) in Rome, Italy, while for the samples used in the rest of the experiments (samples fabricated using e-beam evaporation techniques) the RIE process was performed at the cleanroom of Helmholtz Nano Facility (HNF), Forschungszentrum Juelich, Germany, using as a reactive ion etcher an Oxford Plasmalab 100 Cluster Tool.

The sample has been inserted into the RIE chamber with the backside upward in order to better expose the membrane to the etching plasma, protecting the front side in order not to damage or contaminate the surface of the film. Using the following recipe: 50 sccm CHF3; 10 sccm O2; RF power: 175 W; Pressure: 55 mTorr; V bias: 250V; time: 2' 50''; few tryouts with different samples were performed to adjust the exposure time of the sample to the reactive action of the mixture. In *figure 3.8*, some broken samples after the etching process are shown and also the difference between a no-etched, a partially etched, and a completely etched filter can be appreciated. Even though in the figure, the etched sample shows compressive stress and wrinkled surface, it is worth mentioning that not all the samples share this behavior. Depending on the type of evaporation process and the order in which the materials were deposited, samples can have a completely flat surface after the etching process as we will show in chapter 7.

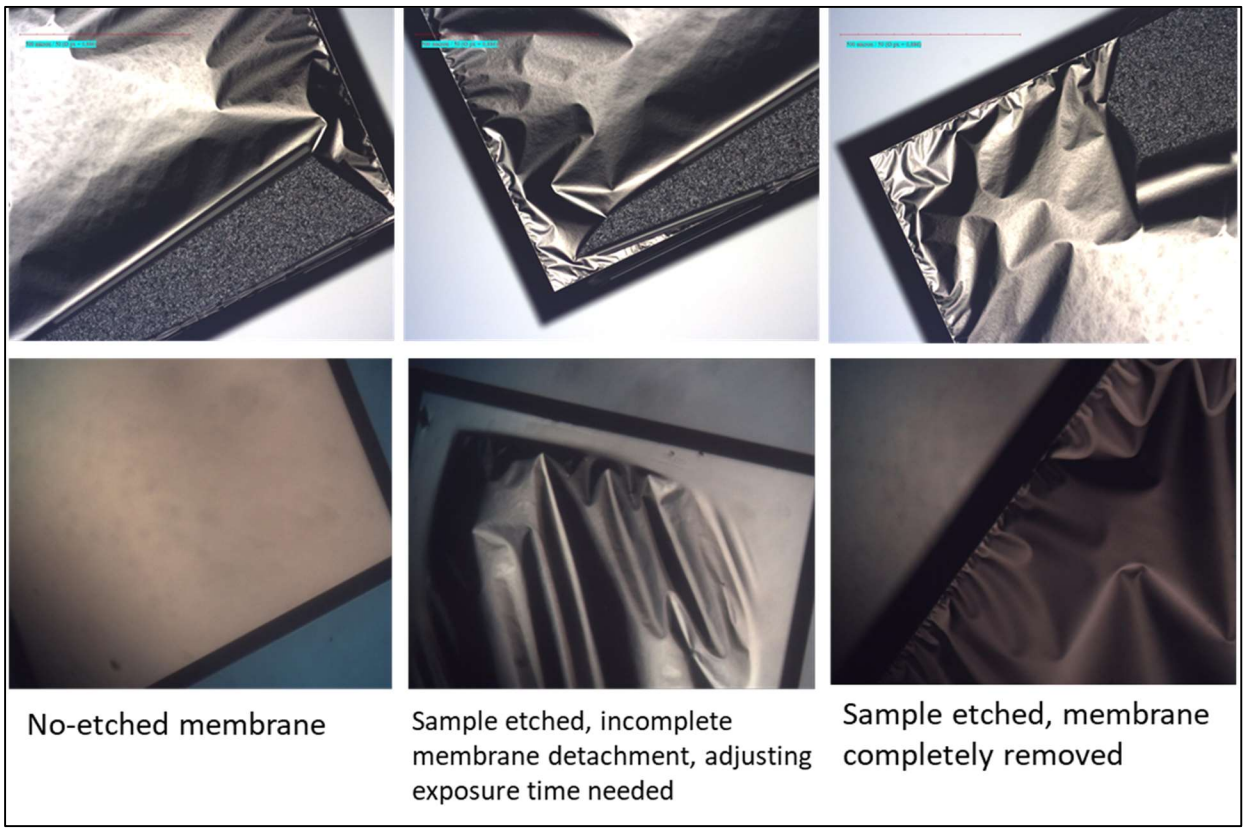

Figure 3.8: *Top: Broken samples after RIE procedure, samples look completely etched. Bottom: Difference between a membrane that is not etched, a partially etched membrane, and a completely etched membrane.*

Chapter 4.

Experimental. Part 2: Characterization Methods.

In this chapter the different characterization methods used on the samples are presented together with the description of the instruments used and the physics principles that explain how each instrument or measurement technique works. The characterization methods are mainly divided into three parts: the mechanical, structural, and optical transmittance characterization.

The characterization includes the determination of the thickness, determination of the crystal structure when applied, chemical composition, and optical characterization (transmittance). Methods used to do such characterization are presented in the following sections.

4.1 Atomic Force Microscopy.

Atomic Force Microscopy (AFM) was used to scan the surface of the first set of samples, used in experiment 1. When scanning the surface of the sample, an image is obtained, this image is used to derive the surface morphology — this way, the smoothness of the surface could be determined.

In AFM an oscillating cantilever with a very narrow tip passes at a very short distance over the surface. The force between the tip and the surface acting on the cantilever is measured by the tilt of a laser beam focused on the cantilever. Typically, a feedback loop of the z piezo in the instrument keeps the cantilever amplitude of oscillation constant throughout the image by keeping the tip at a constant distance to the surface [46]; If the distance between the tip and the surface varies, like in the case of roughness, the oscillations behavior of the tip changes due to the increase of the Van-Der Waals interactions, forces, then the height positions of the cantilever are used to build the AFM image and hence a height profile of the surface. The roughness value can be calculated from either a cross-sectional profile (line) or a surface (area). The most common roughness parameters rely on the calculation of the vertical deviation from a mean line or plane. For this reason, only instruments that provide a quantitative measure of z can provide the proper data to obtain the roughness.

The surface roughness of the samples was measured in air by atomic force microscopy (AFM) using a Park System 70 XE-series AFM in non-contact mode *at* CNR- Institute for Photonics and Nanotechnologies IFN (CNR-IFN) Padova, Italy. The scanned area was 5x5 μm^2. The root-mean-square (RMS) and average surface roughness (Ra) were determined by using XEI data analysis software (Park Systems Corp). Measurements were taken for the substrate and the deposited samples. The silicon nitride membranes used as substrates always show roughness values less than 1.6 nm.

4.2 Rutherford backscattering spectrometry for thickness determination.

An additional 1 × 2 cm^2 flat piece of SiO_2 (1 mm thick) was mounted on the sample holder, as a witness sample, to be deposited together with the filter's substrates using magnetron sputtering. The witness sample was used to measure the thickness and composition of the deposited films by Rutherford backscattering spectrometry (RBS). As an alternative method to confirm RBS thickness results a portion of the Si substrates of the filters was masked during film deposition; The height difference between the masked and the no-masked portions of the Si frame was used to estimate the thickness of the deposited layers by measuring the step edge height with a contact profiler. The deposition rate derived by profilometer measurements was subsequently compared with the RBS data.

During RBS He+ ions scattered by the material are detected to determine its elemental composition and distribution. Incident He+ ions collide with target atoms in the sample and transfer energy to them due to Coulomb scattering. In these elastic collisions, the principles of conservation of energy and impulse are valid, and the energy of the scattered He+ ion E_H is entirely determined by the masses of the He+ M_H, the mass of the target atom M_T, the scattering angle θ and the energy of the incident He+ E_0 according to the following relation [47]:

$$E_H = E_0 \left[\frac{\left(M_T^2 - M_H^2 sin^2\theta\right)^{1/2} M_H cos\theta}{M_T + M_H} \right]^2 \qquad 4.1$$

The higher the mass of the target atom M_T, the higher is the measured energy of the scattered He+ ion E_H for a fixed scattering angle θ, and thus different atomic elements can be differentiated in the RBS spectra. If the incident He+ ion penetrates deeper into the target material, it does not only lose energy due to Coulomb scattering at a specific target atom but it also loses smaller energy amounts due to the small scattering angle [48]. Hence, target atoms that are deeper into the material result in a stronger reduction of the energy in the measured spectrum than target atoms of the same element at the surface. This characteristic offers the possibility to determine the thickness of a specific layer by RBS. The measured data were analyzed deploying the software RUMP [48, 49].

4.3 X-ray Diffraction (XRD).

Thin films deposited by sputtering built of small grains can be crystalline or amorphous. The size, shape, and stacking of the grains are part of the film morphology. X-ray diffraction (XRD) was used to determine if the film is amorphous or polycrystalline.

If the sample is a crystal, x-rays are diffracted only in directions satisfying the Bragg condition:

$$2dsin\theta = n\lambda \qquad 4.2$$

Where d is the distance between crystal planes, 2θ the Bragg angle, n is an integer and λ the wavelength of the monochromatic x-rays. The position of the peaks depends on the crystal symmetry, and the size of the elementary cell of the lattice since each crystal has a different lattice, the element, and its crystal structure can be determined. Crystalline phases present in a sample can be identified on the base of x-ray diffraction curves in standard databases [50, 51]. On another hand, because in XRD only the scattered X-ray intensity is measured and information about the phase is missing, modeling is usually required to fit the measured intensity, and then by an indirect method, the structures of samples could be obtained. The problem with modeling is that fits are not unique. The analysis becomes more difficult in the case of multilayer, where XRD peaks can be low due to the unavoidable diffusions and formations of alloys, thickness fluctuations, and other artifacts.

For this research work, XRD measurements were accomplished using a high-resolution Bruker D8 diffractometer, Cu_K_alpha = 0.15406 nm, *figure 4.1*, employing a scintillator detector with a mechanical slit of 3 mm. The equipment is located in Peter Gruenberg Institute-9 facilities at the Forschungszentrum Jülich. The scans were carried out in a range from 2Theta = 3° – 140° with an angular resolution of 0.1°. Each data point was measured for 10 s.

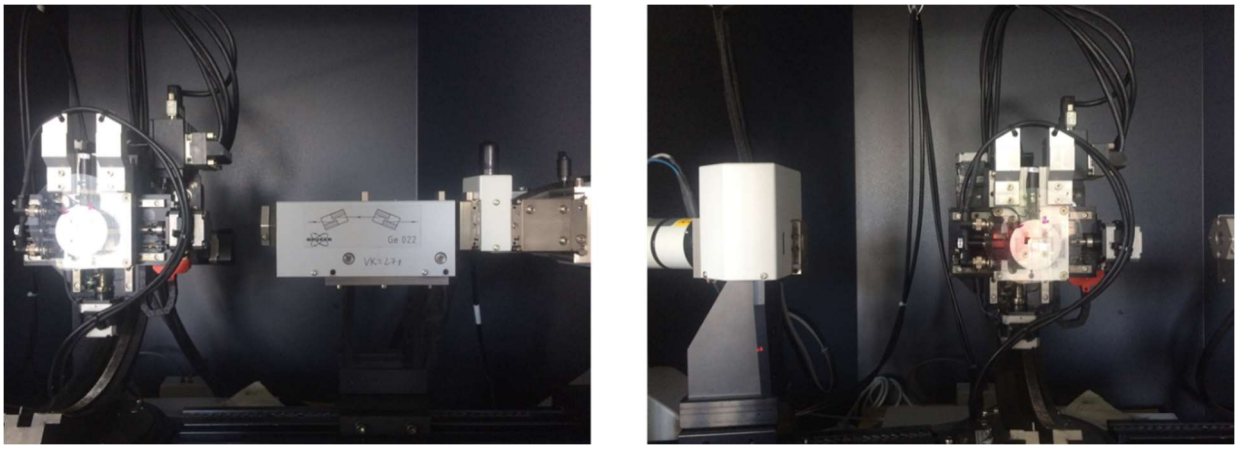

Figure 4.1: *The XRD instrument used for measurements, located at PGI 9 Institute, Forschungszentrum Juelich, Germany.*

4.4 SEM, TEM, HRTEM, STEM, and EDX.

Scanning electron microscopy (SEM) was also applied to investigate the properties of the free-standing sample. The measurements were performed at the imaging facilities of HNF Jülich, using an FE-SEM ZEISS SIGMA 300 (field emission-scanning electron microscope), at the accelerating voltage of 20 kV.

Transmission electron microscopy (TEM) is an imaging technique that uses electrons passing through a thin (preferably less than 100 nm) specimen. It provides information on the atomic arrangement of atoms due to its high spatial resolution (down to few angstroms not achievable standard microscopes). Therefore, the crystal structure of crystalline materials may be accessed directly from atomically resolved TEM images. Due to the small de Broglie wavelength of electrons, resolutions below 0.5 Å can be achieved [52, 53]. At lower magnifications, TEM image contrast is caused by differences in composition, density, or thickness of the material. Therefore, macroscopic strain effect can be observed. At higher magnifications, fine details as small as single columns of atoms can be resolved. TEM is usually coupled with EDX spectroscopes (Energy-dispersive X-ray spectroscopy) in order to provide elemental analysis of specimens with much higher resolution than EDX in SEM.

Before imaging the sample for TEM, the specimens were prepared using the focused-ion-beam (FIB) based method: a small area of the sample is coated with Pt, and a beam of Ga ions cuts a thin sample section, called "lamella" [54]. After separation from the initial sample, the obtained specimen can be further thinned and studied with TEM. In this way, the thickness of a film can be determined.

Figure 4.2: *FEI TEM TECNAI instrument, ER-C 1 Institute at Forschungszentrum Juelich.*

An image in TEM is formed either by using only the central spot or some of the scattered electrons. An aperture into the back focal plane of the objective lens is used to block out selectively part of the diffracted electrons, choosing the way to form the image. A unique mechanism inside the TEM is that the user can drive the desired aperture so that either the direct electrons or some scattered electrons are imaged. If the direct beam is selected, the resulting image is called a bright-field (BF)

image; and if the scattered electrons of any form are selected, it is called a dark-field (DF) image. The difference between these two modes is that the image contrast is inverted in the relation of one to another. It happens due to the mechanism of image formation in each case. Since BF images are formed by weakening the direct beam upon interaction with the sample, the correspondent mass-thickness contrast takes place. The areas in the sample that contain heavier elements appear darker. For DF images, the diffracted beams are the main contributor to the image formation; thus, it provides information about the crystal lattice such as imperfections and a more reliable composition contrast. When the contrast is formed by the phase differences of the electron wave, then it is called a phase-contrast, happening when a large objective aperture is selected, allowing a more extensive number of electrons with different phases to go through and form a high-resolution image (HRTEM). A typical HRTEM micrograph contains information about the orientation of atoms and spacing between them through the lattice fringes. In addition, a Fast Fourier Transform (FFT) can be applied to a selected portion of an HRTEM image to generate a diffraction-type pattern and to determine the crystalline structure of the deposited film.

STEM is similar to TEM. While in TEM parallel electron beams are directed perpendicular to the sample plane, in STEM the beam is focused at a large angle and converging into a focal point. The transmitted signal is collected as a function of the beam location as it is rastered across the sample [55].

There are multiple detectors for STEM imaging:

1. BF (bright-field) detector: small angles (<0-10 mrad). If a small detector is placed on axis, this records the bright-field intensity and yields images similar to BF TEM.
2. ADF (annular dark-field) detector: larger angles (10-50 mrad). A ring detector that integrates the intensity scattered sideways over a larger angular range. The ADF intensity doesn't include a single diffraction spot but an azimuthal integral over all diffraction spots and diffusely scattered intensity of the same distance from the optic axis, suppressing the diffraction contrast.
3. HAADF (high-angle annular dark-field) detector: Angles > 50mrad. It is used in the case of very short camera lengths, where the range of collection angles can become very large and comprise intensity scattered further out than any diffraction disk is visible. Using HAADF the total scattered intensity is then given by summation over the range of collection angles and over all atoms in the sample [55, 56].

The structural analysis of the samples in this work was accomplished in cooperation with the Ernst Ruska-Centre at the Forschungszentrum Juelich, GmbH. Samples were prepared Using FEI Helios Nanolab, and TEM images were performed using FEI Titan Tecnai G2 F20, *Figure 4.2.*

The FEI Helios NanoLab400S FIB-SEM is one of the world's most advanced DualBeam^{TM} focused ion beam (FIB) platforms for transmission electron microscopy (TEM) sample preparation, scanning electron microscopy (SEM) imaging and analysis in semiconductor failure analysis, process development, and process control. The FEI Helios NanoLab400S FIB-SEM combines an Elstar^{TM} electron column for high-resolution and high-contrast imaging with a high-performance

Sidewinder^{M} ion column for fast and precise cross-sectioning. The FEI Helios NanoLab ^{M} 400S is optimized for high throughput high-resolution S/TEM sample preparation, SEM imaging, and energy dispersive X-ray analysis. Its exclusive FlipStage^{TM} and *in situ* STEM detector can flip from sample preparation to STEM imaging in seconds without breaking vacuum or exposing the sample to the environment. Platinum gas chemistry is the preferred metal deposition when a high deposition rate and precision of the evaporation are required [57].

The FEI Titan Tecnai G2 F20 is a versatile transmission electron microscope that is equipped with a Gatan Tridiem 863P post-column image filter (GIF) and a high angle energy dispersive X-ray (EDX) detector. This set up allows for a variety of experiments such as conventional imaging and diffraction, recording of bright- and dark-field scanning transmission electron microscopy (STEM) images, or acquiring elemental maps extracted from energy electron loss spectra (EELS) or EDX signals [58].

4.5 X-ray photoelectron spectroscopy (XPS).

Photoelectron spectroscopy is based on the measurement of the energy of electrons emitted from a surface bombarded by a beam of x-rays [59]. Each atom has its signature. One of the essential capabilities of XPS is its ability to measure shifts in the binding energy of core electrons resulting from a change in the chemical environment of the emitting atom. In this way, the degree(s) of oxidation of each atomic species can be measured. The penetration depth of this chemical analysis is only a few nanometers (typically 25 Å in-depth to a maximum of 80 Å). Thus, surface contamination and surface oxidation have a significant influence on the results, and samples must be carefully prepared to obtain valuable information.

XPS measurements were performed on the sample by using the Phi5000 VersaProbe II, ULVAC-Phi Inc., USA. The instrument is operated at Al K-alpha, with a monochromatic source of 1.486 keV. The measurements were carried on three 200µm size spots, with 187.5 eV pass energy, 0.8 eV step, and 100ms/step. The results are presented with quantification in atomic percentage (at%) and 15% relative error, normalized to 100 at%, with a Shirley background and empirical relative sensitivity factors. The instrument is located at the Central Institute for Engineering, Electronics, and Analytics (ZEA-3) at Forschungszentrum Juelich.

4.6 Optical Characterization.

4.6.1 Transmittance measurements using a gas puff target EUV source.

The EUV source is based on the double-stream gas puff target approach [60]. The targets are formed by pulsed injection of high-Z gas (xenon, krypton, argon) into a hollow stream of low-Z gas (helium, hydrogen) using the valve system composed of two electromagnetic valves mounted

in a standard body and equipped with the double-nozzle setup. The outer stream of gas confines the inner flow improving the gas puff target characteristics (higher density of high-Z gas at a longer distance from the nozzle output). A strong EUV production from the double-stream xenon/helium gas puff target irradiated with nanosecond laser pulses from an Nd:YAG laser, exceeding production from solid targets irradiated in the same conditions, has been demonstrated [61].

Transmittance measurements of the filters were carried on at the Institute of Optoelectronics, Military University of Technology (MTU); Warsaw, Poland. The described EUV light source consists of a laser-plasma based on a double-stream Xe/He gas-puff target combined with a transmission grating spectrograph coupled to a CCD camera.

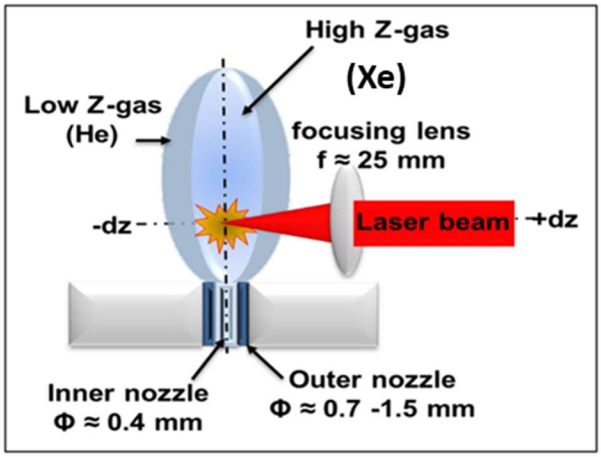

Figure 4.3: *Schematic diagram of the production of EUV plasma in a gas puff target setup.*

The experimental setup has three major components: a laser system, an interaction chamber with the electromagnetic valve to form a gas puff target, and soft X-ray measurement instruments. The laser system consists of a commercial Nd:YAG laser Continuum YG 682. Initially producing 10 ns FWHM pulses with energy up to 0.430 J. The soft X-ray emission spectra from laser-produced gas puff plasmas in the 1 – 22 nm wavelength range have been measured with the use of a transmission grating spectrometer TGS. The TGS consist of 5000 l/mm, 200 nm period + 32 μm entrance slit, to measure the spectra in the 5 – 22 nm wavelength range. The transmission grating was placed at 460 mm from the plasma.

All the spectra were recorded with a back-illuminated CCD camera Greateyes GE 2048 2948 BI placed at 90 mm from the transmission grating. Measurements were taken using the following parameters: 50 shots. 10 sec, 5 Hz.

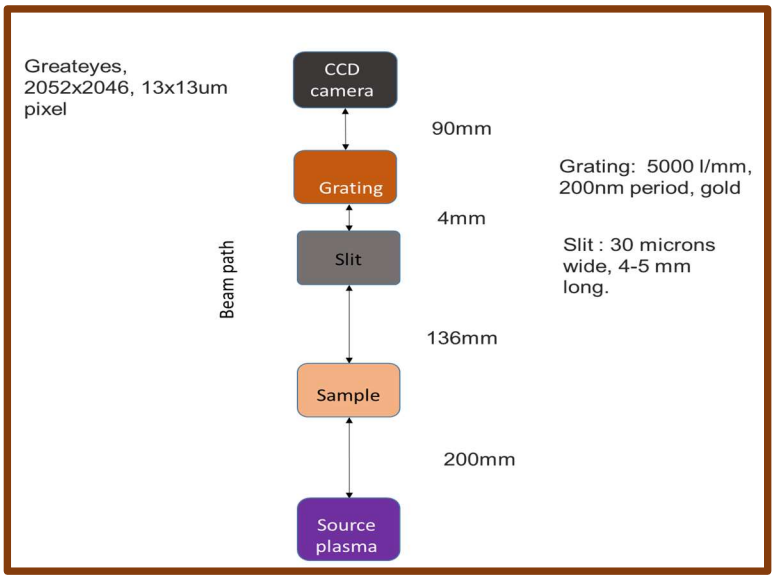

Figure 4.4: *Schematic diagram of the set up for doing transmittance measurements using a gas puff target source.*

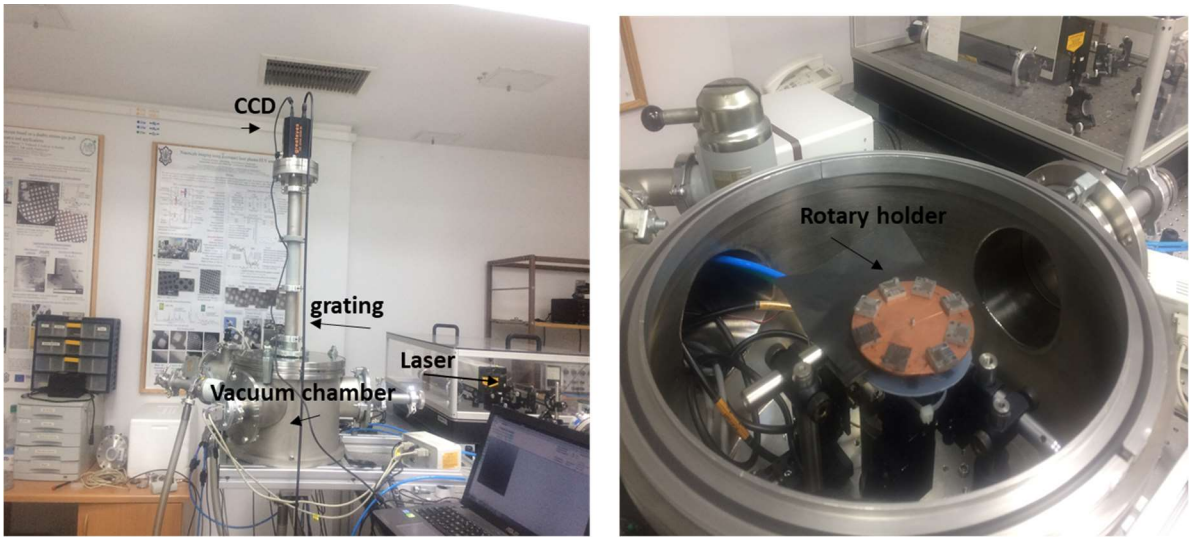

Figure 4.5: *Pictures of the setup for transmittance measurements located at the Institute of Optoelectronics, Military University of Technology; Warsaw, Poland. The left image shows the complete setup; The vacuum chamber connected through a metal tub with the grating and CCD camera. The laser is located behind the chamber in a glass box. The right image shows the vacuum chamber. The rotary holder with the samples can be appreciated.*

The vacuum chamber was equipped with a rotary holder with eight apertures, allowing us to measure seven samples without the necessity of breaking the vacuum. The last hole is reserved for measuring the direct light. A schematic drawing of the setup is shown in *Figure 4.4* and a picture of the setup used is shown in *figure 4.5.*

The results of the measurements performed are obtained in the form of spectrograms. The spectrograms are analyzed to be converted into numerical data. The calibration from pixel to wavelength is given by the diffraction equation customized with the geometrical configuration of the setup and the specifications of the grating and CCD camera used. *In figure 4.6* a schematic drawing of the grating-CCD camera geometrical configuration is presented.

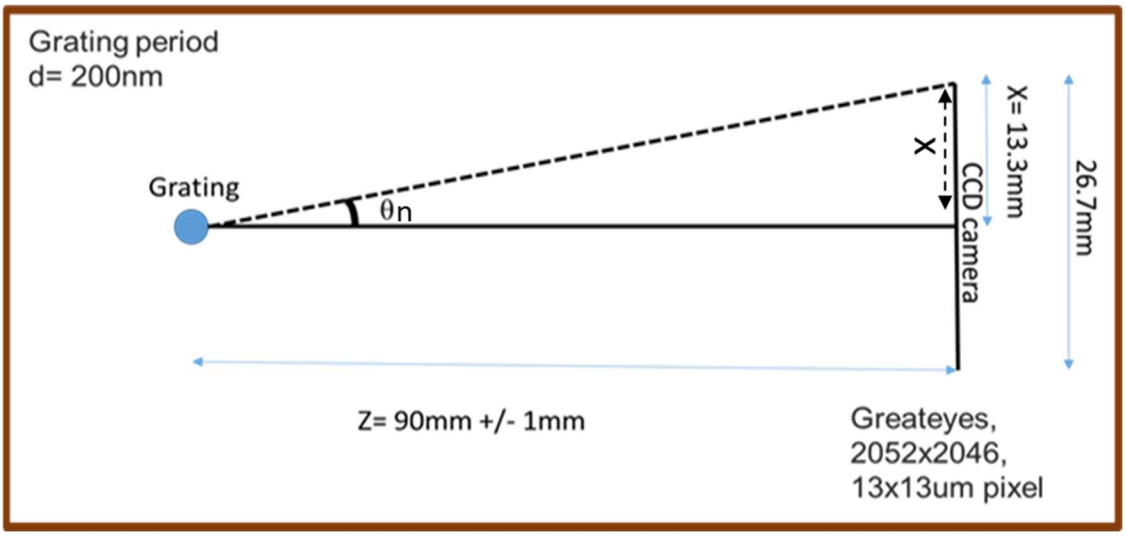

Figure 4.6: *Geometrical configuration of the grating and CCD camera, also grating and camera specification are shown.*

A diffraction grating with spacing d will deflect light at discrete angles θ_n, dependent upon the value nλ, where n is the order of principal maxima. The diffracted angle, θ_n is the output angle as measured from the surface normal of the diffraction grating. Using the diffraction equation:

$$dsin\theta_n = n\lambda \qquad 4.3$$

where λ is the wavelength.

From the geometrical configuration grating-camera, see *figure 4.6,* taking into account that for n=1 the angle θ is very small so: $sin\,\theta \approx tan\theta$; then:

$$sin\theta_n \approx \frac{X}{Z} \qquad 4.4$$

where the length X is the number of pixels in the spectrogram, max corresponding to 1023, multiplied by pixel size in our case 13 μm. The result of that value is marked in the drawing. Knowing that the period of the grating used is 200 nm; then, solving for equation 4.3

$$\lambda \approx d\frac{X}{Z} \approx 29.9\,nm \qquad 4.5$$

This value corresponds to the maximum wavelength possible to detect, the upper limit. The values of X and λ are used to calibrate from pixel to wavelength during the analysis of the data. The spectral resolution is:

$$\Delta\lambda \approx 0.029 \text{ nm} \qquad 4.6$$

4.6.2 Transmittance measurements at synchrotron facilities.

The transmittance measurements of the filters also were carried out at two synchrotron facilities:

- *BEAR beamline of ELETTRA – Synchrotron, Trieste, Italy*
- *Optics Beamline at BESSY Synchrotron, Berlin, Germany* [62].

a) Experimental setup at BEAR.

BEAR is a bending magnet beamline dedicated, among others, to reflectance and transmittance measurements [63, 64]. It covers an energy band from visible light to 1.6 keV, delivering radiation with well-defined spectral purity properties.

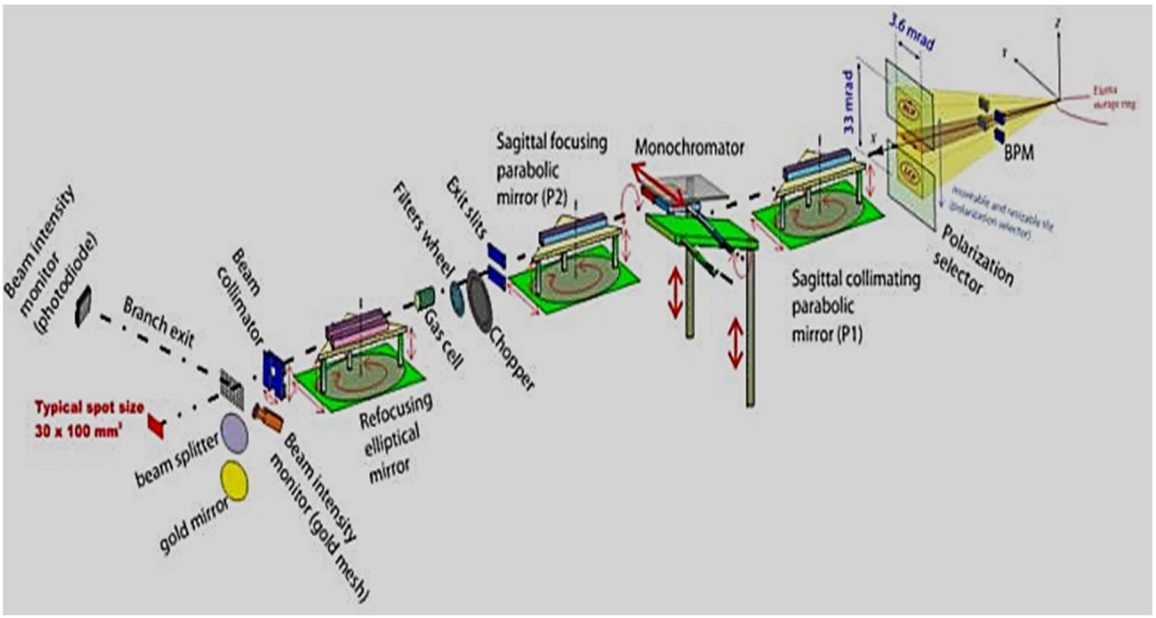

Figure 4.7: *BEAR beamline of ELETTRA – Synchrotron, Trieste, Italy. Movements of the beam are monitored by a photon beam position monitor (BPM) installed at the beginning of the beamline. Then, the beamline is equipped with a device for selecting the polarization of light. The PMGM (Plane Mirror Plane Grating) configuration is based mainly on a first parabolic mirror, collimating the light emitted by the BM source without any entrance slit, a monochromator.*

The sample chamber is equipped with motors enabling movements of the sample holder in all directions (six degrees of freedom), accurate alignment, and scans in a vast angular range. Finally,

a sample insertion chamber with a locking transfer system allows to change and insert samples without venting. *Figure 4.7* shows a schematic of the beamline.
working in parallel light at variable deviation angle, a second parabolic mirror focusing the dispersed beam onto the exit slit, and finally an elliptical mirror focusing the beam on the sample [63].

b) Experimental set-up at BESSY II.

The Optics beamline at BESSY II is a soft x-ray bending magnet beamline equipped with a plane grating monochromator, operated in collimated light. It is optimized to offer a proper resolution at very high spectral purity and efficient stray light reduction by a 4-mirror high order suppressor (HIOS) and filter and slit units (FSU). A permanent end-station, located in a clean-room hutch, accommodates a versatile reflectometer for at-wavelength metrology, covering the spectral range from 10-2000 eV [62]. Images of the set-up are shown in *figure 4.8*.

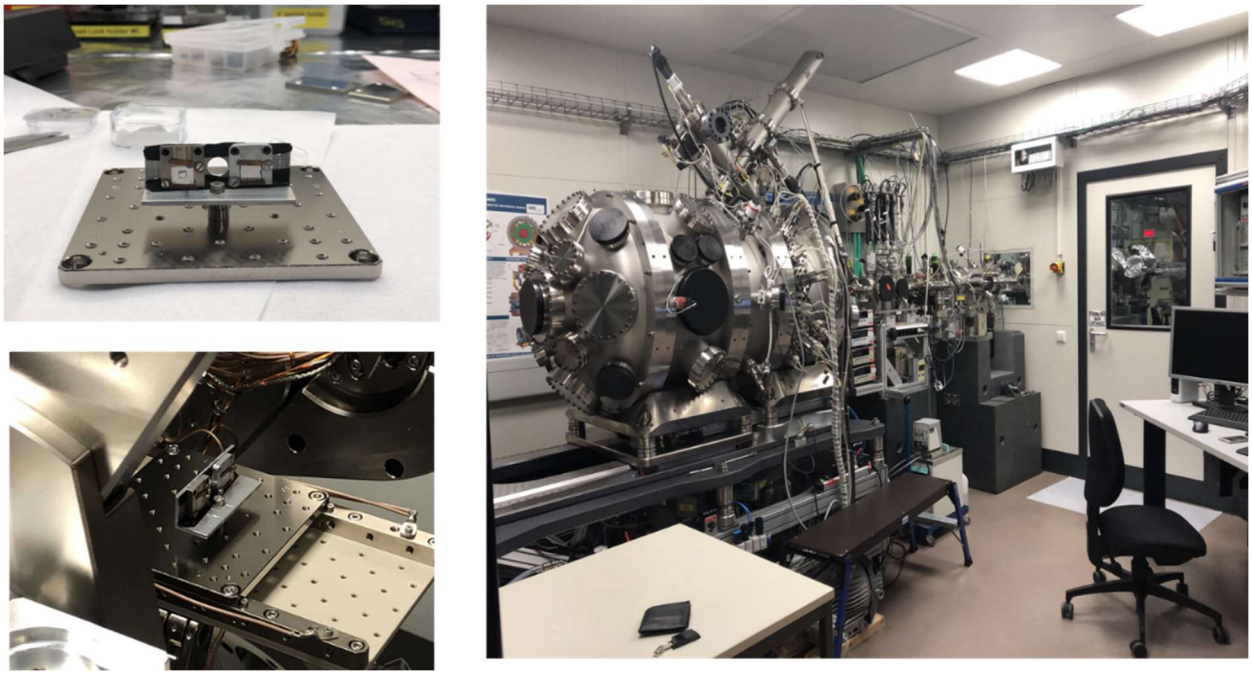

Figure 4.8: *Optics beamline at Bessy II synchrotron. In the left picture, the assembly of the samples can be appreciated; the holder used has three holes, one for measuring the direct light and the other 2 for samples.*

Chapter 5.

Mechanical and optical characterization of Nb/Si3N4, Zr/Si3N4, Zr/Nb/Si3N4, and Nb/Zr/Si3N4 filters (Experiment 1).

5.1 Introduction.

In this part of our research, we investigated the optical and structural properties of Nb/Zr and Zr/Nb bilayer thin films for the development of free-standing transmittance filters in the EUV region between 5-20 nm wavelengths. Samples were deposited on Si_3N_4 membranes by magnetron sputtering technique using metallic targets of niobium and zirconium. For a better understanding of the performance of these structures and their optical and mechanical properties, single layers of Zr and Nb on Si_3N_4 membranes have also been deposited and studied. The thicknesses of the samples were measured by RBS spectrometry.

From multiple sets of samples that were deposited using magnetron sputtering technique, 7 of these samples were selected to resume our findings. The transmittance of 6 of the samples was characterized without etching the membrane. After the first round of transmittance characterization, we proceeded to complete the fabrication process by RIE procedure. After fabrication the samples were stored in air, each one mounted in a custom-made holder, in Polypropylene boxes of a similar size to avoid movement of the sample during transportation.

Fragile samples did not survive the etching process, but it was achieved successfully the etching of the membrane from Nb/Zr and Nb samples. These samples showed higher mechanical stability and toughness.

By etching the silicon nitride membrane, Nb and Nb/Zr self-standing filters were successfully obtained, with free-standing areas up to 3×3 mm^2 and 100 nm thickness. The transmittance of the Nb/Zr free-standing filter was measured. The results show the highest peak transmittance of 60% at 7.02 nm and very good performance in the target range. XPS, XRD, and SEM images were also used to characterize sample structure and chemical composition.

The transmittance of the samples has been measured using EUV radiation; the first try out was using a plasma source, based on gas puff target. Then, for more accurate measurements, samples were characterized entirely at BEAR beamline at ELETTRA and Optics beamline at Bessy II synchrotrons.

Using the plasma source, 30 samples were measured but due to grating defects and plasma fluctuations during the experiment, the measured values of transmittance are more qualitative than quantitative. Therefore, we will present only few results.

The samples used for this part of the research are presented in *table 5.1*, together with the characterization techniques applied to them.

Table 5.1: *The description of the samples used for the resume of the results of the research and measurements performed on them.*

Samples	Substrate (100 nm)	Nominal thicknesses of individual layers (nm)	The total thickness of the metal layer (nm) measured by RBS	Measurements performed				
				AFM roughness	Transmittance		XRD	XPS
					At BESSY II Three months after deposition	BEAR One year after deposition		
Nb	Si_3N_4	100	104	*		*		
Zr_1	Si_3N_4	100	108	*				
Zr_2	Si_3N_4	150	169			*		
Zr/Nb	Si_3N_4	50/50	103	*		*		
Nb/Zr_1	Si_3N_4	50/50	107	*	*			
Nb/Zr_2	Si_3N_4	50/50	107			*		
Nb/Zr_3	Etched (no - substrate)	50/50	107			*	*	*

5.2 Results and discussion.

After deposition, the samples were characterized by RBS in order to detect contaminants due to the fabrication process and raw materials impurities. The specimens mostly show oxygen contamination. The oxygen concentration is not uniform with depth: in some samples oxygen probably diffused from the outside due to the air exposure, in other cases a relatively large presence of oxygen at the interface substrate/film could suggest a gettering effect at the start of the deposition.

Table 5.2 reports a summary of the RBS results: for each sample, the main stoichiometry of the different layers was calculated. Since the density of the different detected compounds is unknown, the reported layer thickness was retrieved by assuming a hypothetical pure metal layer, the bulk metal density, and the detected amount of metal. Samples Nb/Zr_1, Nb/Zr_2, and Nb/Zr_3, were deposited together; then we are assuming the three samples have the same chemical composition. The oxygen contamination mainly affects the Zr_1, Zr_2, and Zr/Nb films.

Both Zr and Nb oxidize when they are exposed to air. Zr oxidizes at a faster rate than Nb as it is shown in *table 2*. From literature we know that the most common oxidation state of Zr, in thin metallic films, is ZrO_2, while for Nb is Nb_2O_5. The material's density changes with oxidation, producing the expansion of the thicknesses of the layers, resulting in the appearance of some intrinsic stress in the film. The lower rate of oxidation and possible plastic deformation of Nb layers could allow the relief of the residual stress [65-68].

Table 5.2: *The mean stoichiometry of different deposited layers calculated from RBS data. Thickness* is related to a hypothetical pure metal layer containing the detected amount of metal and having bulk density.*

Sample	**Nominal total thickness (nm)**	**Top layer (mean composition − thickness*)**	**Bottom layer (mean composition − thickness*)**
Nb	100	$NbO_{0.3}$ − 104 nm	−
Zr _1	100	$ZrO_{1.1}Hf_{0.01}$ – 108 nm	−
Zr_2	150	$ZrO_{0.1}Hf_{0.01}$ − 169 nm	_
Zr/Nb (Zr top layer)	100	$ZrOHf_{0.01}$ – 49 nm	$NbO_{0.2}$ − 54 nm
Nb/Zr (1,2,3) (Nb top layer)	100	$NbO_{0.1}$ − 50 nm	$ZrO_{0.4}Hf_{0.01}$ – 57 nm

Also, the strain strongly depends on the selected top layer. *Figure 5.1* depicts examples of filters grown with compressive and tensile stress. The top images of *Figure 5.1* refer to Nb and Nb/Zr_1 samples, with Nb on the top. In this case, a smooth homogenous structure with tensile stress is observed. The bottom images show Zr_1 and Zr/Nb specimens: the surface is wrinkled by compressive stress.

Regarding the nanoscale observation, the surface roughness of the Nb and Nb/Zr samples is almost the same as that of the substrate, while in the case of Zr and Zr/Nb structures the surface experiences an increase of roughness, particularly in the Zr specimen. The results of the morphology analysis performed by AFM are summarized in *table 5.3*.

The roughness and the stress of the films can affect the properties of the wave-front passing the filter, by inducing distortion of the incoming beam, also can affect the quality of the films and the mechanical stability of the filters. Furthermore, Zr and Zr/Nb samples exhibiting high surface roughness and compressive stress are not the best candidates for the etching process. In fact, they did not survive the etching.

The filters with the tensile strain (Nb and Nb/Zr_1), on the contrary, demonstrate a flat surface, suitable for achieving a successful etching process and for the manufacturing of the filter. The

reduction of the compressive stress is due to the presence of Nb as the top layer. The stress in Zr thin films could be related to the pronounced oxidation of Zr during deposition and the continuing escalated oxidization due to exposure with the air, after deposition [66, 67].

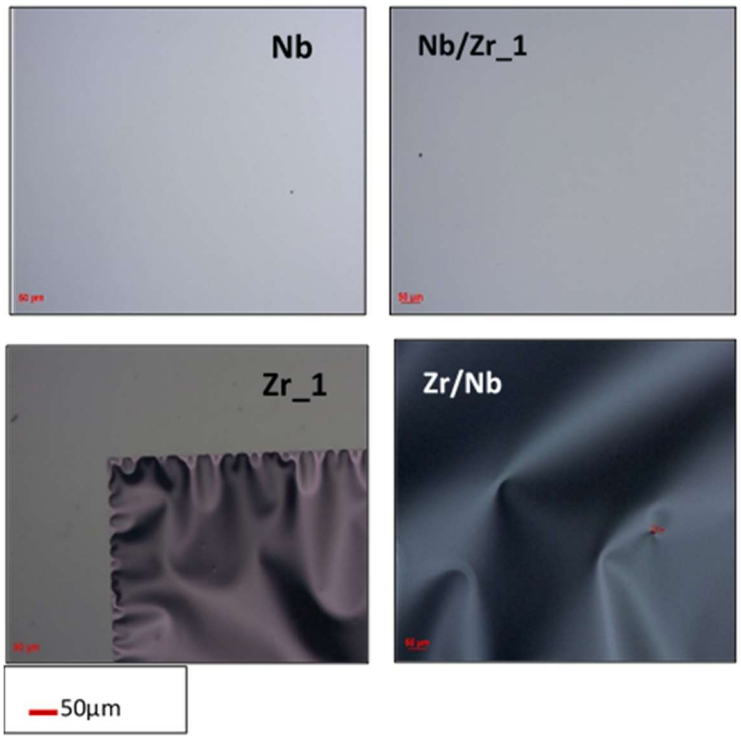

Figure 5.1: *Optical images of the surfaces of the different material samples on Si_3N_4. Nb and Nb/Zr, flat samples, grown with tensile stress (top images). Zr and Zr/Nb, wrinkled samples, grown with compressive stress (bottom images).*

Table 5.3: *Summary of surface roughness values measured by AFM*

Sample	Nominal thickness (nm)	Roughness (nm)
Si_3N_4 (substrate)	100	1.4 ± 0.2
Zr	100	3.4 ± 0.2
Nb	100	1.4 ± 0.1
Zr/Nb	100	1.8 ± 0.2
Nb/Zr_	100	1.4 ± 0.1

Figure 5.2 shows the optical microscope images of the Nb/Zr filter surface structure before and after the etching procedure. Due to the detachment of the silicon nitride membrane, we can observe how the membrane releasing changes the stress on the surface of the sample. The reason why the stress behavior goes from tensile to compressive is not completely certain; it could be because, without the substrate, the expansion of the Nb film due to oxidation is not compensated by the adhesion to the substrate.

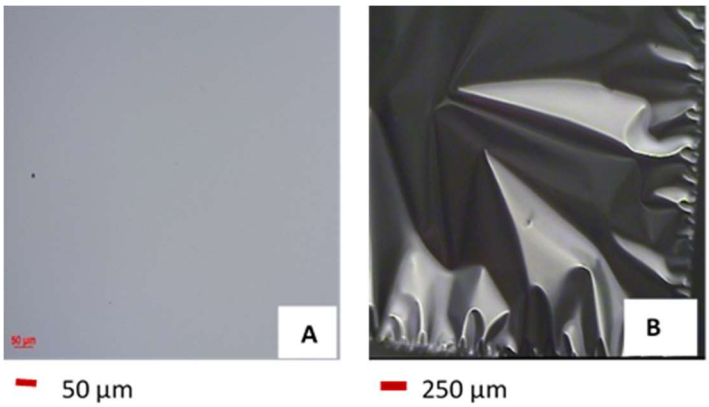

Figure 5.2: *Optical microscope images of the Nb/Zr sample before etching procedure (left) and after the etching procedure (right).*

5.2.1 Transmission measurements using a plasma source based on gas puff target.

The setup for the transmission measurements is described in the experimental part of this thesis, section 4.6.1.

During the measurement campaign, thirty samples were measured. Due to the fluctuations of the plasma and the lack of a reference monitor, the measurements of the sample can give us only a qualitative idea about the performance of the sample; because of that, later on, synchrotron transmittance measurements were pursued. In this thesis we will show only a few results.

For measuring the transmittance of the filters, the samples, already ensembled in a custom-made holder, were placed in the rotary holder of the measurement chamber. The rotary holder capacity is eight samples, one sample per aperture; Seven samples were placed, and one empty custom-made holder was situated in the eighth aperture to record the spectra of the direct beam. The spectra of the direct beam were recorded using the following parameters for the incoming radiation: 50 shots. 10 sec, 5 Hz.

After preparing the setup, a short trial measuring the direct beam was performed, in order to understand the behavior of the incoming radiation. In figure 5.3, two spectrograms obtained from the measurement of the direct beam are shown together with the Image J graph evaluating the zero-order radiation intensity.

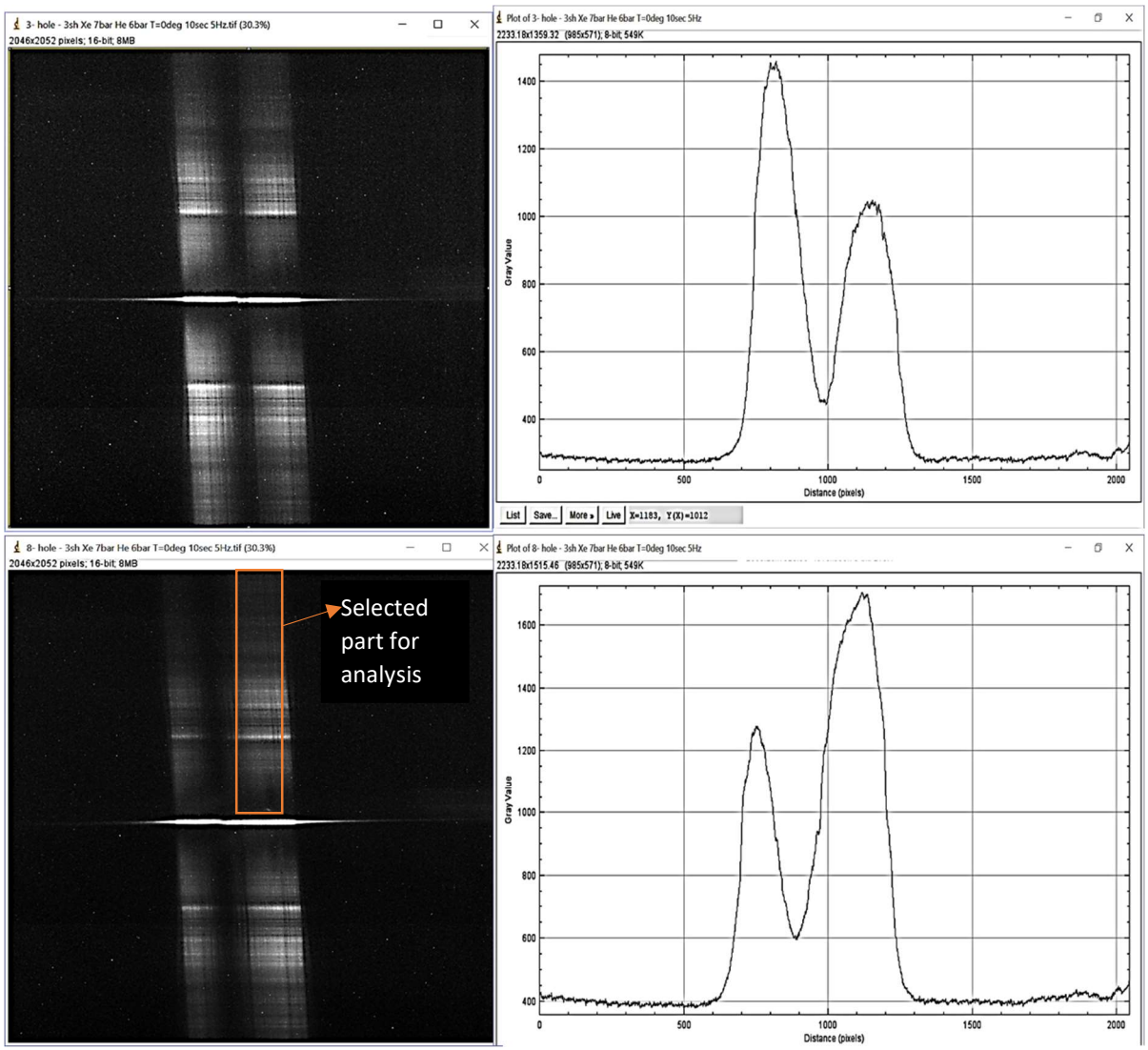

Figure 5.3: *Spectrogram obtained from the direct beam, 3 shots, at 5 Hz to the left. Image J analysis of the zero-order radiation.*

The measurements above were taken the same day with the same calibrations and specifications, 3 shots at a frequency of 5 Hz. From the images we can observe well-noticed fluctuations in the intensity of the zero-order. Besides, defects in the grating are detected, the zero-order is not homogeneous instead is split into two arms. A black band of missing information traverses the entire spectrogram.

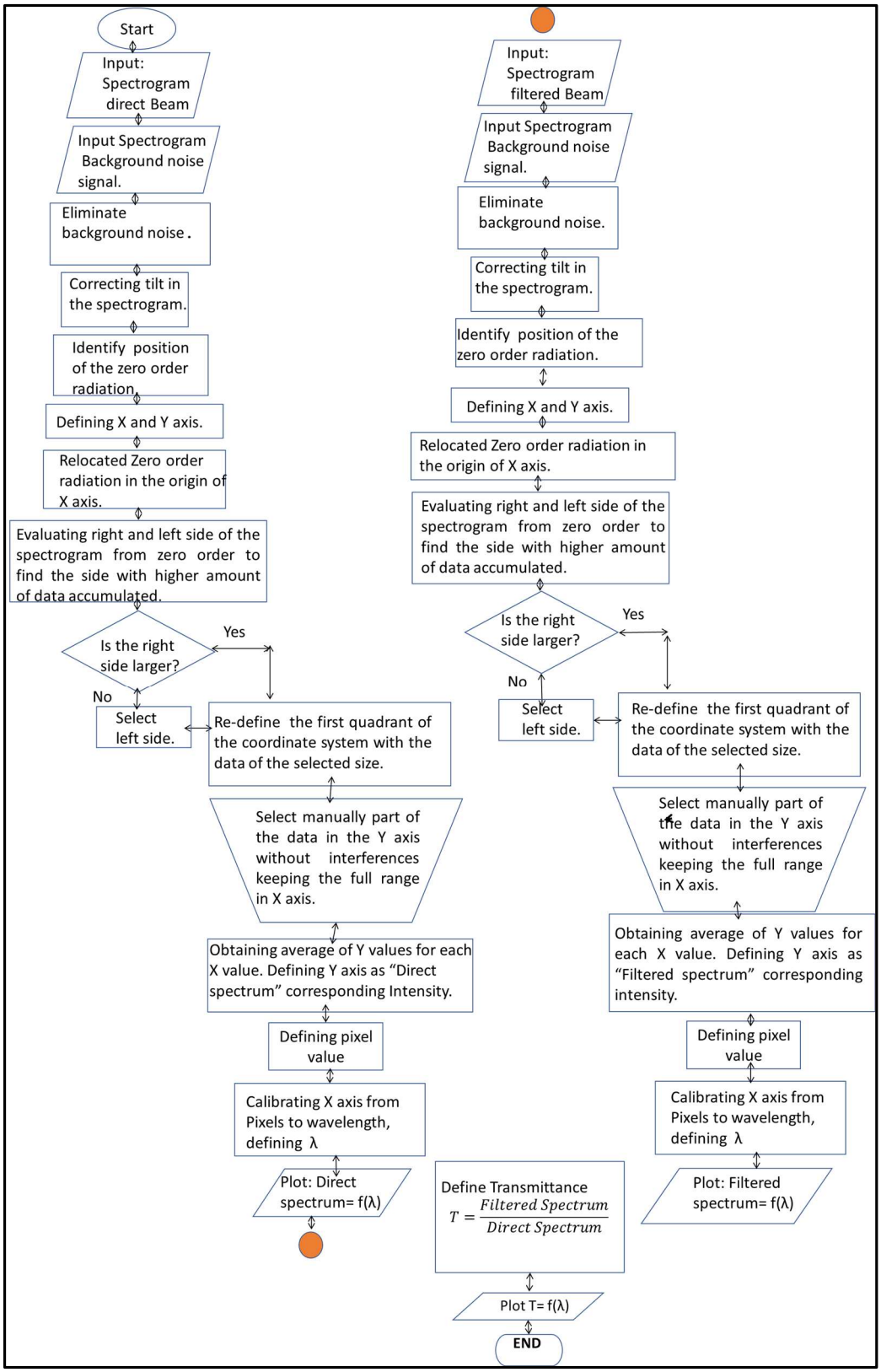

Figure 5.4: *Flow diagram of the MATLAB code created for analyzing transmittance data.*

For processing the transmittance data obtained during the experiment, an original MATLAB code was created. For a better understanding of the analysis of the data, the flow diagram of the created code is shown in *figure 5.4* and the code lines are described in Appendix A.

As we can observe, also in *figure 5.3* the spectrograms appear with a small tilt; which is corrected with a special function in the code. For managing the effects of the grating defects on the data obtained, only one of the two observed bands is selected and integrated for obtaining the total count numbers. This selection has to be done manually (for each filter and each direct spectra) obtaining the positions of the pixels that contain the desired data and inserting them in the code. Since the band from which the selected data will be chosen is decided by an optimization process in the coding, the positions of the data selected for the direct and the filtered beams are not always the same, this could create inaccuracy in the results. In addition, for the calibration from pixel to wavelength, explained in sub-section 4.6.1, an approximation for small angles is assumed to establish the wavelength's positions, this could also contribute to the uncertainties of the measurements.

The first sample measured was the Si_3N_4 membrane window. The background noise is also measured to be subtracted during the analysis. In *figure 5.5,* we can observe the results. In the top image, the comparison between the direct signal and the filtered signal through the membrane is presented. From a simple view, it is possible to deduce the average performance of the membrane. The bottom part shows that the transmittance performance of the measured membrane is resembling the expected simulated values. However, since we are not dealing with a monochromatic source, with the possibility of tuning to a particular wavelength, also taking in account the fluctuation of the emitted radiation by the plasma, and the grating defects: the accuracy of the measurements, in this case, is not as high as at a synchrotron-based setup. The highest peak of transmittance in the target wavelength range is 57% at 12.7 nm.

Figure 5.6 compares the transmittance of an Zr/Nb filter measured at MUT, using the plasma source as well as measured at BEAR beamline. Using the set of data obtained for the same samples, measured with synchrotron radiation and with the radiation produced by this source, a new improved MATLAB code can be written to improve the results. We can appreciate that the background base-line is high, maybe due to a low signal in specific ranges. Since the set-up was used without any mirror filter or transmittance filter but only the samples measured, the contributions of the second and higher diffraction orders of shorter-wavelength emission lines overlaying the measured spectra as well as grating deficiencies must be considered to improve the code.

The maximum transmittance peak for BEAR measurement was about 15% at 12.42 nm while the measured at Warsaw was about 12% at 12.46 nm; proving that Plasma set-up gives us a proper knowledge about the transmittance performance of the filter when the source signal is good. But it seems that for the transmittance from Warsaw there is a small displacement in the positions of wavelength in comparison with those measured at Bear, the reason of this displacement could be the assumed approximation in the calibration from pixel to wavelength inserted in the MATLAB

code; a correction factor should be calculated and integrated into the code to correct and improve the results. The deviation of the results obtained at MUT from the results obtained at BEAR are shown in *figure 5.6 and 5.7* in gradient colors.

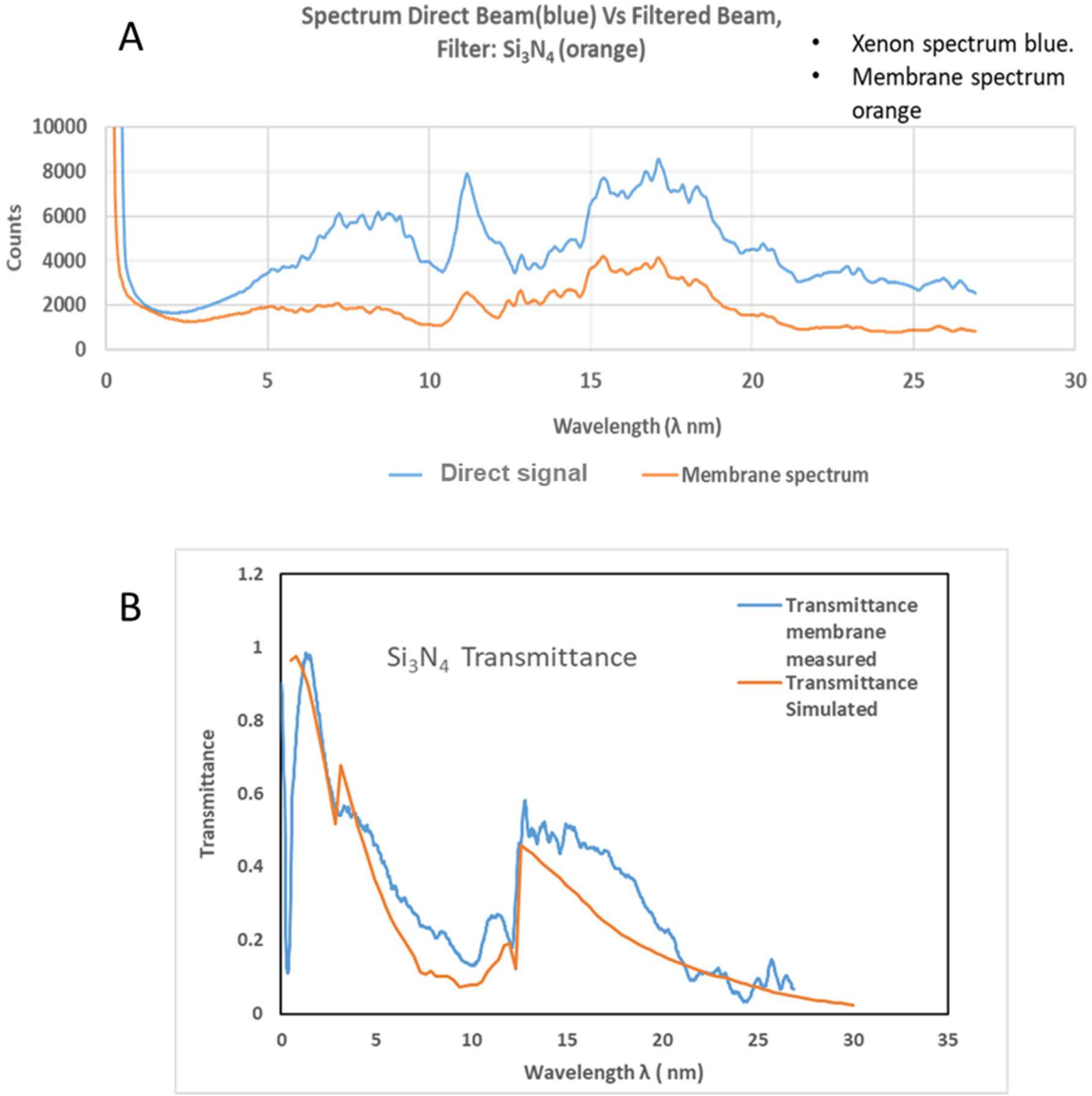

Figure 5.5: *In the top image, the signal of the Xenon spectrum (direct signal) is compared with the transmitted signal (sample). Bottom images show a comparison between the simulated transmittance of Si_3N_4 membrane (left) and the measured transmittance of a membrane window used for the fabrication of the samples.*

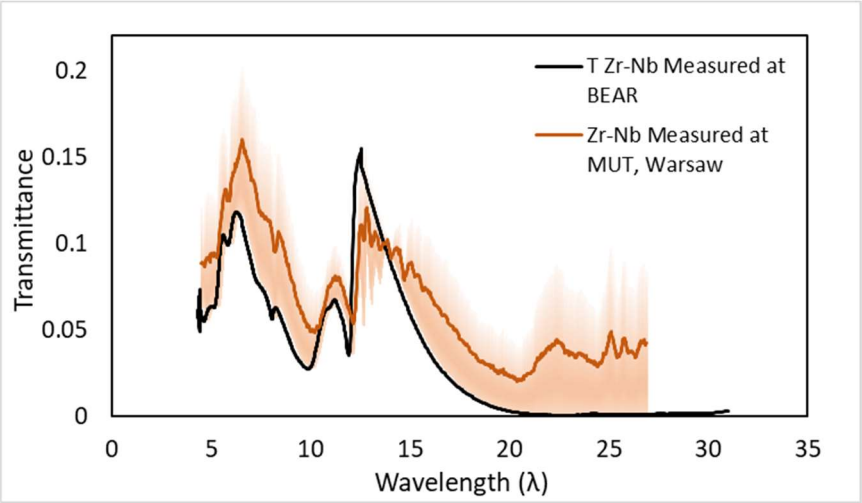

Figure 5.6: *Comparison of the results between the measurements performed at BEAR and the measurements performed at the MUT, Warsaw obtained for the transmittance of a Zr/Nb on Si_3N_4 membrane sample. The deviation of the MUT results in respect to BEAR results is presented in orange gradient color.*

In the case of the comparison of the measurement performed at BEAR with the one performed at MUT for Nb/Zr_3 sample shown in Figure 5.7, the transmittance peak value of the sample at BEAR is of about 27% at 12.42 nm while at MUT was about 24% at 12.61 nm. Here again, as in the comparison with the sample measured at BEAR, we can appreciate a difference in the position of the maximum value, confirming that a correction factor for calibration of energies should be pursued.

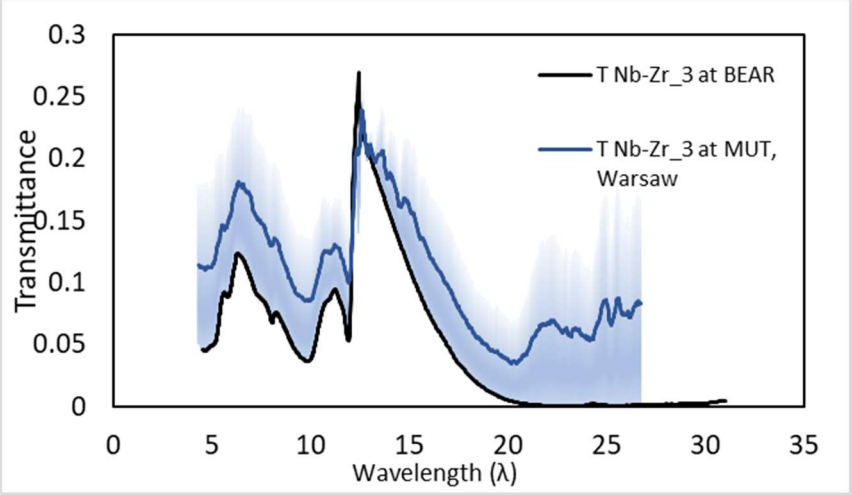

Figure 5.7: *Comparison of the results between the measurements performed at BEAR and the measurements performed at the MUT, Warsaw obtained for the transmittance of the sample Nb/Zr_3 on Si_3N_4 membrane. The deviation of the MUT results in respect to BEAR results is presented in gradient blue color.*

In general, plasma-based sources are proven to provide reliable and precise transmission and reflection measurements, not only in academic setups but also in stand-alone industrial tools. However, with line-dominated emission, careful wavelength calibration and processing of spectra are required; furthermore, a dedicated reference monitor is indispensable, but in our case the accuracy of the quantitative part is limited. A thorough characterization of the instrument should be done, and a more profound analysis method to process the results, specialized for this instrument, should be created in order to have more reliable results.

5.2.2 Transmission measurement results using synchrotron sources.

Transmission measurements were performed before the etching for the samples of interest in the EUV region 40-410 eV (3-31 nm) with steps of 0.2 eV.

In *Figure 5.8,* we present the results of transmittance measurements for Nb/Zr_1 (BESSY II) and Nb/Zr_2 (BEAR) samples. As mentioned before, they were deposited together in the same chamber; sample Nb/Zr_1 was measured three months after deposition while sample Nb/Zr_2 was measured one year after the deposition to evaluate possible effects of aging and contamination on the transmittance performance of the filters.

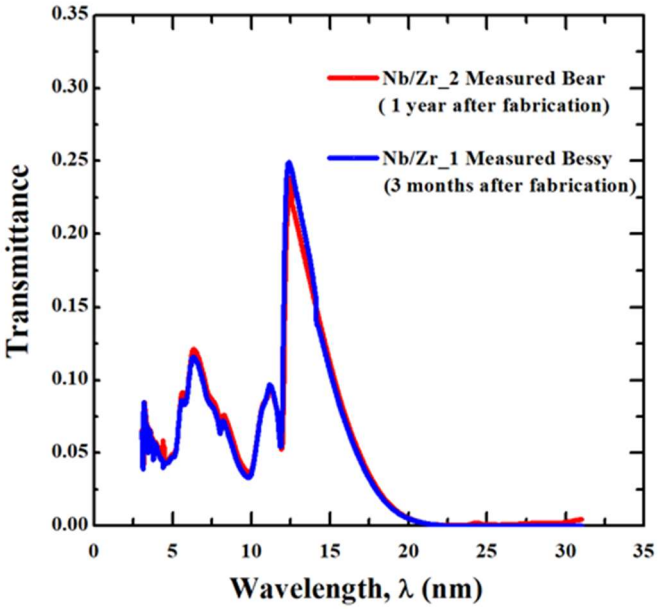

Figure 5.8: *Measured transmittance comparison between sample Nb/Zr_1 and Nb/Zr_2. Samples were fabricated together, in the same chamber; they have equal thicknesses. The transmittance of Nb/Zr_1 was measured three months after and Nb/Zr_2 was measured one year after fabrication.*

There is a minimal difference in the transmittance spectra of the two samples between 3 - 31nm. Since the samples characterized are not precisely the same, we cannot directly conclude that the slight reduction of performance is due to the aging. However, taking into account that the samples

were fabricated during the same deposition run and were kept in similar packing conditions, the results are a good indication of the chemical stability and wear resistance of Nb/Zr bilayer.

After one year, also the samples Zr_1, Nb, and Zr/Nb were characterized in terms of transmittance at BEAR beamline. The total thickness of the metal layers for all the samples is around 100 nm plus 100 nm of the Si_3N_4 membrane. The idea was to compare structural and optical performance of them. The 100 nm Zr sample appears more fragile than Nb one and bilayers. It is possibly due to the higher compressive stress that showed after deposition. During handling and measurement, the 100 nm Zr sample got broken. Then, we decided to use a thicker sample of around 169 nm of Zr (Zr_2) to study the properties of a single Zr layer.

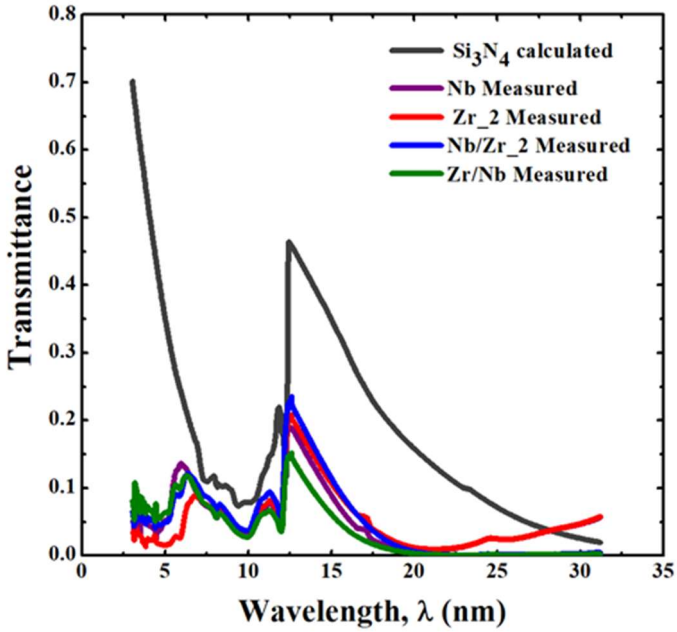

Figure 5.9: *Comparison of the transmittance values of all samples and the calculated values of transmittance for the Si3N4 membrane substrate.*

Figure 5.9, shows the experimental transmittance of the measured samples together with the transmittance curves obtained by IMD simulation using theoretical optical constants of the targeted materials assuming the RBS thickness results and no contamination. All the samples exhibit lower transmittance compared to the calculated data (the Si_3N_4 membrane was considered in the simulated curves). Besides the optical constants used for the simulation (LLNL_CXRO from IMD database), the discrepancy of transmission could have two possible causes:

1. A level of oxidation at the surface and inside the sample different from that calculated by RBS data.
2. A different kind of contamination on the surface of the samples.

The transmittance measured data of the filters was evaluated using the IMD optimization algorithm FOM Minimization-Genetic Binda, in order to determine the structure of the filter and the thicknesses of the layers. The mathematical formulation of the optimization procedure is found in

the IMD user's manual [34]. *Figure 5.10* shows a comparison between the measured curves of Nb and Zr_2 deposited on Si_3N_4 and the fitted theoretical curves. For the fitting the most common contamination elements carbon and metal oxides were added as layers. The composition of the filter's structure resulted from the fitting is shown in *figure 5.11.*

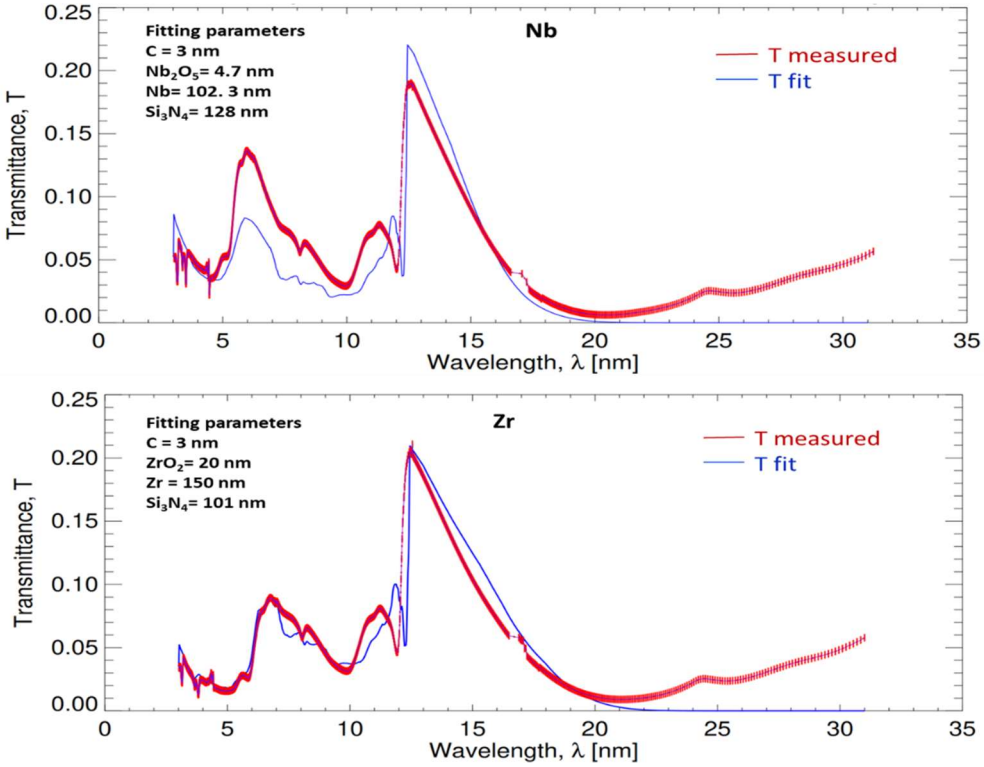

Figure 5.10: *Transmittance curves for Nb and Zr_2 deposited on Si_3N_4 membrane substrates, (not etched samples). The graphs show the comparison between the fitted curves and the measured values of transmittances for the different samples.*

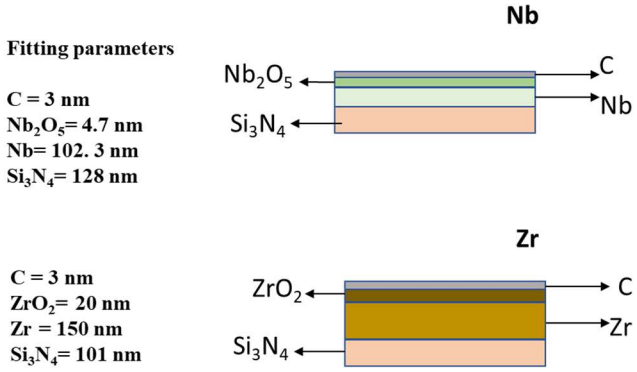

Figure 5.11: *Structures of the Nb and Zr filters on Si_3N_4 membranes resulted from the fitting of the measured data.*

Some studies have linked the compressive stress in sputtered zirconium thin films to the low pressure during the deposition and to the transition from metallic to oxidized film [66, 67]. As it was shown before, in *Table 5.2*, a higher concentration of oxygen was present in Zr/Nb specimens. It could mean an increase in oxidation of the sample, which explains the lower transmittance response.

For the same thickness, the stiffness of the Nb guarantees stable structures on the membrane [15], but with lower transmittance performance than Zr. The transmission of the Nb is slightly below of the widely used zirconium filters and below of the Nb/Zr free-standing filter, proposed in this thesis work (see *figure 5.12*). The bilayer structure of Nb/Zr combines the higher mechanical stability of Nb with the higher transmittance performance of Zr in this specific spectral region, resulting in the best candidate for free-standing filters.

Figure 5.12 shows the comparison between the measured curve of the bilayers structure Nb/Zr_2 and Zr/Nb deposited on Si_3N_4 and the fitted theoretical curves, again carbon and oxide layers were added for the fitting algorithm. In *figure 5.13* the fitted structure is presented.

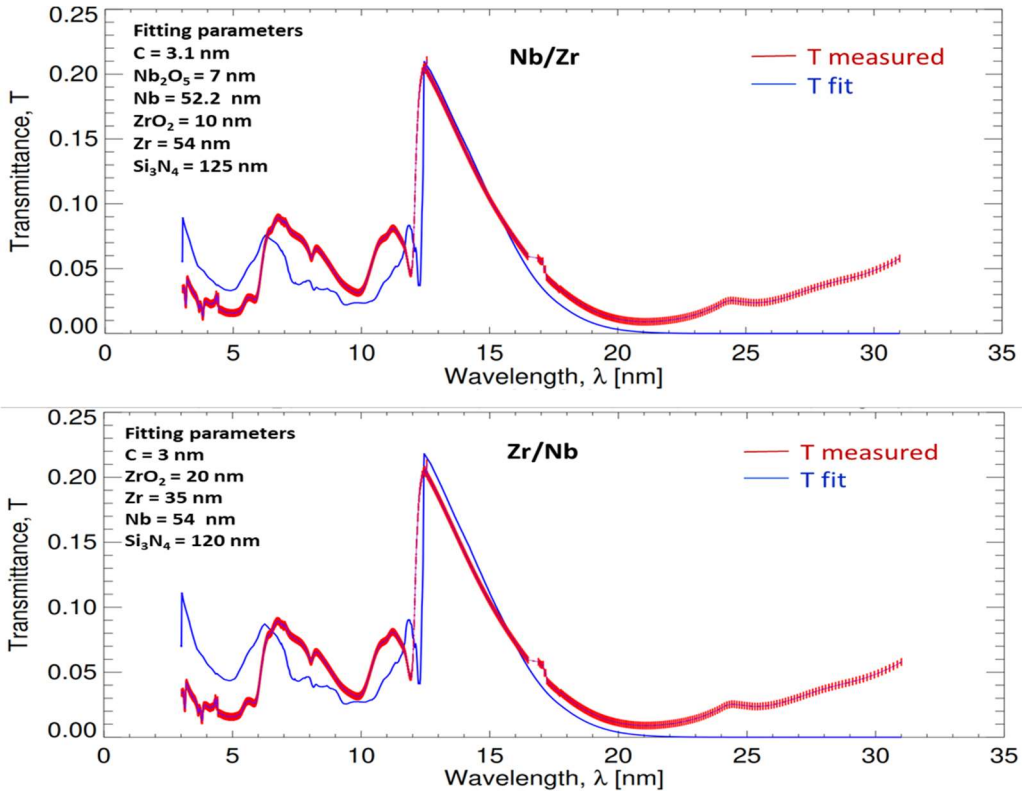

Figure 5.12: *Transmittance curves for the bilayers Nb/Zr and Zr/Nb deposited on Si_3N_4 membrane substrates, (not etched samples). The graphs show the comparison between the fitted curves and the measured values of transmittances for the different samples.*

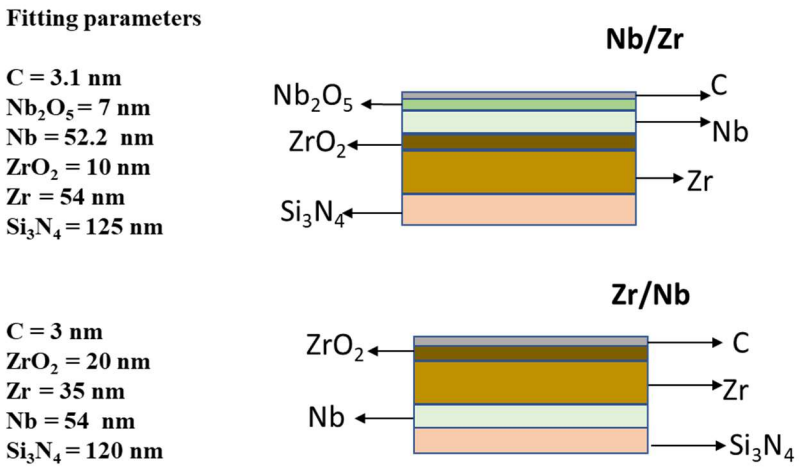

***Figure 5.13**: Structures of the Nb/Zr and Zr/Nb filters on Si_3N_4 membranes resulted from the fitting of the measured data.*

In all the cases the fitting results suggest a Si_3N_4 membrane thicker than the manufacture's values, carbon contamination is suggested to be around 3 nm in the four cases and the level of oxidation of Zr always exceeds the level of oxidation of Nb as it was expected.

After transmittance measurements the etching process was tried out on the four different types of samples, and as it was mentioned before, only Nb and Nb/Zr samples survived the etching process proving to have high mechanical stability.

5.3 Nb/Zr free-self-standing transmittance filter.

In this part, we mainly focus on the new free-standing Nb/Zr filter, which, based on simulated data, could offer higher transmittance performance than monolayer Nb of the same thickness. Sample Nb/Zr_3 (see *table 5.1*) corresponds to the Nb/Zr free-standing filter (etched sample). We did not test the Nb free-self-standing filter.

We performed XRD measurements of this sample. The spot of the x-ray beam with a size of 10 mm x 5 mm is larger than the membrane. Therefore, the Si frame is also measured in the x-ray scan, with a sharp peak around 70.0°. Besides the Si substrate peaks, signatures of the Nb/Zr epilayers were found. These peaks are attributed to the Zr in the hcp crystal structure at 32.2° and Nb in the bcc lattice configuration at 38.0°, as it is shown in *Figure 5.14*.

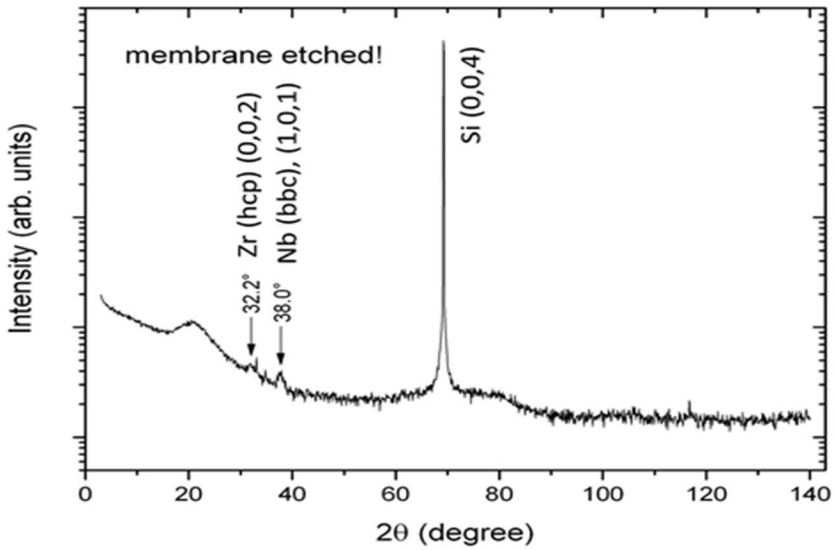

Figure 5.14: *XRD measurements. Signatures of Niobium and Zirconium were found, and also the signature of Silicon due to the frame of the samples.*

Due to the polycrystalline nature of the sample's structures, the picks are not strongly sharp but well identifiable. SEM images depict the surface of the Nb/Zr_3 (*Figure. 5.15*). In the left image, the filter window area and silicon frame can be distinguished; in the right, the polycrystalline structure is observed.

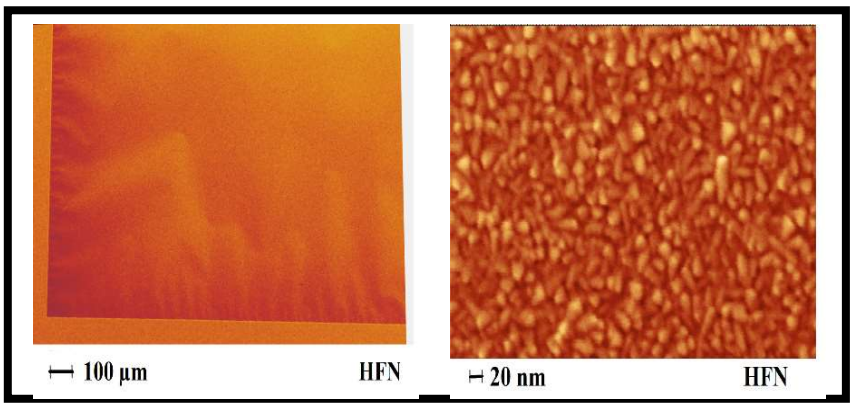

Figure 5.15: *SEM images of Nb/Zr_3 free self-standing filter of about 100 nm thickness. In the left image, it could be appreciated how the tensile stress was released. In the right, image of the surface nanostructure is shown.*

The transmittance of Nb/Zr free-standing filter was measured at BEAR beamline between 40-420 eV (3-31 nm). The beam passes through the sample entering from the vacuum to the Nb layer.

A rough transmittance scan, using the reading on the diode signal, was performed on the sample along horizontal (Y-axis) and vertical (Z-axis), using 40 eV photon energy for studying the uniformity of the filter. The results are presented in *figure 5.16*. The membrane window is about 3 mm x 3 mm. The signal is very stable inside the window area along both axes, demonstrating a uniform bilayer structure.

Subsequently, the transmittance was measured in the complete wavelength range. The results are in *Figure. 5.17.* The difference in transmittance before and after the etching procedure is shown in *Figure 5.17 left.* A considerable increase in transmittance is notable as it is expected after the membrane is removed. The filter possesses the highest transmittance's peak at 7.02 nm of about 60%. At 11nm the transmittance is 47.5%, a little bit lower than the results presented by S. Brose et all in 2012, but higher than for filters proposed by other authors [15, 25, 26]. Brose measured a Nb free-standing filter with 48% of transparency at 11 nm [15]. We present a broad-band characterization of the high throughput Nb/Zr free-standing filter developed in this work and thought for a wide wavelength range. The relative uncertainties in transmittance measurements at BEAR were less than 1%, the detail analysis of the calculation of uncertainties is described in appendix B.

Figure 5.17 right shows the comparison between theoretical transmission curves and measured one of the investigated filters. We present two theoretical curves: "Nb/Zr Calculated 1" corresponds to the IMD simulated transmission for 107 nm ideal Nb/Zr filter by ignoring any contamination or oxidation of the materials. As we can observe, the measured and Calculated 1 curves have significant discrepancies, then we simulated the transmission of a more realistic structure. In the "Calculated 2" curve, we considered the RBS thicknesses results, we simulated the Nb/Zr filter assuming a thin layer of Nb_2O_5, most common oxidation state for Nb thin film [68, 69], on top of the Nb layer and a thin layer of ZrO_2 at the interface [35, 66, 67].

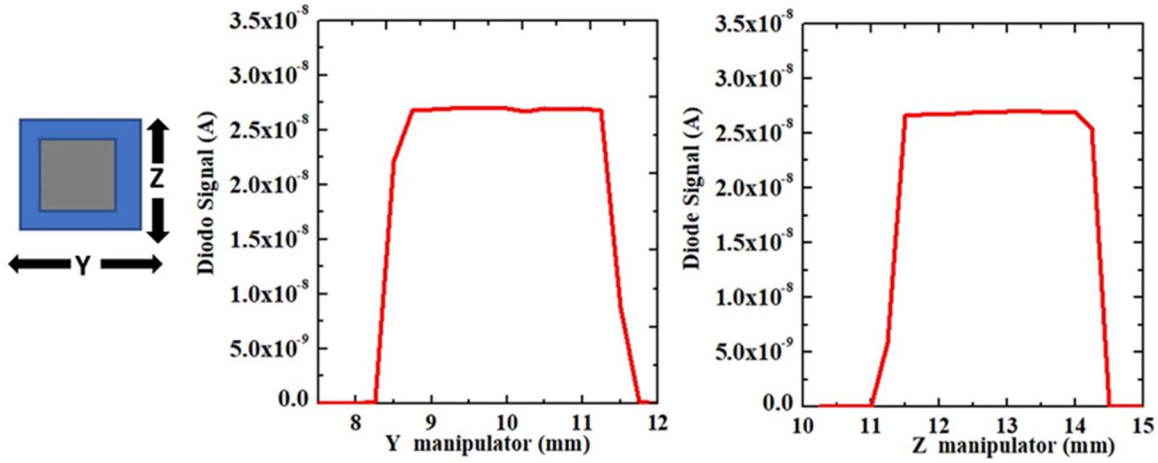

Figure 5.16: *Y and Z scan of the sample at a photon energy of 40 eV to study uniformity of the sample. The filter window is about 3 mm x 3 mm, and the transmitted signal looks very stable.*

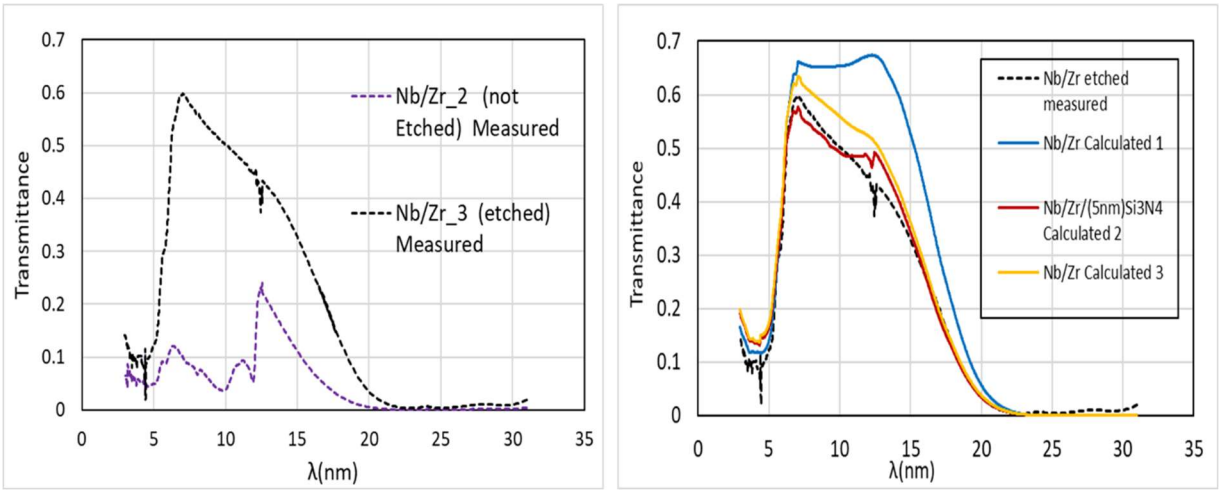

Figure 5.17: *Left: Comparison of transmittance values of Nb/Zr (Nb/Zr_2) before and after the etching process (Nb/Zr_3). Right: Comparison of measured transmittance values of Nb/Zr free-standing filter (Nb/Zr_3) in contrast with the IMD simulated transmittance considering only the nominal thickness of the sample in the Calculated 1 curve. The calculated 2 curve is simulated considering the nominal thickness, layers of oxidation of the materials, carbon contamination, and 5 nm of a residual Si_3N_4 membrane. 'Calculated 3' curve is simulated using the same structure of 'Calculated 2' but assuming complete etching (no residual membrane).*

Furthermore, since carbon is a common type of contamination on metal filters exposed to the environment, we added in the simulation 4 nm of carbon on the surface. In the model, a 5 nm thin layer of Si_3N_4 has also been added to the bottom of the structure to take into account the possible residuals of the membrane after the etching process. The final structure (*Figure. 5.18*) used for the simulation of the Calculated 2 curve is the following, from top to bottom:

1) C layer = 4.00 nm
2) Nb_2O_5 layer = 7.00 nm
3) Nb layer = 42.00 nm
4) ZrO_2 layer = 20.00 nm
5) Zr layer = 37.00 nm
6) Si_3N_4 layer = 5.00 nm
7) C layer = 5.00 nm

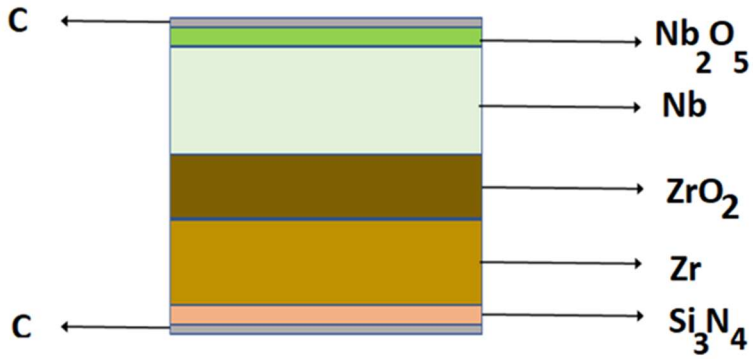

Figure 5.18: *Filter structure used for obtaining the transmittance simulated curve Calculated 2, which agreed more closely with the measured curve.*

Indeed, the measured and 'Calculated 2' curves are very similar. We can deduce that our hypotheses of contamination have some grounds. In the 'Calculated 3' curve, we consider the same carbon and oxygen contamination as in Calculated 2, but in this case, we are assuming a completed etching (no presence of residual membrane). The transmittance of the filter is improved in case of achieving complete etching. Furthermore, we can conclude that carbon contamination and oxidation of the metal layers are the higher contributors to the reduction of the transmittance performance of the filter. Some absorption features can be found in the measured data at 4.39 nm and 4.45 nm corresponding to the carbon K absorption edge and at 12.2 nm and 12.4 nm, where the LII and LIII silicon absorption edges are present. These lines are found not only in the experimental analysis but also in the 'Calculated 2' curve.

To test the hypotheses of surface contamination other than the initial oxidation levels found in the RBS results after the fabrication of the samples, XPS mapping in three different spots of the free-standing filter was performed. *Figure 5.19* shows the image of the three spots randomly selected to determine the homogeneity (about 8 nm in-depth) of the contamination at the sample surface.

Figure 5.19: *XPS analysis was performed in the 3 different shown spots. The measured were performed on the top layer.*

In *figure 5.20,* the XPS spectrum from one of the spots is presented, and in *table 5.4* results from the survey of the three spots are displayed.

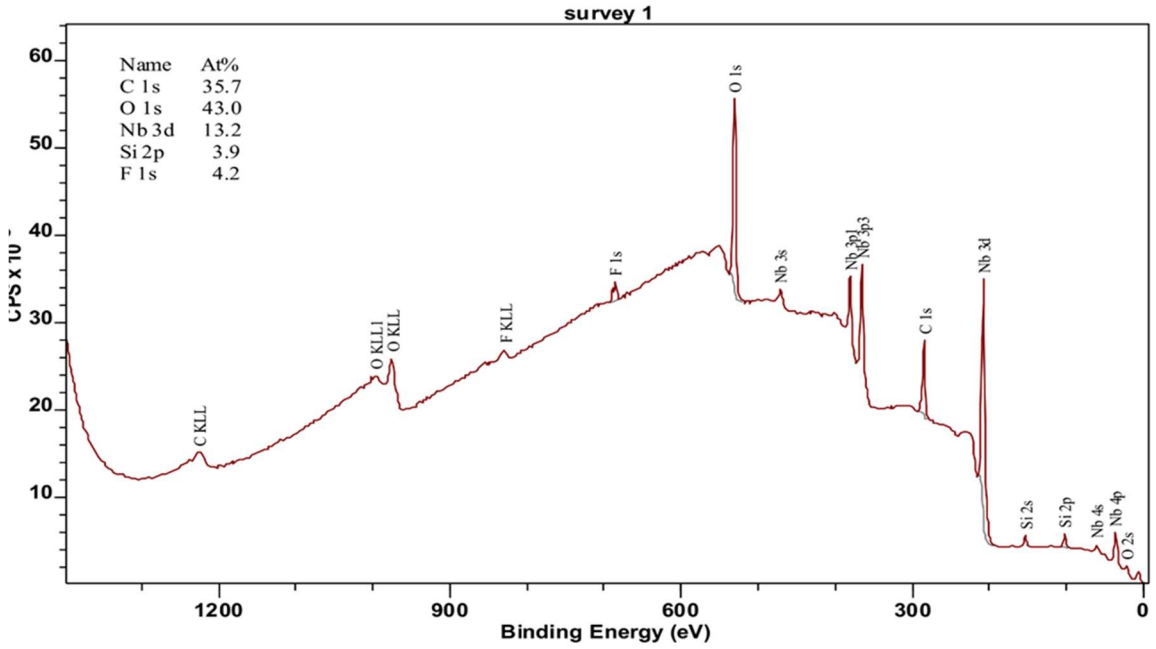

Figure 5.20: *XPS spectrum of one spot measured on the Nb/Zr free-standing filter.*

Table 5.4: *Quantification in at% of elements found on the surface of the free-standing filter. The analysis can reach between 5 to 8 nm deep.*

Elements found	**Spot 1 (At %)**	**Spot 2 (At %)**	**Spot 3 (At%)**
C	35.7	35.0	37.0
O	43.0	42.3	41.3
Nb	13.2	13.1	12.4
Si	3.9	4.7	4.5
F	4.2	4.9	4.8

The results indicate the presence of carbon contamination on the surface on top of a natural oxide layer of Nb_xO_x. Furthermore, some Si and F traces were found on the surface, not sure the source of Si contamination, but F contamination could be some residue from the etching procedure. The XPS results agree with the transmittance performance of the filter as we have shown in Calculate 3 curve.

5.4 Conclusions.

Nb and Zr have good transmittance performance between 5-20 nm, they are good candidates for EUV filters for FEL 2 at FERMI that cover specifically this range. The transmission of the Nb is slightly lower than that of widely used zirconium filters, but the higher stiffness of the Nb allows obtaining more stable filters of the same thickness. The use of the combination of these two materials, in bilayer structures, brings together the excellent transmittance performance of Zr and the stiffness of Nb which makes Nb/Zr an excellent choice for fabrication of thinner free-standing EUV filters.

The plasma source based in gas puff target set-up is useful to characterize the transmittance of thin films when high accuracy is not needed. It can be helpful to have an insight of the average performance of the filter or to have knowledge about the completeness of the etching procedure; comparing the measurements with expected values obtained by simulation. Since several samples can be measured in a short time without the necessity of open the vacuum chamber, the instrument set-up is time-saving. Synchrotron campaign measurement required months to be complete, from the time of submitting the proposal to the time of the actual measurements. Also, the measurement chamber, in case of transmittance measurement, can hold max two samples at the time, (at BEAR and BESSY) which means that only a few samples can be measured in each campaign.

Nb/Zr free-standing filters were obtained, showing a peak transmittance of 60% at 7.02 nm, this is the best-reported transmittance value until now, to our knowledge, for this wavelength. In the case of the filters on Si_3N_4 membranes, the maximum transmittance achieved was approximately 24% around 12.55 nm. Due to the high compressive stress of Zr and Zr/Nb on Si_3N_4 samples, etching the membrane was not possible. On the other hand, for the samples that showed flat, tensile stress surface, the etching process was successful, obtaining free self-standing Nb, Nb/Zr filters.

Additionally to the presence of a residual thin layer of Si_3N_4 at the bottom of the sample, assumed because the presence of the Si LII and LIII edges on the transmittance measurements, the XPS analysis of the Nb/Zr free-self-standing filter indicated that the reduction of the expected values of transmittance could be due to the surface contamination and some level of oxidation of the metal layers. It is recommended to grow an oxidation protection layer in situ with the metal material deposition to avoid progressive oxidation of the filters.

Chapter 6.

Structural Analysis of Zr/Nb, Nb/Zr, and Nb/Zr/Nb on Si3N4 membranes.

6.1 Measurements descriptions

We are interested in understanding the reason why Nb/Zr filters resulted, regardless of the type of deposition technique used during the fabrication, in a tougher thin film than the Zr/Nb filters. The study of the crystal structure of the sample and the interface properties using TEM, SEM, and STEM analysis could give us some insight into the answer. With TEM images we will be able to identify the crystal structure of the layers and see if there is any dislocation present in the layers or interdiffusion.

For this campaign of characterization, a new set of samples were fabricated. The fabrication of the samples was done following the procedure explained in chapter 3. On this occasion e-beam deposition technique was used to deposit the metal layers instead of magnetron sputtering. The samples were fabricated at HNF, Forschungszentrum Juelich.

To understand better the interface properties of the bilayer structures, besides the Nb/Zr and Zr/Nb samples, one sample Nb/Zr/Nb (three-layer) was also fabricated. Samples analyzed are presented in table 6.1. The calculation of the instrumental uncertainties, made by the technicians responsible for the e-beam deposition, predicted an error of +/- 5nm each layer.

Table 6.1: *The samples used for the structural analysis.*

Sample	Composition	Nominal thickness (nm) +/- 5nm/layer	Characterization technique	Si3N4 membrane (Substrate) thickness (nm)
1	Nb/Zr	47.5/47.5	TEM	10
2	Nb/Zr	50.0/50.0	XRD-TEM	100
3	Zr/Nb	70.0/50.0	TEM	10
4	Nb/Zr/Nb	25.0/50.0/25.0	TEM	100
5	Zr/Nb	50.0/50.0	XRD	100
6	Zr	100.0	XRD	100

The substrate used for the fabrication of samples 2, 4, 5, and 6 corresponds to the regular Si_3N_4 membranes described in section 3.1, while for the samples 1 and 3 a smaller substrate was used. The substrate has 1 mm x 1 mm Si_3N_4 membrane window, 10 nm thick with a Si frame of 200 µm thick. The substrate has a total area of 3 mm x 3 mm.

Before proceeding with the TEM study, samples 2, 5, and 6 were used for XRD analysis in order to have an insight into the structure of the samples, to find out if they were amorphous or

polycrystalline. As we expected, the samples resulted to be polycrystalline as we can observe in *figure 6.1.*

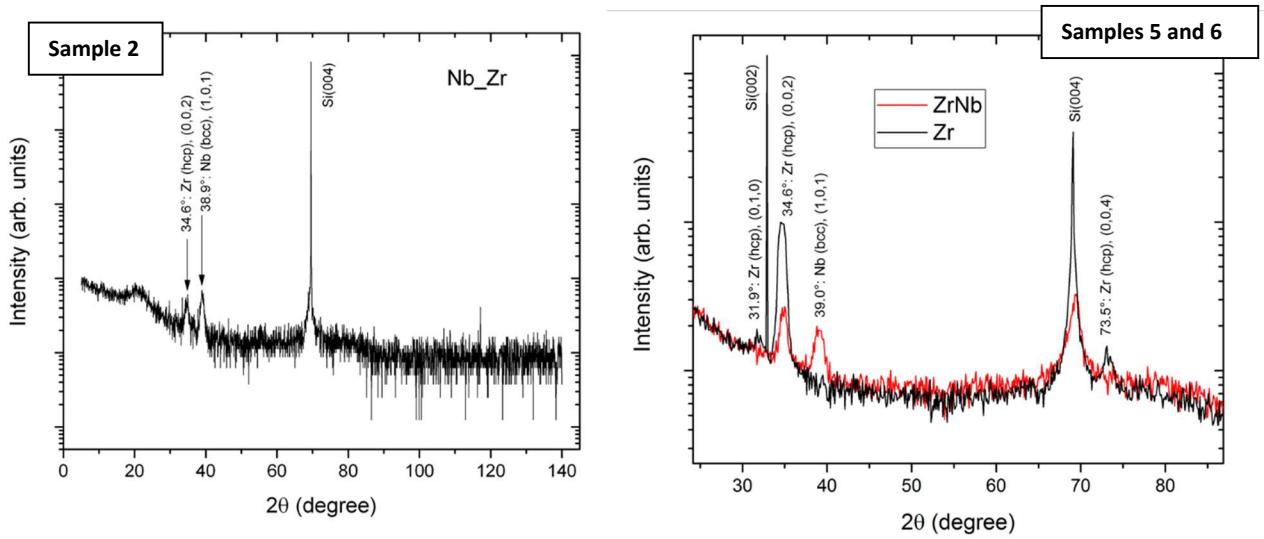

Figure 6.1: *XRD spectrum of 3 samples. In the left image Nb/Zr filter, and the right-side image, Zr and Zr/Nb filter XRD's spectrum.*

In the XRD spectrum of Nb/Zr, sample 2, *figure 6.1* left, we have found three distinctive peaks; one very sharp peak at around 70°, this is the signature of Si wafer [70, 71], since the XRD beam is larger than the membrane window and it detects also the Si frame of the sample. The other two peaks, very soft, at 34.6°, and 38.9° tell us that the composition of Nb/Zr filter is formed by Zr (hcp) (0 0 2) and Nb (bcc) (1 0 1) respectively [71, 72 73]. In *figure 6.1*, right, the spectra of 2 samples (5 and 6) are shown. The distinctive signature of Si is evident in both samples. The composition of the Zr/Nb filter is made by Zr (hcp) (0 0 2) and Nb (bcc) (1 0 1), as indicated by their respective peaks at 34.6° and 39.0°. Whereas in the Zr sample, an extra very soft peak at 31.9° is evidence of another orientation of Zr crystals present in the sample, which corresponds to Zr (hcp) (0 1 0) [74]. Furthermore, another crystal orientation for Si is also present. Although XRD analysis gives us some idea of the structure of the samples, since samples are polycrystalline with different crystal orientation and the XRD reveals very weak peaks, these results are not necessarily conclusive.

To perform the TEM study, four samples were used, samples are listed in *table 6.1*. These four samples were not etched, since in any case during the preparation of the sample for TEM specimen, (lamella) the filter is cut to be put in a TEM grid. To prepare the lamella, a platinum (Pt) protection layer is deposited on top of the sample, in this way, the layers of interest are "sandwiched" between the Pt layer and the substrate, *figure 6.2*."

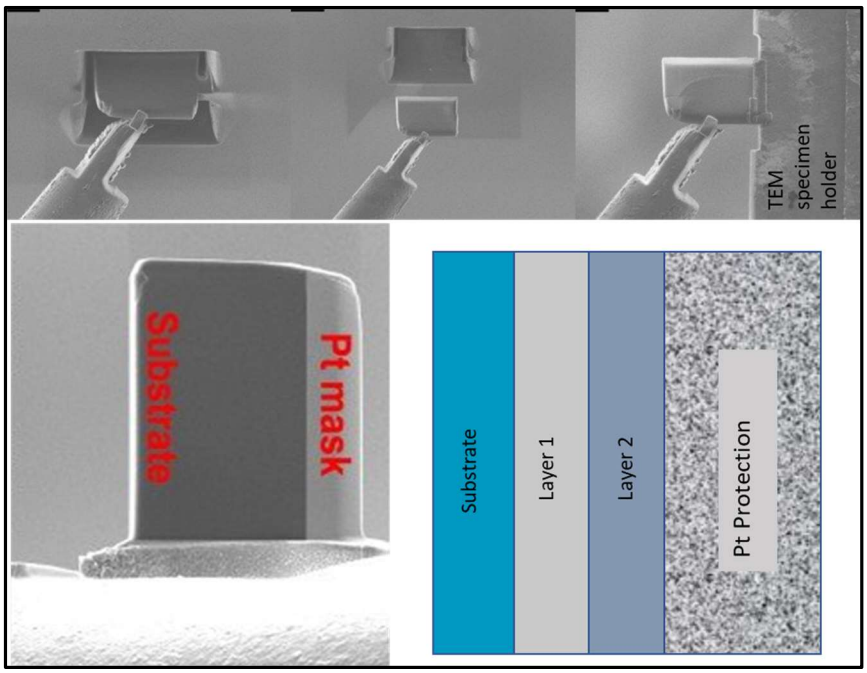

Figure 6.2: *FIB method sample preparation for TEM. Top: Cutting of the sample specimen and placement in the TEM holder. Bottom left: A quick view of a "sandwiched" TEM sample ready for measurements. Bottom right: A schematic of the profile view of a TEM sample in the way we will observe it in the next sections.*

SEM, TEM, and HRSTEM images were taken and processed depending on the different situations of each sample. Due to the limited time with equipment, not the same procedure was followed for each sample. BF STEM images in dm3 (Digital_Micrograph Image) files were used to obtain the diffraction pattern from the Fast Fourier Transform (FFT), this pattern was processed to index the crystal structure of the samples.

6.2 Diffraction in TEM.

When a collimated electron beam $\boldsymbol{k_0}$ pass through a thin sample, the beam is diffracted and a diffraction spot is formed. The vector connecting the diffracted beam $\boldsymbol{k}$ and the incident beam $\boldsymbol{k_0}$ correspond to:

$$\boldsymbol{g} = \boldsymbol{k} - \boldsymbol{k_0} \qquad 6.1$$

Where $\boldsymbol{g}$ is called the diffraction vector, see *Figure 6.3*.

If the sample is crystalline, the distances of the diffraction spots from the origin $\|g_{hkl}\|$ can be used to determine the corresponding planar spacing:

$$d_{hkl} = \frac{1}{\|\boldsymbol{g}_{hkl}\|} \qquad 6.2$$

when the diffraction condition is fulfilled, the geometry of the direct and scattered beams is similar to the reflection of light from planes. From Bragg's law:

$$2d_{hk}\ sin\theta = \frac{n}{\lambda} \qquad 6.3$$

In which $sin\theta$ denotes the Bragg angle of diffraction, n = 1 the order of the diffraction, and λ the electron wavelength [75].

For very thin samples, the Fourier transform of the diffraction pattern gives the projected interatomic distances. For the analysis of the FFT, ImageJ 2 from FIJI software [76] was used to find the experimental values of g vectors magnitudes. ImageJ's circle tool was used to measure the spot/ring patterns concentric to the (000) direct beam. From the area measured, the radius corresponding to $\|\boldsymbol{g}_{hkl}\|$ is found. From the values of $\|\boldsymbol{g}_{hk}\| = 1/d_{hkl}$ in reciprocal space, the d-spacing is calculated for each measurement made, see *figure 6.4*. For the calibration and analysis of the images, camera length and photon energy values must be known. The calibration of the instrument for the analysis of all samples and the camera length was determined using the Si diffraction pattern from the frame of the substrate confronted with the well-known Si standard diffraction pattern.

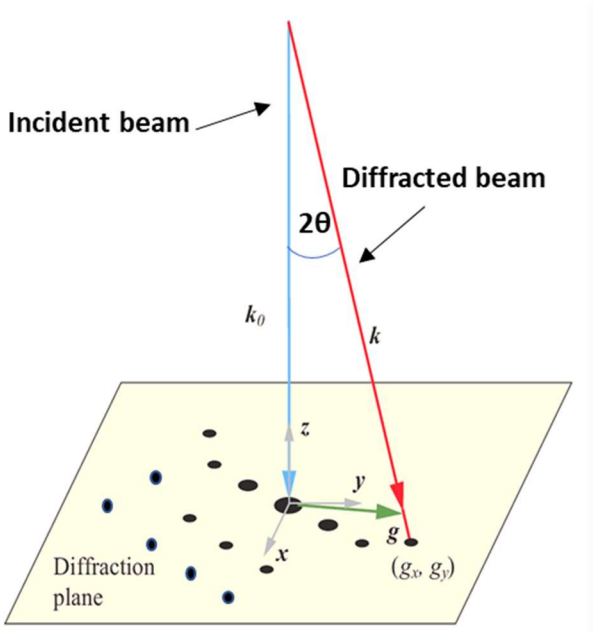

Figure 6.3: *Transmission electron diffraction geometry,* $\boldsymbol{\kappa_0}$ *represent the incident beam while* $\boldsymbol{\kappa}$ *represents the diffracted beam.*

These $\boldsymbol{g}$ values were compared with the theoretical values for the different crystal structures corresponding to the materials involved in each sample, Using the ICSD database [77].

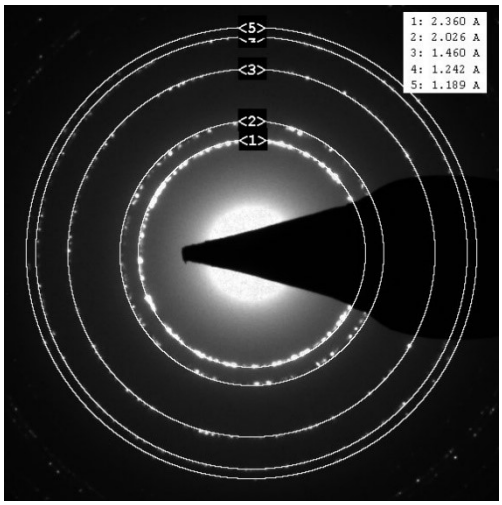

Figure 6.4: *Selected concentric diffraction rings from the diffraction pattern of a polycrystalline sample.*

6.3 Nb/Zr.

a) Sample 1.

BF TEM images of the surface of the cut lamella can be observed in *figure 6.5*. In BF mode the unscattered (transmitted) electron beam is selected with the aperture, and the scattered electrons are blocked. Since heavier atoms scatter electrons more intensely than lighter atoms, the regions with heavier atoms appear darker; in this way, Nb that is heavier than Zr is identified by the darker areas on the surface while Zr is identified by the lighter areas. Even though a thinner membrane was used, the sample is still very thick to appreciate in more detail the surface structure.

The diffraction pattern was obtained from the FFT of the bright-field TEM image (*Figure 6.5 top*). The diffraction pattern reveals a polycrystalline structure. We can observe five very intense rings while the rest are less bright. In *table 6.2,* the comparison of the g values for different crystal structures of Zr and Nb are presented. The best fit is marked in yellow cells.

Comparing the measured g values with the g values database**,** the best fit for Zr corresponds to Zr (fcc) of Fm-3m space group**.** All peaks of this structure are present and the ratios from the experimental pattern agree with this structure model, as it is shown in *table 6.2*. It is possible also that hcp Zr (P63/mmc) is present, its strongest intensities of (101) and (110) would overlap with the first ring, and this would agree with the previous results from XRD spectrum. *In table 6.2*, g values of hcp Zr appear in light blue cells.

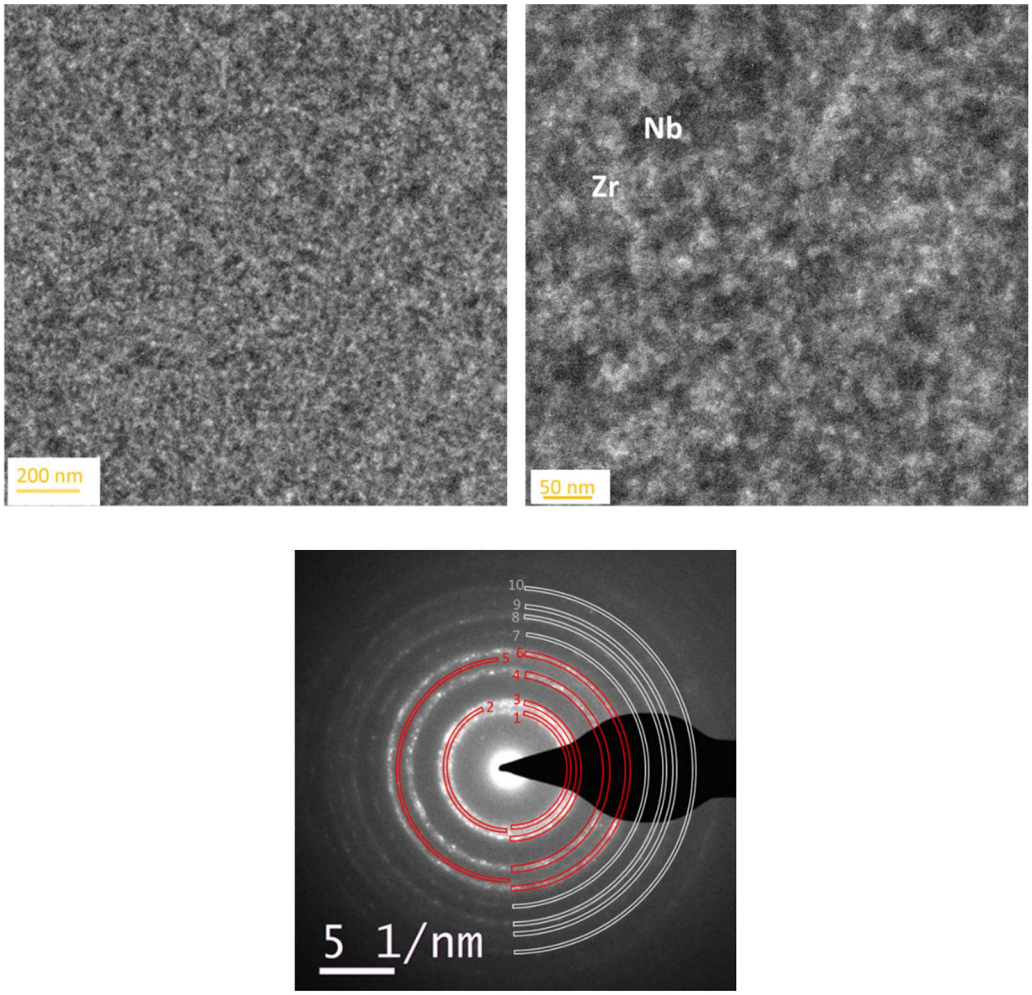

Figure 6.5: *Top: Bright field, TEM surface images of Nb/Zr/Si_3N_4. Zr and Nb phases can be observed. Bottom: Diffraction pattern obtained from the bright field image of the Nb/Zr sample; The calibration and measuring of the rings to obtain crystal structure are shown.*

Although all Nb reflexes overlap with some Zr intensities, taking into account the accuracy with the calibration of the images, possible cell size variations, and the broadness of the experimental intensities, the best fit for Nb corresponds to the Nb lm-3m (bcc from Bravais lattice) space group. Nb best fit is also marked with yellow cells.

Si diffraction pattern was used for the calibration of the instrument but also was analyzed. The structure model of Si was assumed to be Fd-3m space group (structure of mostly used Si wafers). However, Si could be excluded because its strongest peak of (111) planes is missing in the experimental pattern but some g values for Si could be overlapping with Zr pattern.

To finalize analyzing sample 1, a quick EDX analysis was also performed. *Figure 6.6* shows the results. Besides the elements of the composition of the sample and substrate, traces of Cu appear in the results. Cu contamination is not common in this kind of sample, but since the custom holders

(*section 3.1*) fabricated to keep the samples were made with bronze clamps, some residues of Cu could have been transferred to the surface of the filters.

Table 6.2: *Comparison between Experimental g values and Zr and Nb g values for different crystal structures. The best-fitted values are in yellow.*

	Experimental g (nm^{-1})	g_Zr Fm-3m (nm^{-1})	hkl	g_Nb Im-3m (nm^{-1})	hkl	g_Si Fd-3m (nm^{-1})	hkl	g_Zr P63/mmc (nm^{-1})	hkl	g_Zr P6/mmm (nm^{-1})	hkl
								3,57	100	3,92	101
1	3,8-4,0	3,82	111			3,19	111	3,88	002	3.97	110
2	4,2			4,28	110			4,06	101		
3	4,4-4,7	4,42	200								
										5,1	111
						5,21	022	5,28	102	5,5	201
										6.36	002
								6,2	100		
										6.85	211
4	6,6-7,0	6,24	220	6,06	200	6,11	113	6,8	103	6.88	300
5	7,5	7,32	311	7,42	211	7,37	004			7.5	112
6	7,8-8,2	7,65	222			8,03	113			7.94	220
7	9,1-9,3	8,83	400	8,57	220	9,02	224				

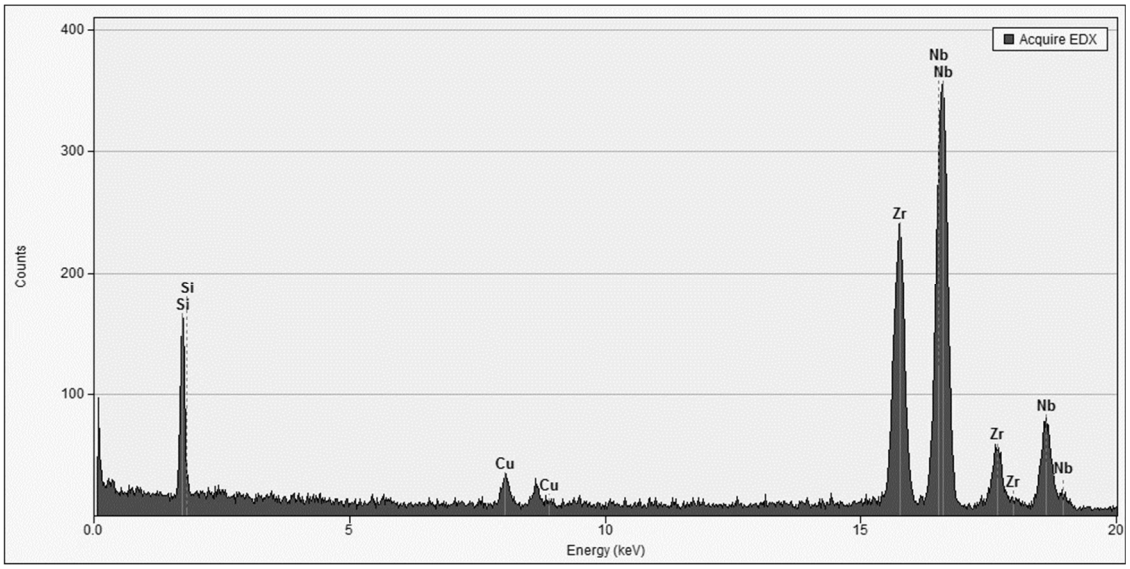

Figure 6.6: *EDX analysis of the Nb/Zr/Si_3N_4 Filter, peaks of Zr, Nb, and Si are present in the sample as it was expected. Surprisingly, Cu peaks are identified.*

b) Sample 2.

A Nb/Zr sample was used to study further the structural properties of this type of bilayer, having a close look at the interfaces. *Figure 6.7* shows SEM images of the cut lamella of the sample. In the top picture, the substrate can be appreciated. Since the TEM specimen was prepared using a cut from the Si frame of the filter, the red square is underlaying the Si at the bottom of the filter. The green square encloses the area of interest where the bilayer Nb/Zr is located. The yellow square denotes the Pt protection deposited on top of the filter. In the bottom picture the experimental values of the thicknesses of the Nb and Zr layers were obtained using SEM tools, revealing 47.50 nm for Nb layer and 47.50 nm for Zr.

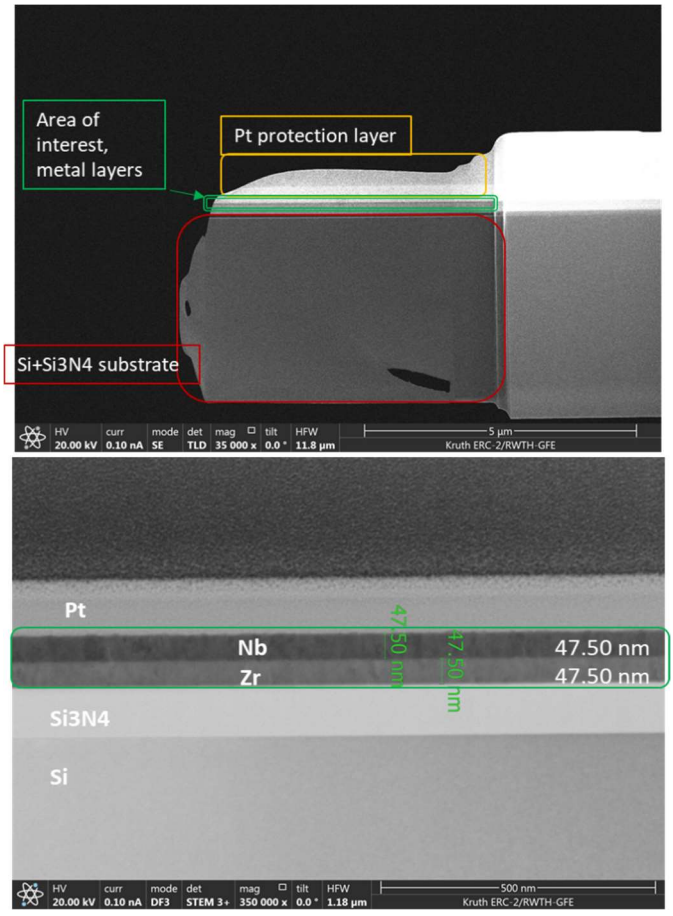

Figure 6.7: *Lamella cut of Nb/Zr sample, SEM images. Top: Three color areas identified, in red the substrate, in green the area of interest with Zr and Nb metal layer and in yellow the Pt protection layer. Bottom: Layers thicknesses were measure with SEM tools, both Zr and Nb have about 47.50 nm.*

TEM BF detector images were used to study the crystal structure of the different layers and their interfaces. As we can observe in *figure 6.8* the Nb/Zr bilayer is "sandwiched" between the platinum protection layer used for the preparation of the TEM specimen and the Si_3N_4 membrane + Si substrate. Five different positions were chosen to obtain five selected area diffraction patterns

(SADP), in order to study the various adjacent components and their respective interfaces. The positions are numbered in the image from 1-5.

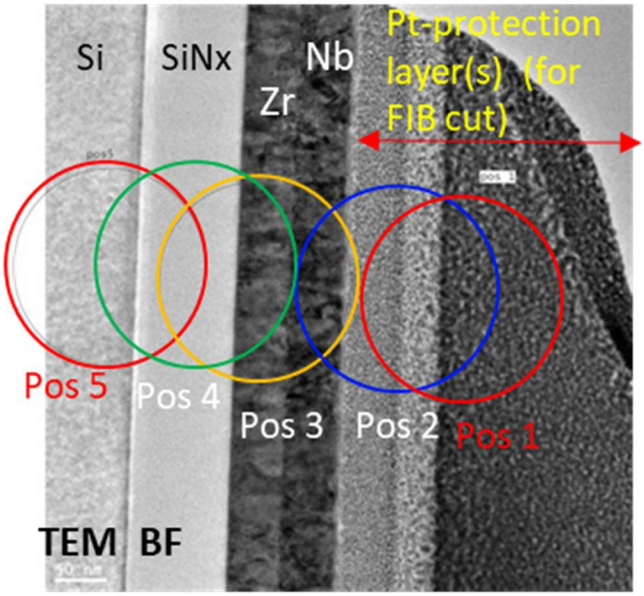

Figure 6.8: *TEM BF image of the cut lamella. Different positions on the sample image were marked in colored circles for analysis purposes. There are five positions, indicating the positions of the selected area aperture. Positions 2, 3, and 4, marked in blue, yellow, and green respectively cover the area of interest. The scale bar in the image is 50 nm.*

In table 6.3 we present the crystal structure of the elements founded in each one of the five positions marked in *figure 6.8*. The g values of the possible structures founded in each position are color code. The respective colors are black for ZrO, green for Zr (fcc –brighter green or hexagonal P63/mmc- darker green), blue for Nb, red for Pt, and orange for Si. Grey g values are from unknown structures due to some spots that are superposed making difficult the identification.
Since our area of interest is covered by positions 2, 3, and 4, we will review in detail the analysis done in those two positions while the analysis done to positions 1 and 5 will be summarized.
Position 1 only contains the material of the Pt protection layer, as indicated in the BF image.

In *figures 6.9, 6.10,* and *6.11* the diffraction patterns of the selected areas belonging to position 2, position 3, and position 4 respectively are shown. The measure of the rings DPs is done with the rotation average shown to the upper right in each figure, which shows the intensities and the position of each ring founded in the DP.

The DP acquired for position 2, *figure 6.9*, contains different materials: Pt protection layer and the upper (Nb) layer (as indicated in the previous BF image).

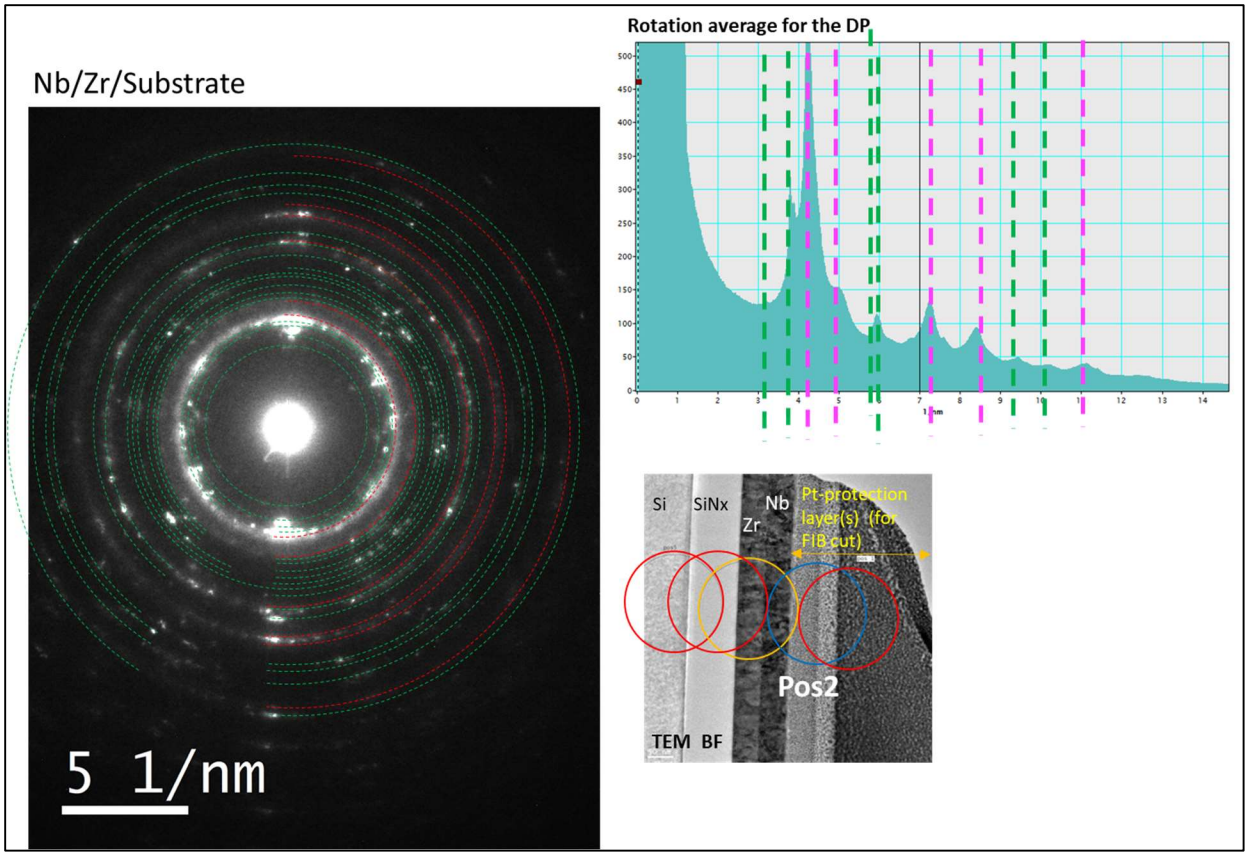

Figure 6.9: *Diffraction pattern of position 2. The blue circle in the image above, which represents the position of the selected area aperture used for the acquisition of DP, (i.e., Pt and Nb layer-mainly). The rotation average indicates the positions and intensities of the rings to obtain the g values.*

Due to inaccuracy of the positioning of the SA aperture it is not excluded that other material layers are contained in the selected area; g values corresponding to ZrO were found during the analysis, which means that position 2 is covering also the upper part of the Zr layer. The possible structures to which the spots can be ordered are indicated in the table with their respective colors, defined above.

The DP acquired for Position 3 (*figure 6.10)* contains mostly the bilayer formation corresponding to the filter. In position 3, we could identify two different crystal structures for Zr (hcp and fcc), and different crystal orientations as is typical for polycrystalline structures. The crystal structure found for Nb was always bcc, but also with varying orientations as is shown in *table 6.3.* Some of the g values corresponding also to ZrO were found.

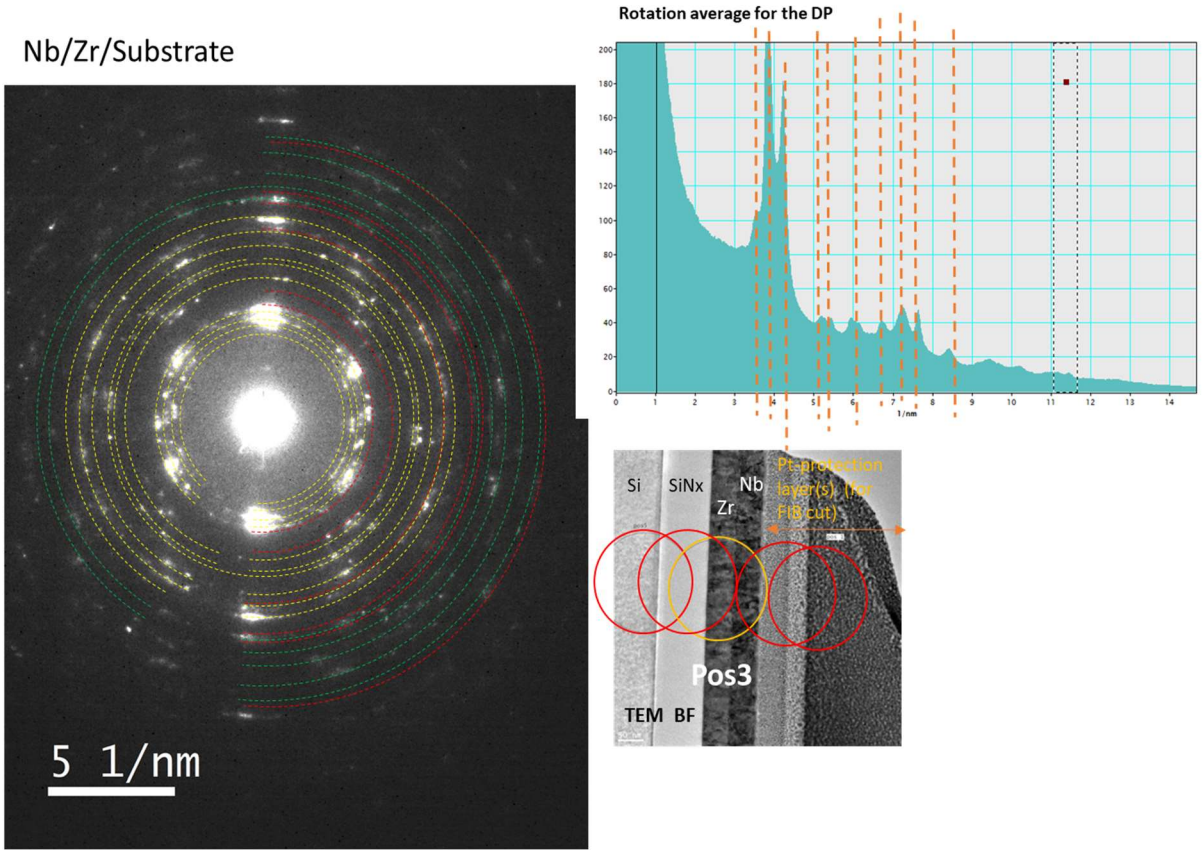

Figure 6.10: *The yellow circle in the image above represents the position of the selected area aperture used for the acquisition of DP in position 3 (both layers and the SiNx part).*

In position 4, *figure 6.11*, DP of Si (Fd-3M) in [110] zone axis is clearly recognized. The additional spots should correspond to the bottom layer (Zr + Nb), crystals with different orientations where found, see *table 6.3*. Unfortunately, the amount of the bottom layer material is restricted, and only a few spots are present. The possible structures to which the spots can be ordered are indicated in the table with the respective colors. The corresponding values of g, given in the table, in the last column, indicated in orange, are used as a reference for analysis of DP in position 4. Next to the g values measured from the experimental pattern, also values for model Si (with cubic unit cell parameter a = 0,54309 nm) are given in brackets.

DP acquired for the position 5 contains the material of Si substrate and Si-nitride layer (as indicated in BF image, *figure 6.8*) It could be identified as DP of Si (Fd-3M) in [110] zone axis.

In *figure 6.12,* BF TEM image shows closely the bilayer structure Nb/Zr and the interface between them. In Nb side as well in Zr side, different planes due to the different crystal orientation present in the layers can be appreciated.

Table 6.3: *The g values founded in each position in the diffraction patterns for Nb/Zr. Color code: black for ZrO, green for Zr (fcc –brighter green or hexagonal P63/mmc- darker green), blue for Nb, red for Pt, and orange for Si. Grey g values are from unknown structures.*

g values **Pos 1**	*g* values **Pos 2**	*g* values **Pos 3**	*g* values **Pos 4**	*g* values **Pos5_ Measured/model**
	3.2 ZrO (111)		**3.2**	**3.2 / (3,19)**
	3.7	**3.5 Zr P63/mmc (100)**	**3.7 +Si**	**3.7 (3.68)**
	3.8	**3.8 Zr fcc (111) Zr P63/mmc (002)**	**3.9**	
	3.9 + ZrO (200)		**4.1 Nb (110)**	
4.4	**4.2+Pt**	**4.2 Zr fcc (200)**		
5.1	**5.2+Pt**	**5.2 Zr P63/mmc (102)**	**5.2+Si**	**5,2/ (5,21)**
	5.4 ZrO (220)	**5.4**	**5.6**	
	5,7	**5.9**		
	6.0	**6.0**	**6.1Nb (200) +Si**	**6.1 / (6.11)**
	6.2	**6,15 Zr fcc (220) Zr P63/mmc (110)**		
	6.4 ZrO (311)		**6.3**	**6.4 / (6.38)**
	6.8	**6.7 Zr P63/mmc (103)**	**6.7**	
7.1	**7.3+ Pt+Zr**	**7.2 +Zr fcc (311)**	**7.4 Nb (211) +Si**	**7.4 / (7,37)**
	7.7	**7.6 Zr fcc (222)**	**7.8**	
			8.0	**8.0 / (8.03)**
8.3	**8.4 ZrO (331) +Pt**	**8.4**	**8.6 Nb (220)**	
			9.1	**9.1 / (9.235)**
	9.4+ ZrO (422)	**9.4**	**9.6 Nb (310)**	**9.6 / (9.57)**
	9.7			
	10.2	**10.2**	**10.4 Nb (222)**	**10.4/ (10.42)**
11.0	**11.1**	**11.0**	**11.1**	**11.1/ (11.05)**

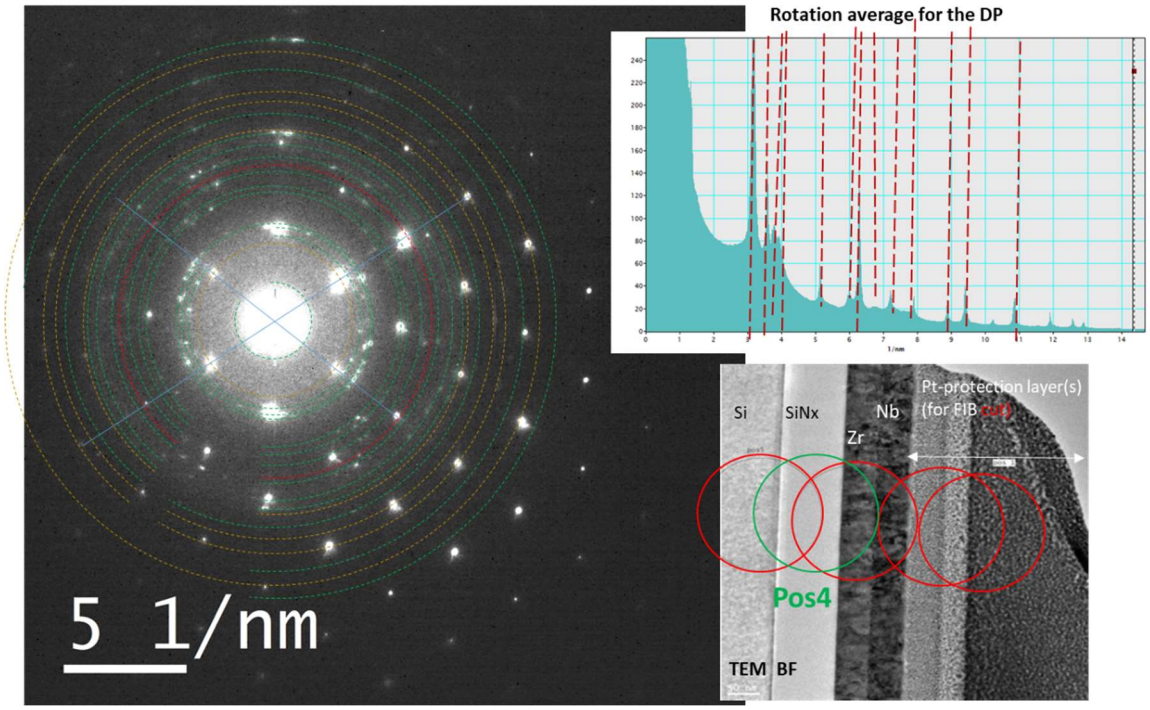

Figure 6.11: *Diffraction pattern of position 4. The green circle in the image above represents the position of the selected area aperture used for the acquisition of DP. (Si + Si_3N_4 + Zr + bottom part of Nb layer).*

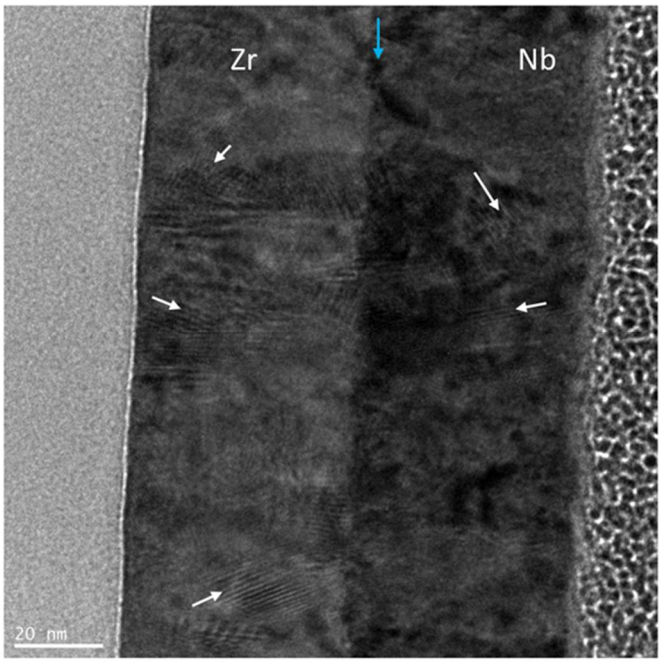

Figure 6.12: *BF image of the bilayer Nb/Zr. In the picture the sharp interface between the layers can be observed. The white arrows show points where planes with different crystal orientations are visible.*

In summary for this sample, Interfaces between layers looks very sharp, intermixing is not appreciated in the BF images, it is recommendable an EDX analysis to evaluate interdiffusion. DPs were very difficult to analyze due to the small amount of the materials in the area of interest included in the SA aperture due to the shallow thickness of the layers (TEM specimen too thin). Since the materials of these layers were Nano-polycrystalline, each time only a few grains (with variable crystallographic orientations, (see *figure 6.12*) of the layers of interest could contribute to the DP, which resulted in very few spots.

Due to very similar values for the different g for all material considered, some structures could not be identified (the same g can be attributed frequently to several materials). The only clear contributions are in pos. 1 and 2 and correspond to Nano-crystalline Pt and in positions 4 and 5 corresponding to single-crystalline Si. The best method to identify the structure is the analysis with the aid of HRSTEM, but it was not possible to be performed for this sample due to limited time with the instrument.

6.4 Zr/Nb (sample 3).

A Si_3N_4 membrane window of 10 nm thickness, used especially for TEM imaging, was used to deposit the sample to be studied. The nominal value of thicknesses of the bilayer structure Zr/Nb was 50 nm/ 50 nm. However, but due to fluctuation of the voltage during the evaporation of Zr, the thickness of the Zr layer is higher. Furthermore, because of the oxidation of Zr, the Zr layer is expanded, so at the time of the measurement Zr thickness was about 70 nm as can be observed in *figure 6.12*, which corresponds to the SEM image of the cut lamella.

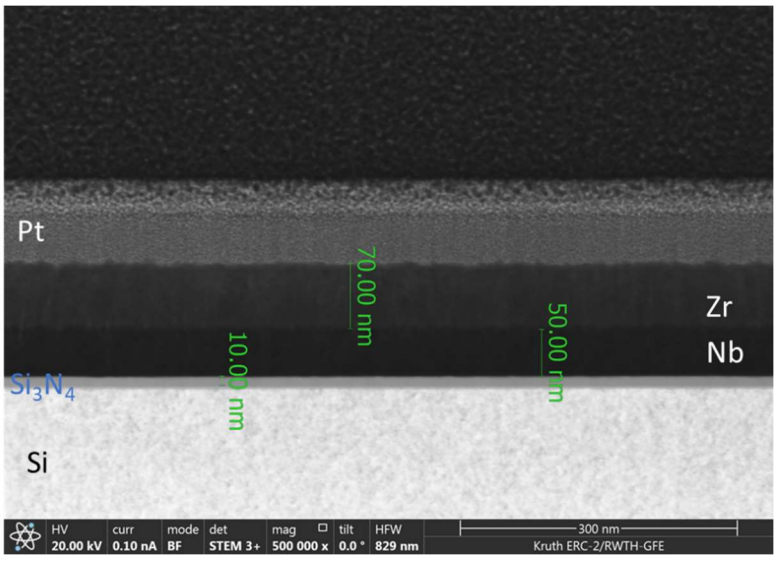

Figure 6.12: *SEM Image of the Lamella cut of Zr/Nb. The thicknesses of Zr and Nb are shown, and also the thickness for the* Si_3N_4 membrane.

For the study of this sample, HRSTEM images were used, which convey in more reliable results, determining with high accuracy the crystal structure of the materials involved.

First, an EDX analysis was performed, and it is presented in *figure 6.13*. EDX 1, the top right image, only Zr and Nb are highlighted. The interface between these layers is very sharp and we can notice that no inter-diffusion is present between the two layers. EDX 2 shows the full composition of the specimen. Each element is represented with a different color: yellow for Si, orange for Si_3N_4 membrane, marked as N, for the nitrogen content. Follow by Niobium, which is red, Zirconium green, the oxygen content is represented by light blue, the Platinum protection layer is dark blue, and Carbon is purple.

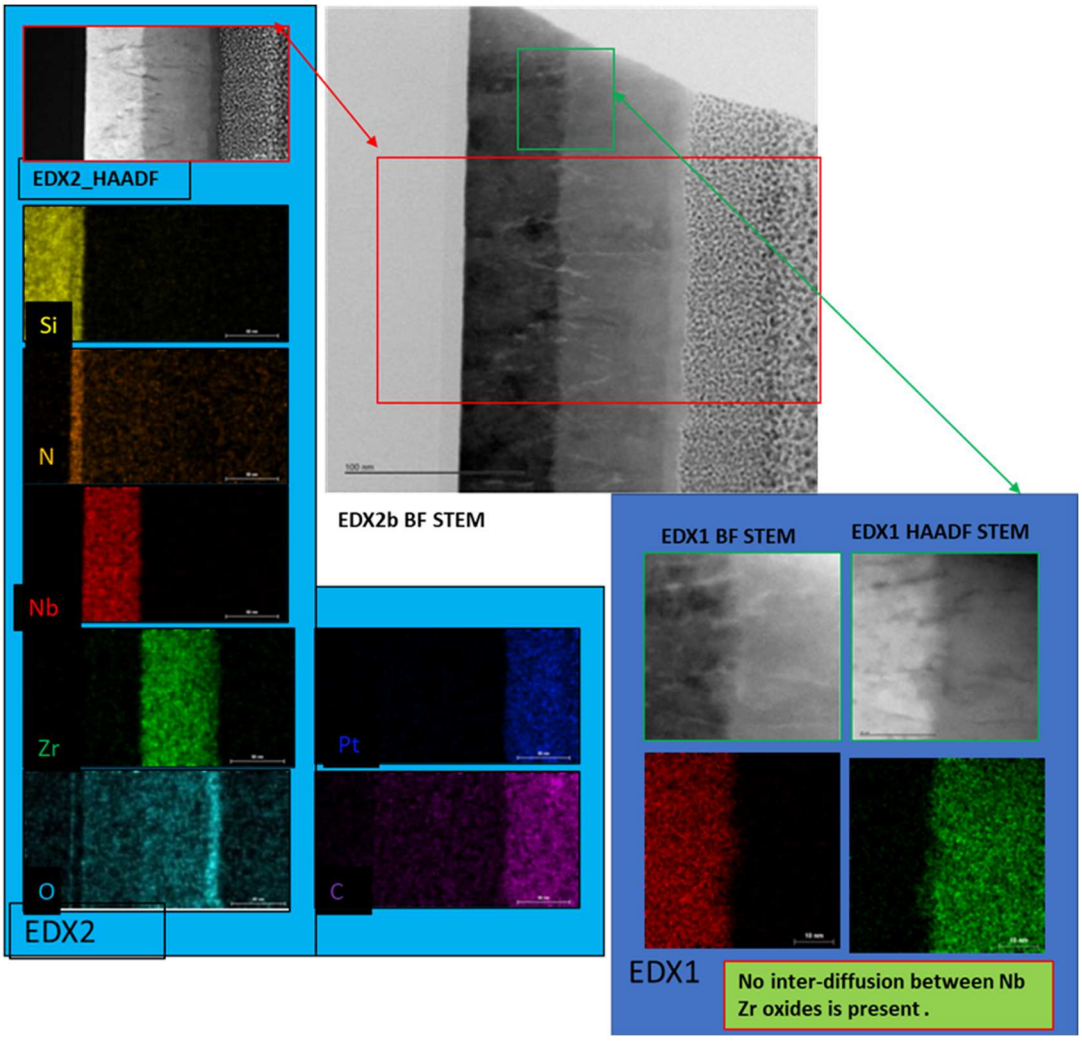

Figure 6.13: *EDX analysis of the sample. It was not found interdiffusion between Nb and Zr layer. Each layer of the sample is color code in order to appreciate the interface between layers. EDX1 (bottom right), shows only the bilayer section with Zr and Nb. EDX2 shows all the layers that compose the sample. EDX2 shows the presence of ZrO (light blue) at the top of the sample, also son carbon contamination (purple).*

Since Zr is in the top layer and it gets oxidized very easily when it is exposed to the air, it was expected to be oxidized. In the results we can observe that the outer layer of Zr (10 nm top layer) is oxidized; the very high blue area shows that. Carbon contamination is also present in the sample.

In *figure 6.14*, the TEM BF was processed, four areas were selected to study more closely the composition of these areas to acquire the crystal structure of the elements involved using the FFT. The four regions are shown in four different colors. From left to right: First area, color red, it has been processed to study Nb. The second area, the color purple, it is used to study Nb, Zr, and the interface between them. The third area, color light blue, it is intended for studying just Zr. Finally, the fourth area, color green, has been processed to study the Zr layer but including the oxidized part of the film; it means the ZrO crystal structure was also obtained.

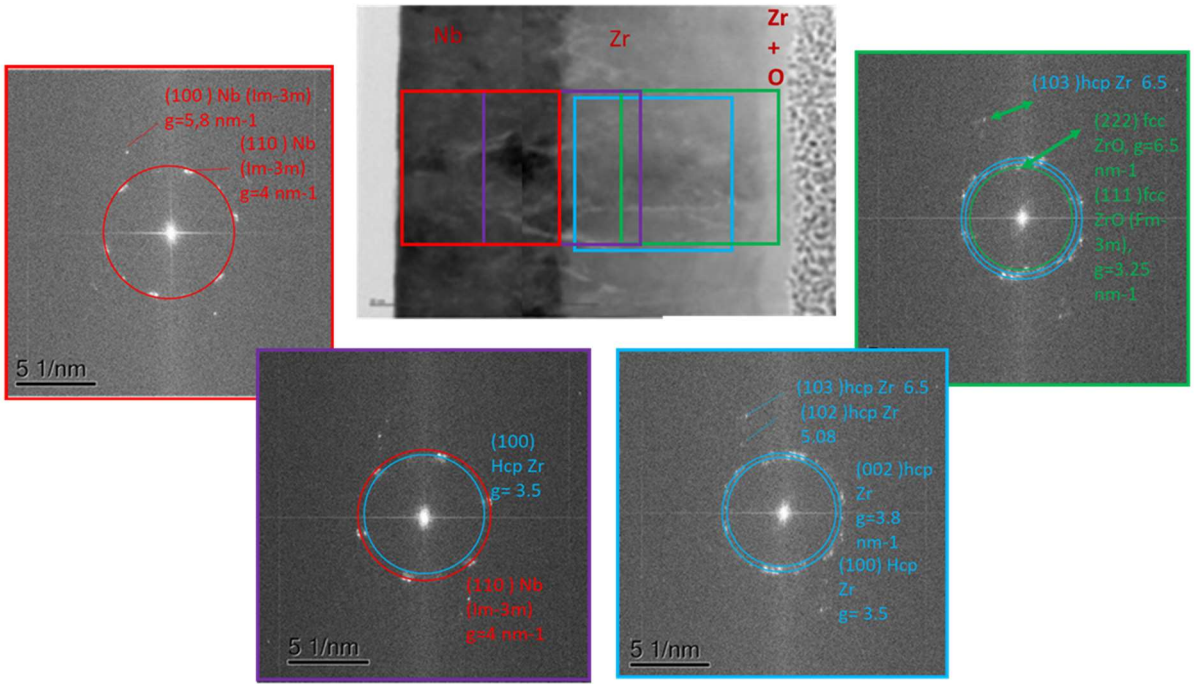

***Figure 6.14**: FFT diffraction pattern of the four different areas chosen to study the crystal structure of the materials of each layer, obtained from high-resolution Bf STEM image (center picture). Four aperture selected areas were chosen to study the sample (colored squares). The crystal structures found for Nb, Zr, and ZrO are marked in red, blue, and green respectively.*

Again, ImageJ tools from FIJI software were used for the acquisition of the g values and lattice parameter from the ring formed on the diffraction pattern. Those values were compared with different models to obtain the crystal structure of the materials. The resume of all results is presented in *table 6.4*. HRSTEM images were also used to process three areas, studying carefully and separately Zr, ZrO, and Nb.

In figure 6.15 top left: A HAADF STEM image of the bilayer and the well-defined interface is shown. Some lines that go from one layer to the other can be appreciated, possible marks of defects and dislocations present on the bilayer structure.

Figure 6.15 top right: BF STEM images are presented, to have a better visualization of the unit cells due to the different contrast depending on the type of image. For Zr, Hexagonal, honeycomb shape it well observed, with agrees accurately with XRD results and the FFT images results. Fourier Transform (FT) images, were indexed with the unit cells of d Zr hcp (i.e., high-temperature hexagonal structure of Zr with space group P63/mmc). The model used for the lattice parameters are: a = 0,323 nm c = 0,515 nm. For this model g (002) = 3.88 nm^{-1} and g (100) = 3.57 nm^{-1}. While from experimental images we got g (002) = 3.8 nm^{-1} and g (100) = 3.5 nm^{-1} so the unit cell parameters will be respectively bigger than that of the model.

The top part of the Zr layer was studied, this part of the layer is oxidized, it corresponds to an about 10 nm ZrO layer. Remembering that in BF image the contrast is higher in heavy elements, so the oxygen atoms can be appreciated since Oxygen is lighter than Zr. The Fourier Transform (FT) images were indexed with the unit cell of cubic ZrO (space group Fm-3m), which is well defined in the image (*figure 6.15 bottom right*). The lattice parameter of the used model was a = 0.513 nm. The model predicts g (200) = 3.896 nm^{-1} and g (220) = 5.51 nm^{-1}, while from experimental image FT we got: g (200) = 3.7 nm^{-1} and g (220) = 5.2 nm^{-1}. So, also, in this case, the unit cell parameter will be respectively bigger than the one for the model used.

In *figure 6.15 bottom left:* We focus on the Nb layer. Nb is not oxidized. Cubic crystals with different orientation planes can be easily identified. Fourier Transform (FT) images were indexed with the unit cell, of cubic cells, of Nb (Lm-3m) with a=0.33 nm. For this model g (200) = 6.06 nm^{-1} and g (220) = 4.28 nm^{-1}, while from experimental image FT we got: g (200) = 5.8 nm^{-1} and g (220) = 4.15 nm^{-1},). So, for Nb also, the unit cell parameter will be respectively bigger than the cells of the model.

Each time the experimental lattice parameters (a and c) appear to be 5% bigger than those of the model. Considering the calibration overestimation of 2% evaluated for Si, 2-3% difference in the lattice parameter can be assumed.

Table 6.4: ***Crystal structure of the elements that composed the Zr/Nb sample.***

Elements	**Crystal structure**	**Orientations**	**experimental *g* values (nm^{-1})**	**Model *g* values (nm^{-1})**
Zr	Hcp ($P6_3/mmc$)	(002)	3.80	3.88
		(100)	3.50	3.57
ZrO_x	Fcc (Fm-3m)	(200)	3.70	3.90
		(220)	5.20	5.51
Nb	Bcc (Im-3m)	(200)	5.80	6.06
		(220)	4.15	4.28

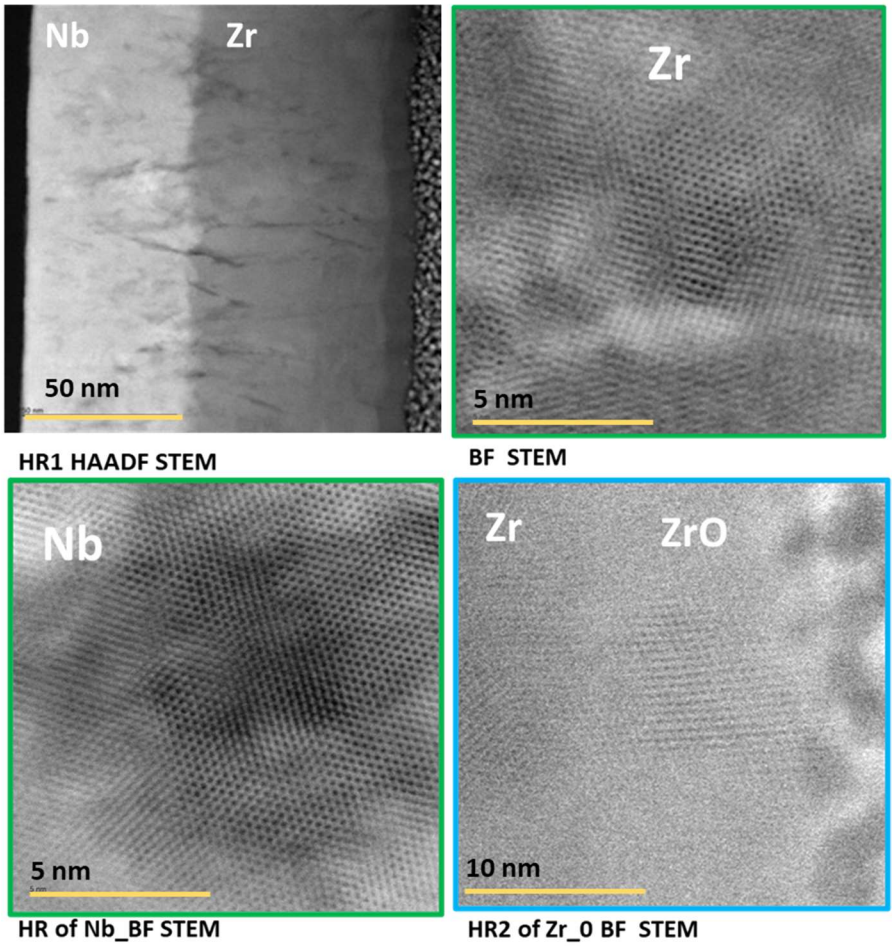

Figure 6.15: *HAADF STEM and BF STEM images of the crystal structure of Zr. A close view of the shape of the crystal structure is observed and an estimation of the size of the unit cells.*

6.5 Nb/Zr/Nb (sample 4).

Since Zr oxidizes faster than Nb, a three-layer structure was fabricated assuming Nb would protect Zr from oxidation and it will make the structure mechanically tougher. In the hypothesis the transmittance performance of the three-layers should be very similar to the free-self-standing Nb/Zr filter, since the total thickness of the sample also will be around 100 nm after etching. For the three-layer sample (sample 4), we will focus just on EDX analysis and Nb crystal structure since there was no novelty in the Zr layer in comparison with the last samples and there was limited time using the instrument. For the fabrication of this sample, a standard 100 nm membrane window was used as a substrate for the e-beam evaporation of the materials.

The SEM cut lamella cross-sectional image is shown in *figure 6.16*. Optical measurements of the thicknesses of the layers were performed with SEM tools.

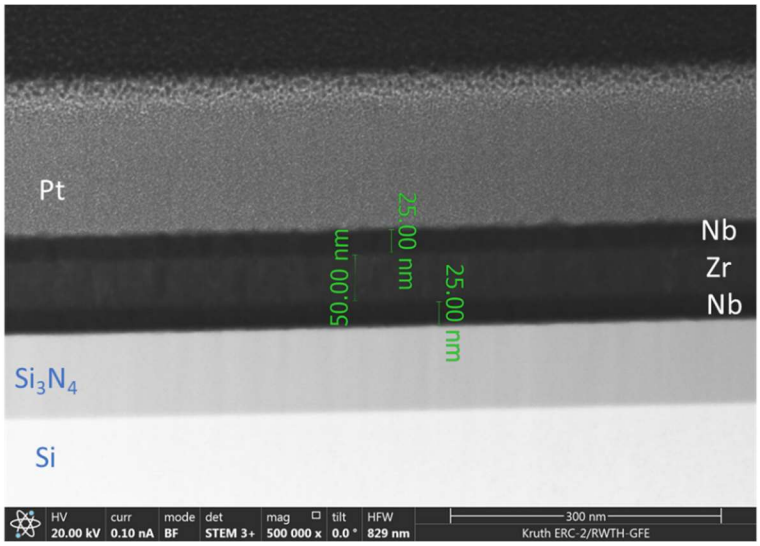

Figure 6.16: *SEM Image of the cross-section Nb/Zr/Nb. The thickness of each layer is shown.*

In figure 6.17 BF images are shown, the interfaces don't look so sharp, some roughness can be appreciated. Some planes with different crystal orientations can also be identified marked with white arrows.

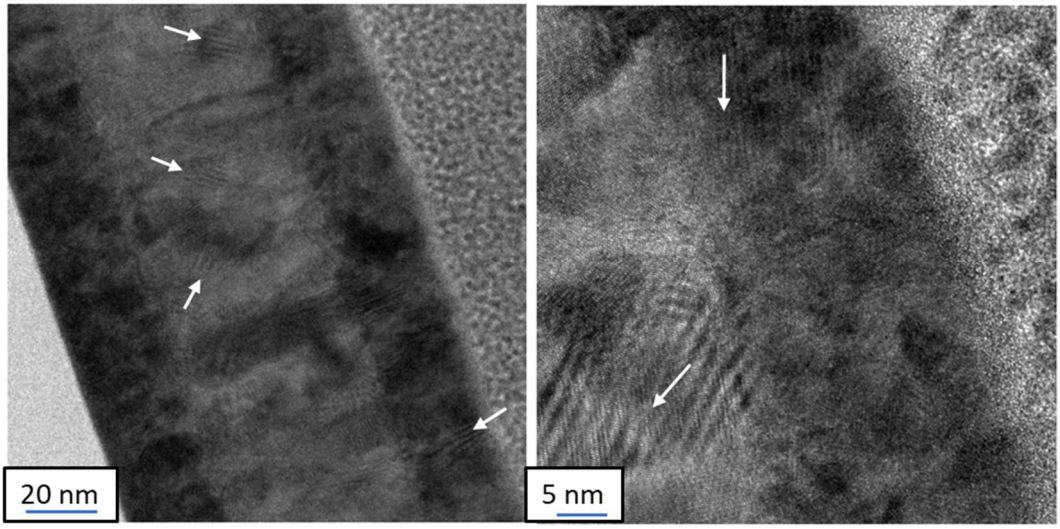

Figure 6.17: *BF TEM images for closer views of the three-layers structure. The white arrows show planes where different crystal orientations can be appreciated.*

In the HRSTEM images in *figure 6.18*, the crystal structure of Nb is studied. In the case of HAADF mode, the heavier elements appear lighter, so Nb in the sides appears with less contrast than Zr. Previously, the calibration of the images was done using the HRSTEM images of Si. The unit cell from the model of cubic Si used corresponds to the lattice parameter a = 0.543 nm, while the experimental measurements give us a value of a = 0.556 nm. That means that the unit cell parameters measured from STEM will be overestimated by 2%.

Since Nb get oxidize slower than Zr, not an expansion of the upper Nb layer is present. The unit cell of Nb was measured in the outer layer, corresponding to Nb bcc with different crystal orientations: Nb (200) with g = 5.8 nm^{-1}, with a unit cell of about 0,338 nm, (after consideration of 2% overestimation calculated via calibration from HRSTEM images of Si) and Nb (110) with g = 4.1 nm^{-1}.

Finally, we cannot explain the origin of the additional Nb crystal structure with g = 3.6 nm^{-1}. This g value does not fit to Nb or NbO (Pm3m) but could be some other state of oxidation of Nb like Nb_2O_5 [78], or maybe the formation of a superstructure.

Following the procedure of indexation of the crystal structure, EDX analysis was performed; the results are shown in *figure 6.18*. As for the last sample, each layer is color-coded, corresponding to yellow for Si, orange for N, which corresponds to the Nitrogen contents of the membrane. Continuing with red is for Nb, green for Zr, dark blue for Pt protection layer, and very light blue for the oxygen content.

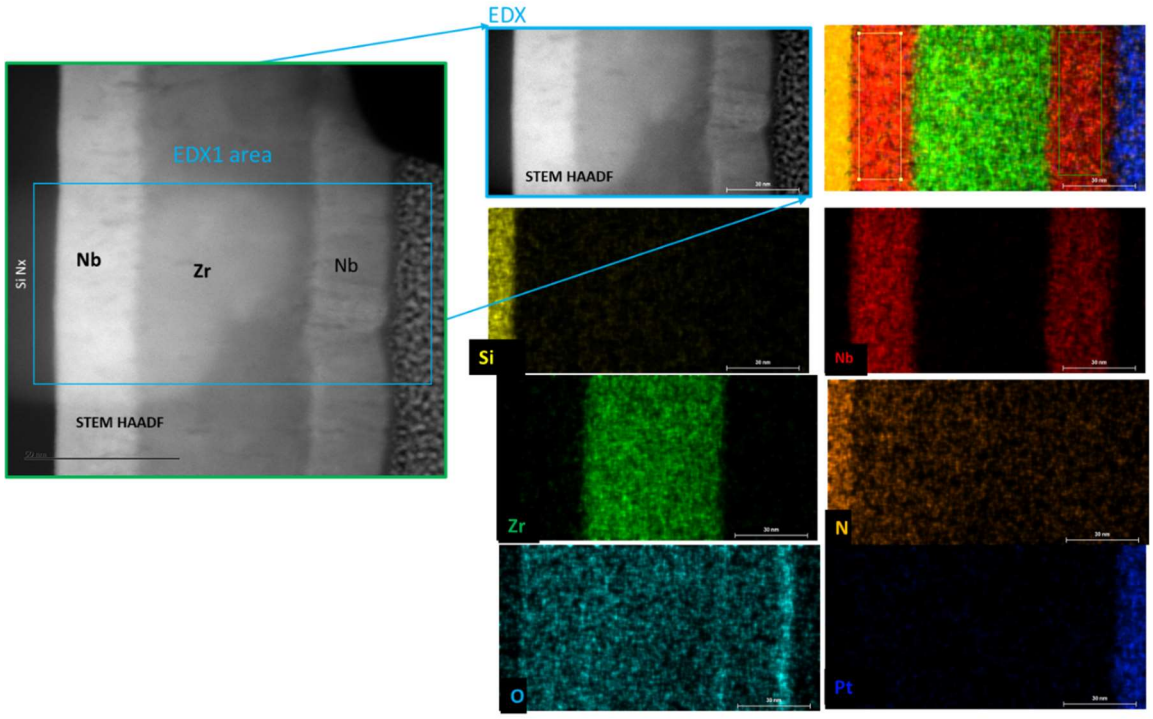

Figure 6.18: *EDX analysis of the difference interfaces interactions, each element is color code, no interdiffusion was found.*

No interdiffusion was observed between the Zr and Nb layers, neither at a higher resolution. Nevertheless, as we can see in the images, the internal boundary is not perfectly flat. The roughness of the interphase is in the range of 1-2 nm.

The top layer of Nb present oxidation, the thin layer is of about 4-5 nm. Not expansion of the Nb oxidized layer can be determined without previous thicknesses measurements.

6.6 Conclusions

- The filters are composed of polycrystalline layers. Different crystals structures of Zr were found mostly in sample 1, but due to the less accuracy of those measurements in compare with the HRSTEM measurements for sample 3 and the XRD results, we conclude the Zr hcp structure is the most reliable structure to be found in this type of thin films.
- Nb layers were composed for different crystals orientations but always bcc Nb, agreeing very well with XRD results presented in section 6.1.
- The structure for ZrO founded corresponds to fcc ZrO. Zr expands when it gets oxidized, but we cannot know precisely the amount of expansion without previous measurements of sample thickness. The expansion of this layer can lead to an increase of stress on the films and it could be the reason why Zr/Nb filters are more fragile than Nb/Zr ones.
- Oxidation was always found in the top layer of the filters.
- Carbon contamination, typical in this type of filter, was found in sample 3.
- There was not inter-diffusion between the interfaces of Zr/Nb, Nb/Zr, but the boundaries between materials were not completely flat. The roughness of the interfaces in sample 4 was estimated to be between 1-2 nm.

Chapter 7.

Study of EUV radiation damage on free self-standing Nb, Zr, Nb/Zr, and Zr/Nb thin-film filters.

7.1. Introduction.

Optical devices in high brilliance sources, such as thin-film absorption filters, mirrors, and others, which operate under vacuum of about 10^{-6} Pa or lower, are exposed to radiation in the presence of residual contaminants (more often water vapor and hydrocarbons) and so their surfaces are susceptible to oxidation, carbon deposition, and other chemical reactions.

The main chamber is filled with optics, sensors, electric wiring, and numerous other components [79]; All these components not only produce outgassing but also make baking of the vacuum system impossible, which can also lead to the contamination of the filters. Moreover, the contribution of hydrocarbons produced during the exposure process itself cannot be ignored, most filters are very susceptible to carbon contamination, which results in reduced transmittance.

The photochemistry of the relevant processes at the surface of the optical elements is found to be intensely dependent on the type and pressure of background gas constituents and the incident flux of the EUV photons. Under the illumination with EUV radiation, photoelectrons of less than 10 eV energy are typically created [80]. The cracking of the adsorbed molecules at the optical surface by those photoelectrons or due to EUV photodissociation results directly in contamination of the surface of the optical devices with molecules and radicals [81, 82, 83].

Water and oxygen act as oxidizers, most of the materials available for filters in EUV oxidize quickly, which reduces their performance and results in rapid aging. This effect can be prevented or mitigated by using an oxidation-resistant protective capping layer.

Hydrocarbons lead to carbon growth. Three steps lead to carbon growth: adsorption, diffusion, and photon or secondary electron-induced dissociation [80,79]. Unfortunately, most capping layers do not prevent the build-up of carbon contamination, leaving this as the primary surface contamination process [80]. The high absorption of EUV radiation by carbon makes the contamination layer a critical issue.

Thin-film filters for extreme ultraviolet are used to remove multiple-order radiation. They are also used as gas barriers, allowing the introduction of contaminant gas that could damage the filters and of course, cause of contamination [10, 14, 18]. The contamination of the films reduces the performance of the multilayer filters. So proper study of the contamination due to environment and radiation exposure is necessary to determine appropriate protective coating solutions for these transmittance filters.

7.2. Experiment Description.

The free self-standing filters designed and fabricated in this project are intended to be used in EUV and soft x-ray FEL sources. In these types of sources, the filters will have to face high peak power radiation, high repetition rate, long-term operation and short pulses, which could deliver enough energy to the filter's structures to cause re-crystallization and an increase in the number of defects in thin films inducing damage on this kind of optical devices even if the irradiance doesn't exceed the single-shot damage threshold [84, 85].

The durability of free self-standing thin-film filters at normal incidence as well as the contamination process due to the exposure to high-density EUV radiation has been experimentally studied. Due to the difficulty of obtaining FELs time to study the behavior of the filters under FEL conditions, an alternative experiment has been developed using a high-density radiation set-up to expose the samples to certain doses of EUV radiation; with the possibility to determine the critical dose where the samples show any change on their surface due to the exposure.

For this experiment, one set of 6 samples formed by 4 different types of free self-standing filters was used: Nb, Zr, Nb/Zr, and Zr/Nb, see *figure 7.1*. The samples were fabricated in the HNF center at Forschungszentrum Juelich, following the fabrication procedure described in chapter 3. The filters have a 3 mm x 3 mm window area. Doses variations are determined by the time of exposure. 2 min, 4 min, and 6 min along the horizontal axis.

As the deposition method, e-beam deposition technique was used; deposition conditions are given in sub-section 3.2.4 and etching recipe in section 3.4. As a side note, it is worth mentioning that the samples prepared by e-beam technique, before etching presented a very flat and smooth surface but after etching procedure, Zr and Zr/Nb samples became wrinkled as the Zr and Zr/Nb filters prepared by sputtering for chapter 5 experiment.

Four samples were exposed to high-density EUV and 2 samples were kept as a control. Having control samples is important because it helps to differentiate between contamination or damage on the surface due to environmental conditions and handling during characterization from those due to radiation exposure. Samples are described in *table 7.1,* with the particular objective for each sample.

After the fabrication, optical microscope's images and XPS measurements were performed on the surface of the samples to be able to identify any macro-change after the radiation exposure. A Phi5000 VersaProbe II XPS was used, the instrument was described in chapter 4. XPS was performed in 3 points of each sample.

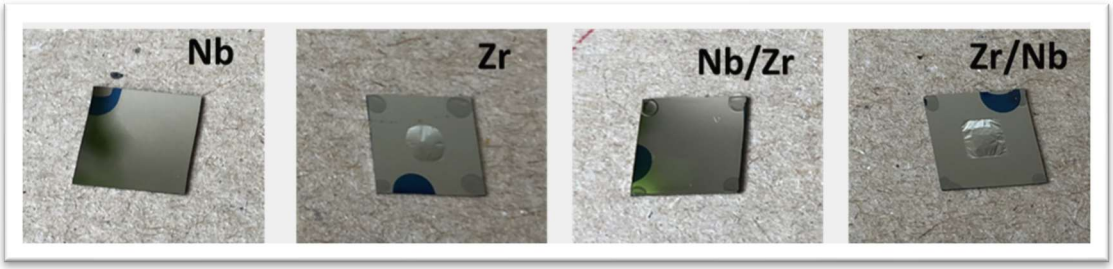

Figure 7.1: *Free self-standing filters to be exposed to high-density EUV radiation.*

Table 7.1: *Description of the samples that will be used for the experiment and each particular objective during the different parts of the study.*

	Sample	**Nominal thickness (nm) +/- 5 nm error each layer**	**Objective**
1	Nb_1	100	To be exposed at ILT + before and after characterization
2	Zr_1	100	To be exposed at ILT + before and after characterization
3	Nb/Zr	50/50	To be exposed at ILT + before and after characterization
4	Zr/Nb	50/50	To be exposed at ILT + before and after characterization
5	Nb_2	100 nm	Sample control
6	Zr_2	100 nm	Sample control

The transmittance of the samples was characterized before exposure tests in BEAR beamline at ELETTRA synchrotron. Due to the limited time available for using the beamline the samples could not be characterized in the full spectral range from 4 nm to 20 nm. In order to be able to monitor any changes on transmittance after high-density EUV radiation exposure, only four wavelengths were chosen to scan the horizontal axis using the Y manipulator (which allows the horizontal movement along the sample) of the instrument: (6, 7.02, 13.5, 17) nm. The radiation exposure was intended to be performed along the horizontal axis. All filters have a small blue mark in one corner, which is used to recognize the horizontal axis orientation and thus ensure the same position of the sample during the radiation exposure and characterization procedures.

An EUV pulsed xenon plasma discharge source combined with a high-NA optics (two-shell ruthenium-coated Wolter collector) and a molybdenum/ silicon multilayer mirror optimized for 13.5 nm, to achieve high peak irradiance at sample was used to apply three doses on each sample,

for a total of three radiation exposure spots. The focus point position was determined with the help of a scintillator, which was also used to estimate the size of the beam spot; The spot size is about 0.05 mm^2.The setup is located at the Fraunhofer Institute for Laser Technology and the Chair for Technology of Optical Systems at the RWTH Aachen University. *Figure 7.2* shows the schematic drawing of the samples with the positions where the different exposures were performed. Samples were kept in vacuum during EUV exposures; The vacuum level was around 10^{-5} Pa.

During the experiment the beam was not characterized due to time limitations; the setup was built and characterized around two years before the experiment and a re-characterization of the beam was performed by the lab team some time after the experiment. The values of peak intensity and fluence obtained during the re-characterization of setup are used in this thesis to estimate the doses applied to the samples. The peak intensity in the spot was approximately 0.19 W/cm^2; the fluence was kept constant at a level below the single-shot damage threshold while the variation of the doses applied on each spot depends on the time of exposure and the pulse frequency.

The fluence per pulse F is determined by

$$F = \frac{\epsilon_p}{A} = \frac{1.9\ \mu J}{0.0005\ cm^2} = 3.8\ \mathrm{mJ}/cm^2 \qquad 7.1$$

Where ϵ_p is the average energy per pulse, value taken from the information about the characterization of the source and optical setup described in the next section, and A is the effective area.

The theoretical dose applied in each spot is given by:

$$Dose_{total} = F \times ʃ \times \mathrm{t} \qquad 7.2$$

Where ʃ is the pulse frequency and t is the total time of exposure in seconds.

To characterize the beam on the spot, a Zr filter placed before the photodiode was used to eliminate out-of-band radiation, in this way, the peak intensity measured by the photodiode is lower than the peak intensity radiation applied to the samples, meaning that the experimental total doses applied to the three spots on each sample are estimated to be larger than the theoretical values presented in *table 7.2*.

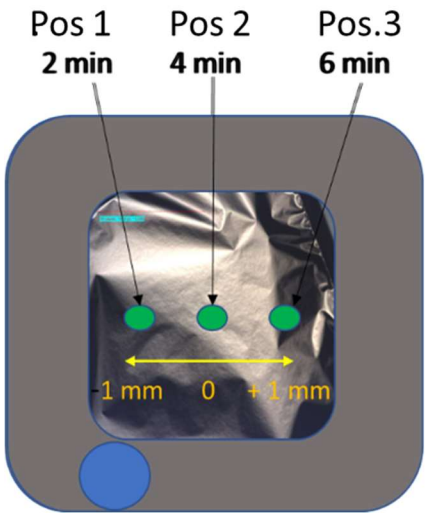

Figure 7.2: *Schematic picture of the exposure spots. The first spot was at the center of the filter's window. The other two spots were separated by 1 mm from the center, left and right. All samples have a reference blue spot to ensure the position orientation of the samples.*

Table 7.2: *Time of exposure and the calculated total dose applied in each selected position.*

Position	Time of exposure (s)	Total theoretical dose on the spot J/cm^2
1	120	22.8
2	240	45.6
3	360	68.4

After the EUV exposures were performed, filters were re-characterized by microscope optical observation and XPS measurements around the same spots of the radiation exposure. Both XPS analysis before and after the experiment were carried out at ZEA3 institute at the Forschungzentrum Juelich.

Unfortunately, sample 4 (Zr/Nb) was broken while it was mounted for XPS measurements. Transmittance measurements after exposures were not possible by the time of writing this thesis.

7.3. High-density radiation setup.

As a light source, AIXUV pulsed xenon plasma discharge source is used, *figure 7.3*. This type of source produces a plasma pinch with a sub-millimeter diameter and strong emission lines in the XUV. The light output for this type of source has been measured in previous projects from ILT and RWTH Aachen, to be 0.401 mJ/sr per pulse within a 2 % bandwidth around 13.5 nm [86]. This value includes self-absorption in the xenon that leaves the source together with the light.

To filter a smaller band around the desired EUV wavelength, a molybdenum/silicon multilayer mirror optimized for 13.5 nm is used. The source is connected to vacuum chamber. Via this chamber, pressure measurement devices, a turbomolecular pump, and gas inlets for venting are connected to the setup. The vibration frequency of the turbomolecular pump is about 500 Hz, filters to be tested must be tougher enough to resist the vibration. The complete information about the setup can be found in the master thesis of Oskar Hofmann [87]; Part of his project at RWTH Aachen was the full characterization of this source and optical design of the setup (first characterization). The characteristics of the source and the beam re-characterization are presented in *table 7.3.*

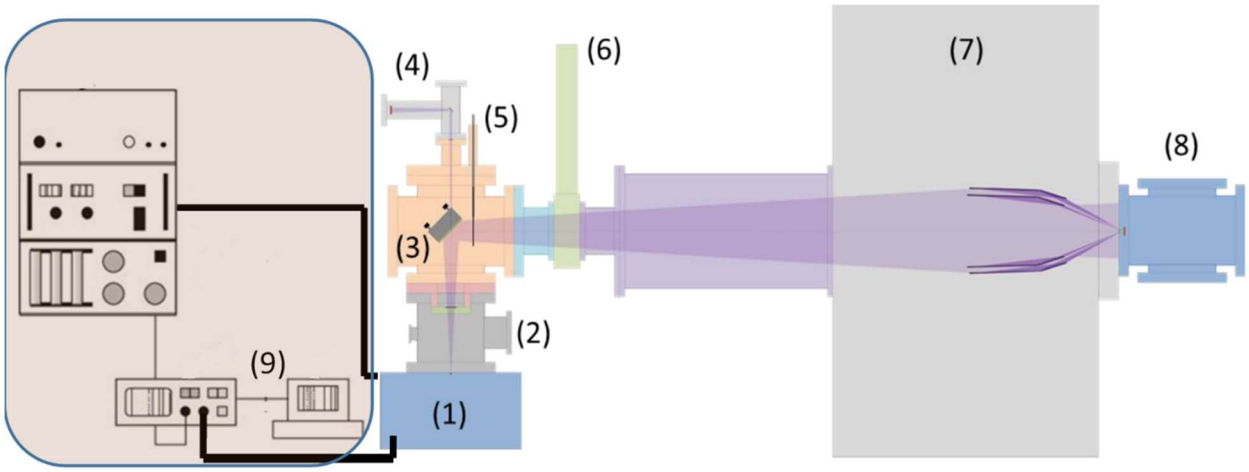

Figure 7.3: *Scheme of the experimental setup [87] with the source (1), 6-way-cross connector (2), multilayer mirror (3), reference diode (4), removable collector blocker (5), gate valve (6), collector chamber (7) and sample chamber (8). Controllers for the source and motion motors, power supply, oscilloscope, and computer (9).*

Table 7.3: Information about the source and beam characterization.

Repetition rate	50 Hz.
Bandwidth	2% around 13.5 nm
Plasma produced with	Xenon gas
Spot size	Around 0.05 mm^2
Peak intensity in spot	0.19 W/cm^2
Fluence	3.8 mJ/cm^2
Energy per pulse	~1.9 µJ

The setup was built under the concept of how constantly monitor the light output of the source. The multilayer mirror is positioned in such a way that some light from the source can pass above the mirror. This light then is reflected by a smaller multilayer mirror, of the same type, onto a reference diode. Another photodiode (signal diode), of the same type as the reference diode, is

placed at the position of the sample to measure the fluence of the radiation that would arrive to the sample spot. After calibrating both diodes against each other, the radiation arriving onto the sample can always be calculated from the signal of the reference diode [87].

Figure 7.4 shows pictures of the actual setup, in ILT (Fraunhofer Institute for Laser Technology), joint lab with the Chair for Technology of Optical Systems at RWTH Aachen University. The two photos on the right side, show the holder used to perform the exposures. The circular piece is a Zr filter coupled with a scintillator to determine the position of the focal point of the beam. The small square piece is the sample placed in the custom-made holder. In the bottom picture, the sample is placed in the direction of the beam.

When the focus point position is determined with the help of a scintillator, the sample is placed in the desired position with the help of the sample station, which is located inside the measurement chamber. The sample station can move in two dimensions; left-right and in-out of focus. The sample station does not run in the vertical direction, which implies a limitation on the selection of the spots to be exposed.

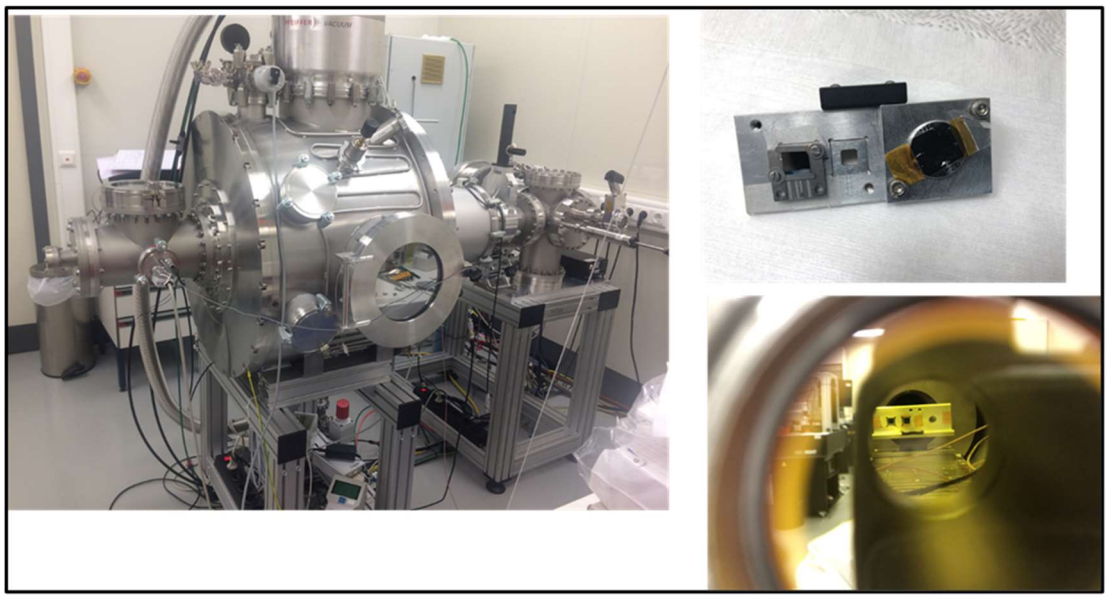

Figure 7.4: *Picture of the actual set-up located in ILT institute of Aachen University. In the top image, right side: Scintillator side by side with one of the samples. The holder allows the placement of two samples together with scintillator. In the bottom, ride side: Sample placed in the beam pass is shown.*

7.4 Results and discussion.

An infrared camera was intended to be used during the exposure of the filters in order to monitor the procedure, having the possibility to ensure the position of the beam on the sample and obtaining a mapping of temperature changes due to the radiation absorption and the infrared emission of the metal layer. Unfortunately, the infrared camera was not working during the planned experiment.

The malfunction of the infrared camera let us working blindly since we could not be secure if the beam was focused on the sample, and analysis of infrared emission was not possible. After focusing the beam using the scintillator placed next to the filter in the custom holder shown in *figure 7.4*, using a horizontal motion manipulator the sample is moved to a calculated position that should correspond to the center of the filter. From there the positions of the other two spots were located moving the manipulator 1 mm to the left and 1 mm to the right from the center.

The setup can manage only one sample each time, so opening the chamber and breaking the vacuum is necessary to place the next sample.

During the first try out of the setup for the experiment, an extra sample of around 100 nm Zr was used. The starting time of exposure was chosen 8 min, for a total dose of 91.2 J/cm^2. Unexpectedly, when the chamber was opened the filter was broken. Since there was no way to monitor the sample during exposure, we cannot be sure when it happened and what was the reason for the filter getting broken. Due to the limited number of samples available for the experiment and the limited time available for the experiment, the times of exposures were shorter than programmed, resulting, as we assume, in administrated doses below the critical dose. Furthermore, slight misalignment of the sample stage could result in sample displacement from the optimum focus position, obtained with the help of the scintillator, causing further doses reduction.

After the rounds of exposure, samples were inspected with an optical microscope, no sign of ablation or any kind of damage was possible to detect with the instrument, so, from a simple observation point, the filters are strong enough to support the doses administrated and the vibrations inside the chamber.

7.4.1 The surface chemical composition.

XPS analysis of the filters was performed before and after high-density EUV radiation exposure. Unfortunately, Zr/Nb sample (sample 4) was broken during the mounting of the sample for XPS. Because of that, we won't present XPS results taken for sample 4 before exposure, since the results are very similar to the other filters. Instead, in a collection of data presented in *table 7.3*, the comparison between the surface composition of the filters before and after the experiment is presented as well as the comparison of the control samples before and after the time of the programmed experiment. Five months are the time between the taken measurements.

As one can observe, similar to previous analysis of these kinds of filters in chapter 5, the presence of oxygen, carbon, and fluorine on the surface of these samples are characteristic. It must be remembered that the analysis reaches only between the first 5 to 8 nm into the sample's surfaces. After the radiation doses were applied, some traces of Si are found on the surface of the filters; We cannot be certain about the cause.

Table 7.3: *XPS analysis comparison of each filter before and after EUV high-density radiation exposures as well as the comparison of the control samples before and after the complete experiment.*

Sample 1, (Nb) before EUV exposure			
Elements found	Point 1 Percentages %	Point 2 Percentages %	Point 3 Percentages %
C	21.4	21.2	22.3
O	53.8	53.0	52.4
F	2.8	3.5	3.1
Nb	22.0	22.3	22.2

Sample 1, (Nb) after EUV exposure			
Elements found	Point 1 Percentages %	Point 2 Percentages %	Point 3 Percentages %
C	38.7	41.1	40.4
O	40.5	39.0	40.2
F	2.4	2.8	2.4
Nb	15.9	14.7	15.2
Si	2.5	2.3	1.8

Sample 2, (Zr) before EUV exposure			
Elements found	Point 1 Percentages %	Point 2 Percentages %	Point 3 Percentages %
C	20.4	21.2	19.8
O	47.7	46.8	45.9
F	9.5	9.8	12.5
Zr	22.4	22.2	21.8

Sample 2, (Zr) after EUV exposure			
Elements found	Point 1 Percentages %	Point 2 Percentages %	Point 3 Percentages %
C	41.0	40.9	46.0
O	31.9	32.9	29.3
F	11.2	9.6	10.3
Zr	15.3	15.8	13.5
Si	0.6	0.8	0.9

Sample 3, (Nb/Zr) before EUV exposure			
Elements found	Point 1 Percentages %	Point 2 Percentages %	Point 3 Percentages %
C	31.8	29.7	28.8
O	34.8	31.5	30.7
F	18.0	24.9	27.1
Nb	15.4	13.8	13.4

Sample 3, (Nb/Zr) after EUV exposure			
Elements found	Point 1 Percentages %	Point 2 Percentages %	Point 3 Percentages %
C	41.6	41.5	39.6
O	39.4	39.7	37.4
F	3.4	3.0	8.4
Nb	14.3	14.1	13.4
Si	1.4	1.7	1.2

Sample 5, control (Nb) before			
Elements found	Point 1 Percentages %	Point 2 Percentages %	Point 3 Percentages %
C	21.4	21.2	22.3
O	53.8	53.0	52.4
F	2.8	3.5	3.1
Nb	22.0	22.3	22.2

Sample 5, control (Nb) after			
Elements found	Point 1 Percentages %	Point 2 Percentages %	Point 3 Percentages%
C	34.5	38.3	33.1
O	44.7	42.0	45.2
F	2.1	1.8	2.4
Nb	18.1	17.3	18.7
Si	0.6	0.7	0.6

Sample 6, control (Zr) before			
Elements found	Point 1 Percentages %	Point 2 Percentages %	Point 3 Percentages %
C	20.4	21.2	19.8
O	47.7	46.8	45.9
F	9.5	9.8	12.5
Zr	22.4	22.2	21.8

Sample 6, control (Zr) after			
Elements found	Point 1 Percentages%	Point 2 Percentages %	Point 3 Percentages%
C	34.7	34.0	35.0
O	40.5	40.3	39.3
F	5.1	5.7	6.3
Zr	18.8	19.2	18.6
Si	0.9	0.9	0.7

Regarding carbon contamination, there was an increase in the percentage of carbon found on the surface of the filters after exposure but also on the control samples. In the case of the control samples, in sample 5, an average increase of 62% of carbon with respect to Nb was found and a 68.6% increase in sample 6 with respect to Zr. In the case of the samples submitted to the

exposures, there was an average increase of carbon of about 85% in sample 1 with respect to Nb; 108 % percent increase in sample 2 with respect to Zr, and only a 35 percent increase in sample 3 corresponding to Nb/Zr. Since we cannot ensure that the measurements were taken in the exact points where the doses were applied, the results are not conclusive. Furthermore, we cannot infer any relationship between the amount of dose applied and the percentage of carbon found on the surface since the increase was similar for the 3 spots on each sample. However, the results confirm the presence of stronger contamination due to carbon growth for the exposed samples.

Oxygen percentage got a reduction in the measurements after exposure in mostly all the samples, inclusive in the control samples. We could say that since XPS can detect just a few nanometers of elements on the surface, then maybe, the increase of carbon pushed for a reduction of the oxygen content at the surface, becoming part of an oxidized metal layer. A more detailed XPS is needed to be able to identify the oxidized states of the metal layers.

7.4.2 Optical characterization.

The transmittance performance of the first four samples (Nb, Zr, Nb/Zr, and Zr/Nb self-free-standing filters) was measured at BEAR Beamline before exposures to high-density EUV radiation at 13.5 nm. Four wavelengths were chosen to track the possible changes, on transmittance performance, due to exposure damage.

The samples were scan along the horizontal axis to measure transmittance at each one of the chosen wavelengths (6, 7.02, 13.5, 17) nm, taking the central point of the filter window as one reference. The second reference, to ensure the correct position of the sample, as it is mentioned before, is a blue spot located in each sample. For the measurements, the samples are positioned keeping the blue spot always in the bottom-left corner. The window of the filter is 3 mm x 3 mm in size. Using the Y manipulator, the motors of the instrument moved the samples in steps of 0.1 mm. A transmittance map of the samples, for each wavelength, is presented in *Figure 7.5.*

As we can observe from figure 7.5, the transmittance curves resulted from the measured data demonstrate certain homogeneity. We can even infer the type of etching outcome from RIE procedure. It looks like it was an isotropic etch since curves are not completely flat but kind of rounded at the edges.

The four free-self-standing filters demonstrate a remarkable performance. As it was expected from the transmittance results of Nb/Zr free-self-standing filter presented in chapter 5 the highest value of transmittance for all filters occurred at 7.02 nm. Nb presented the highest transmittance performance with 77% of transmittance for 6 nm and 7.02 nm and 65% at 13.5 nm, to our knowledge these are the highest values of transmittance for Nb free-standing filters at these wavelengths, presented so far [17]. Also, Zr filter shows good transmittance performance with 67% at 7.02, followed by Zr/Nb with 66% and at last Nb/Zr filter. Paying attention carefully to the transmittance curves of Nb/Zr, even though the results on transmittance are similar to the Nb/Zr filter characterized in chapter 5, it looks like that the Si_3N_4 membrane was not completely detached,

the convex shape of the curves is proof of the non-uniformity of the etched part showing the highest inhomogeneity of all samples. The presence of a residual Si_3N_4 membrane reduces the transmittance performance of the filter. Besides, the thicknesses of the filters deduced by fitting the measured data will explain in more detail below the results obtained. The comparison of the measured transmittance data is presented in *figure 7.6.*

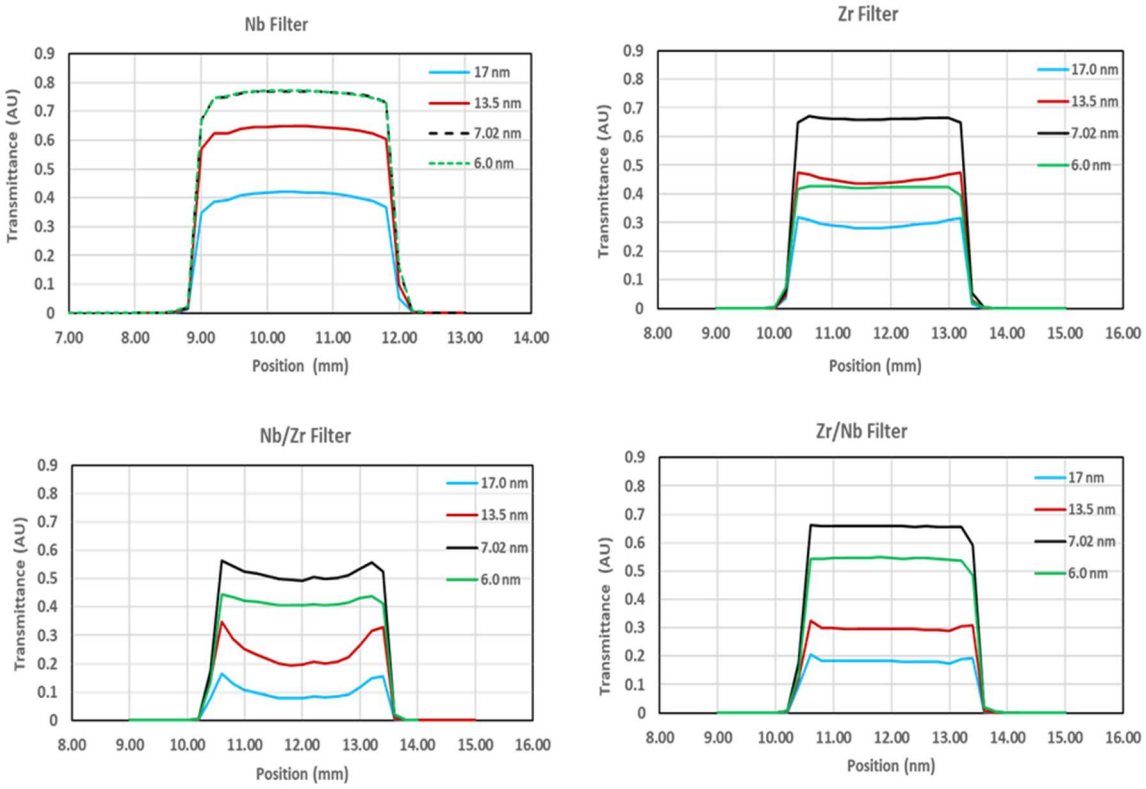

Figure 7.5: *Transmittance map of the samples, for 6 nm (green), 7.02 nm (black), 13.5 nm (red), and 17 nm (blue) wavelengths.*

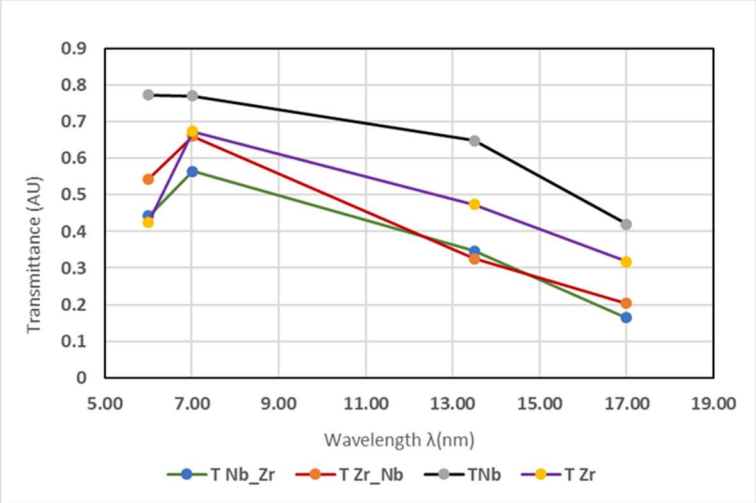

Figure 7.6: *Transmittance relation of the four samples measured at four wavelengths.*

IMD optimization algorithm was used to fit the curves of the measured data of each filter. Taking in account the results from XPS measurements of the filters before exposure, and the results from TEM analysis from similar structures studied in the last chapter: a layer of carbon was added as a top layer and layers of metal oxides were added in order to try to simulate the most realistic structures for our filters. In *figures 7.7 and 7.8* the fitted curves are shown together with the resulted proposed structure for each filter.

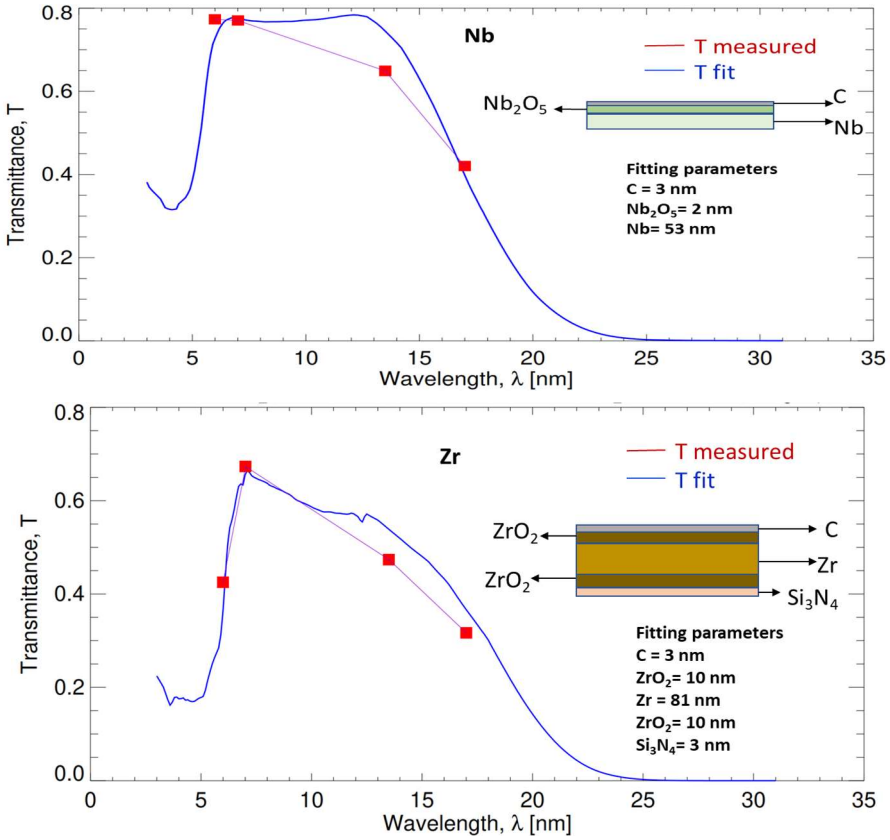

Figure 7.7: *Measured curves and fitted curves for Nb and Zr free-self-standing filter.*

Since the measured data is composed of only four points, it is very difficult to fit the curves perfectly because the degrees of freedom of the variables for the algorithm get limited. Similar to the fit for the filters in chapter 5, the carbon layer on top is always around 3 nm, and the level of oxidation of Zr is higher than that of Nb.

To find the best fit for Nb filter, *figure 7.7* top, the total thickness of the Nb layer had to depart significantly from the nominal value. The total thickness of the filter is found to be 58 nm. The optical constants used for the fitting of the measured data also influence the results. For all theoretical simulations of the measured data, values from "nk" IMD files were used as optical constants. These files cover a wide range of wavelengths and use data compiled from different databases such as the data from llnl_cxro.nk, Palik.nk, and other contributors, expanding the range from 0.124 angstroms to $3.33 \cdot 10^6$ angstroms depending on the element [88].

For Zr filter (figure 7.7 bottom), the transmittance performance was lower but the total thickness of the filter is higher in comparison with Nb filter, around 107 nm, very close to the nominal value. For the best fit of this filter a residual 3 nm Si_3N_4 membrane had to be added and oxidation of the Zr layer at the top as well at the bottom.

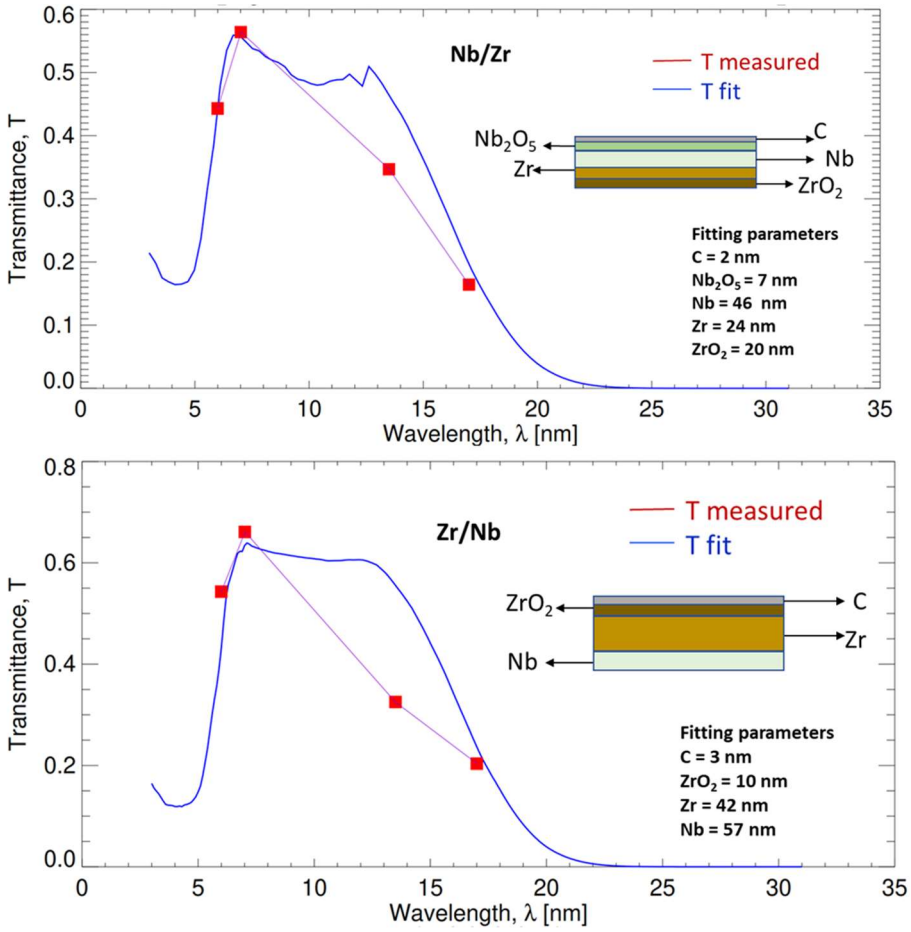

Figure 7.8 *Measured curves and fitted cures for Nb/Zr and Zr/Nb free-self-standing filter.*

In the case of Nb/Zr filter, *figure 7.8 top*, we were assuming also a residual Si_3N_4 membrane, as for the Nb/Zr filter in chapter 5, in that case since there was a broader characterization of the filter, the absorption L edge signature pointed out that possibility. But in the end, in this case there was another alternative: the best fit was achieved by assuming a completely detached membrane and as the consequence of not having it at the bottom, a layer of ZrO_2 due to the exposure to the air after the etching process. The total thickness of the best-fitted structure was about 99 nm.

For Zr/Nb filter (*figure 7.8 bottom),* different combinations of parameters were used to find the best fit of the structure, *however* fitting did not converge very nicely. There was no need of assuming a residual membrane and since Nb is in the bottom layer, and Nb oxidize in a slower rate, we did not propose an oxidized layer at the bottom, but just and oxidized layer of Zr on the top.. The total fitted thickness was about 112 nm.

As we mentioned before, the re-characterization of the filter after EUV exposures was not possible by the time of writing this thesis. Those measurements are necessary to determine any reduction of the transmittance performance of the filter due to the exposure. A better way to track the position of the exposure spot is also necessary in order to ensure the reliability of the results.

7.5 Conclusion

- The doses applied are possibly far from the critical doses where the filters can present any visible damage.
- The experiment could be extended to applying higher doses of radiation and then re-characterizing the samples.
- An infrared camera or another way to monitor the samples during exposure is needed to ensure the position of the exposure spots.
- The fitting of the measured transmittance data suggests that Nb filter is thinner than expected. Furthermore, even though e-beam deposition technique seems to achieve more mechanically stable filters, magnetron sputtering has better control on the target thicknesses of the layers.
- XPS results are not conclusive because even though the increase of the percentage of carbon contamination is mostly higher in the samples that were exposed, we are not able to ensure that the positions of the XPS measurements are the same as the exposure spots.
- Because during the exposure of the samples there was no additional Zr filter to suppress out-of-band radiation, which was used for the characterization of the beam, and due to an uncertainty regarding the best focus position and spot size, it is not possible to determine exact dose on each spot. The dose is however large enough to result in some contamination on the exposure spots, which was, in some way, confirmed by XPS measurements.

Chapter 8.

Conclusion, recommendations, and future work.

During the long way of this project, and from all the results obtained, several conclusions can be addressed.

Thin-film filters are used in all kinds of short-wavelength sources, such as plasma-based sources and synchrotron radiation-based sources. Thin-film transmittance filters are needed to ensure the quality of the beam delivered from those sources. In the EUV, materials have broad absorption, so good candidate materials are limited. Furthermore, the properties of the radiation delivered from high-brilliance sources (high peak power and short pulses), like FELs, demand not only a good transmittance performance of the filters but also thermal, mechanical, and chemical stability when exposed to this kind of radiation. Taking into account all of those considerations, the selection of materials for the fabrication of the filters is not a trivial task.

In our case, we found that Nb and Zr are the best candidates for the fabrication of free-standing thin-film filters. Studying the properties of these two materials and analyzing the simulation of their transmittance performance, we conclude that the combination of Nb and Zr in bilayer structure filters was the best option for filters in the range from 4.5 to 20 nm. For the project, we studied the properties not only of the bilayer structure but also of the monolayer filters as well. A more careful etching procedure is needed to achieve the optimized performance of this bilayer structure.

During the fabrication steps, differences in the quality of the filters were noticed depending on the deposition technique used, at least for Zr and Zr/Nb filters. These two types of filters, when they were fabricated using sputtering deposition techniques, presented compressive stress featured by a wrinkled surface. They resulted in very fragile structures, to survive the etching procedure. It is possible that the quick oxidation of Zr, during or after deposition, is the cause of the fragility of those filters, taking into account that sputtering takes a considerably longer time than e-beam evaporation and in those combinations, Zr is on top, where it is always exposed to air.

When e-beam evaporation was used, all samples were strong enough to survive the etching procedure; but again, even though after deposition all samples presented flat smooth surfaces, after etching Zr and Zr/Nb samples became wrinkled showing apparent signs of compressive stress.

Nb and Nb/Zr samples presented flat and smooth surfaces and were strong enough to survive the etching procedure, even when they were fabricated using the sputtering technique. In this case, when they were fabricated with magnetron sputtering; after being etched, the filters also featured compressive stress with wrinkled surfaces. This was not the case when Nb and Zr were fabricated using e-beam deposition techniques; Samples remained flat and smooth even after etching. On the other hand, magnetron sputtering offers more control over the thicknesses of the deposited layers, besides that, for the fabrication of these filters, the e-beam technique is preferred.

Self-standing Zr, Nb, Nb/Zr, and Zr/Nb filters have been achieved. The transmittance performance of all four kinds of filters was characterized before etching, as is presented in chapter 4. However, for the limited time during the synchrotron measurements campaign, we presented only the results of the full characterization of our Nb/Zr self-standing filter, with the highest peak of transmittance of 60 % at 7.02 nm, which represent excellent results. We also presented the remarkable results of the transmittance measurements, at four wavelengths, of the achieved self-standing filters fabricated using e-beam evaporation. Due to the imperfection of the etching procedure for some of the samples, the results are not all as expected. Nb presented the best performance, with a transmittance of about 77% at 6 nm and 7.02 nm and about 65% at 13.5 nm. For Zr filter, the peak transmittance, for the wavelengths measured, was 67% at 7.02 nm. In the case of Zr/Nb filter it is 66% at 7.02 nm. In the case of Nb/Zr, the possible oxidation of the bottom layer after the detachment of the membrane reduced the transmittance of the filter. But even with the reduction of its performance due to this problem, the filter achieved around 56% of transmittance at 7.02 nm, very similar to the value obtained before; It is possible to let around 2 nm residual membrane to protect the bottom layer from oxidation and improve the transmittance, but a very precise etching process needs to be carried on.

Plasma source- based on gas puff target, coupled with a spectrometer set up, was also used to measure the transmittance performance of the samples. It resulted in a suitable technique, but only when high accuracy of the measurements is not needed. It is a time-saving method compared with synchrotron beamlines. Higher accuracy could be achieved with the proper characterization of the source, also the development of better analysis code, using better approximations for the grating equation, is needed to analyze the obtained spectrum data. This is part of our future work!

The structural analysis of the samples revealed that two different crystal structures were preferred by Zr (hcp and fcc) both with multiple crystal orientations. In the case of Nb, only bcc Nb was found in the respective analyzed samples. Results are in agreement with the results obtained by XRD. Both Zr and Nb presented a certain level of oxidation when they were the top layer, but while Zr presented about 10 nm of the oxidized layer, Nb only had around 3-4 nm. Samples were fabricated both the same day. The oxidation of Zr has resulted in some expansion of the Zr layer, while on Nb layer was not noticed any expansion by the time of the analysis.

XPS analysis of the samples found Oxygen, Carbon, and some Fluoride contamination on the surface of the samples. Also, EDX analysis showed oxygen contamination and carbon contamination in some layers. Carbon contamination is very common in this type of optical devices. EDX showed no interdiffusion between the interfaces of Nb and Zr. HRSTEM showed that the lattice parameters of the samples are larger than those predicted by the theoretical model used. If the oversize is due to the different lattice size of the elements in the bilayers, intrinsic stress could be the cause of the fragility of some samples.

For the study of the radiation damage of the filters, samples have been exposed to high EUV doses in a setup based on a plasma source. No visible damage could be appreciated with the doses

applied. It would be recommendable to repeat the experiment in a free-electron laser source; increasing the applied doses, looking for finding the critical doses for each type of filter, and the single-shot damage threshold. This could be pursued as future work.

Since samples are sensitive to oxidation, it is recommended to perform the in-situ deposition of a protective coated layer to avoid the progressive oxidation of the filter and ensure a longer lifetime.

Appendix A

MATLAB code created to process transmittance data obtained during the measurement campaign in the Military University of Technology; Warsaw, Poland.

```
%Analysis of Transmittance Data.
 % The code is used to obtain the transmittance spectrum of the filters from the spectrogram produced by the measurements performed with the coupled spectrometer-CCD camera transmittance setup.
The code returns a plot of Transmittance vs. wavelength.


 %First Step, Working with Direct.

Data =imread('name signal file.tif');
Bkground= imread('name background signal file.tif');
Sample = Data-Bkground;
% eliminating the noise background from data.

 Sample = double(Sample);
 %making data easier to manage.
figure
image(Sample)

% For finding the position of the max value on the matrix the next three
% steps have to be used together.

 G= sum(abs(gradient (sum(Sample,2))));

test = G(Sample);

f=@(ang)Rot(ang, Sample);

angle = fminsearch(f, 1);

sample_opt = imrotate(Sample, angle);
figure;
imagesc (Sample);
figure;
imagesc (sample_opt);
```

```
function rough = Rot(ang, img)
rough= -G(imrotate(img, ang));
end

function rms = G(img)
rms=sum(abs(gradient (sum(img,2))));
end
  Sample (:);
 % Use the column representation of my matrix to find max value

 [~,I]= max(sum((Sample),2));
 % Return max Value and index


 x = 1:size(Sample,1);
%defining position of the axe X

 y = 1:size(Sample,2);
%defining position of the axe Y

imagesc(y,x-I,Sample,[0 20000]);
 %relocation of zero position and limiting contrast.
% value of contrast must change depending on the image
colorbar;

i1=x<I;
 % Evaluating which part from the maximum is larger, upper

 i2=x>I;
% part or lower part.

 a=sum(sum(Sample(i1,:)));
 b=sum(sum(Sample(i2,:)));

 if (a-b>=0)
 % condition deciding what part to take.

S = Sample(i1,:);
else
S = flipud(Sample(i2,:));
```

```
end
imagesc(S,[0 20000]);

 CutS= S(1:800,1027:1036);
% clipping S to use a selected part of data to be analyzed

Direct= sum((CutS),2)/10;
%average.
pixel= 13000;

x= (1:size(S,1))* pixel;
%Calibration from Pixel to Wavelength

lamda= flipud((x(end-799:end)*(0.0000023))');
 % lines calibrations are (799) is different for each sample, depending of the image of the spectrum.

figure;
plot(lamda,Direct);

% % Second Step: Doing the same procedure for the Filter sample.

Dataf =imread('filter.tif');
Bkgroundf= imread('bckg filter.tif');
Samplef = Dataf-Bkgroundf;

Samplef = double(Samplef);

Samplef (:);
[~,I]= max(sum((Samplef),2));

xf = 1:size(Samplef,1);
yf = 1:size(Samplef,2);
imagesc(yf,xf-I,Samplef,[0 10000]);
colorbar;

i1f=xf<I;
i2f=xf>I;
a=sum(sum(Samplef(i1f,:)));
b=sum(sum(Samplef(i2f,:)));
if (a-b>=0)
```

```
Sf = Samplef(i1f,:);
else
Sf = flipud(Samplef(i2f,:));
end
imagesc(Sf,[0 10000]);
colorbar;

CutSf= Sf(1:800,1037:1046);
Filter= sum((CutSf),2)/10;
pixel= 13000;

xf= (1:size(Sf,1))* pixel;

lamda2= flipud((xf(end-799:end)*(0.0000023))');
 % values are selected manually depending on the spectrum of each sample.

figure;
plot(lamda2,Filter
plot(lamda,Direct,'r', lamda2,Filter, 'b');

T=(Filter/Direct);
%Transmission calculation

plot(lamda,T);
```

Appendix B

Uncertainty Analysis

It is very important in every experimental research to evaluate and express the uncertainties of the results derived from the measurements. The uncertainty of a measurement is a quantification of the doubts about the measurement results.

The uncertainties come from errors. They are two types of errors: systematic or random (statistical). These two types of errors are connected to the concepts of accuracy and precision. A repeatable (precise) measurement is one where the spread of results is 'small', while an accurate measurement is one in which the result is in agreement with the 'true value'.

The uncertainty of a single measurement is limited by the precision of the measuring instrument, along with any other factors that might affect the ability of the experimenter to make the measurement and it is up to the experimenter to estimate the uncertainty [89].

Synchrotron Measurements [BEAR]

To obtain the transmittance T of a sample at a certain photon energy E_{ph} and incidence angle θ (in our case normal incident beam), It is required to monitor the followings identities: Transmitted intensity, direct beam intensity (without the sample in the beam path), and two intensity monitor readings that correct the instability of the beam with time. These intensity pairs are measured by the photocurrent responses of the photodiode and refocusing mirror respectively.
Since the transmittance measurements were performed at normal incidence and a surface scan was performed to take the measurements at the center of each sample, we will neglect the possible uncertainties derived from the alignment of the sample, and we will focus in the calculation of the systematic error derived from instrumental uncertainties.

The transmittance T has been evaluated using 2 different normalizations: using mirror current and the sum of the 4 BPM (beam position monitor) currents. In the 2 cases, the transmittance is given by:

$$T = \left(\frac{I - I_{dark}}{I_{m,BPM} - I_{m,BPM\ dark}}\right) \Big/ \left(\frac{I_0 - I_{dark}}{I_{m,BPM} - I_{0m,BPMdark}}\right)$$

The instrumental error analysis has been done by measuring 1000 times at the same energy the following quantities:

I: Transmitted intensity (diode signal).

I_m: $Transmitted\ intensity\ monitor$ ($refocusing\ mirror\ drain\ current\ -\ sum\ of\ BPM\ current$).

I_0: Incident intensity (diode signal).

I_{0m}: Incident intensity from the monitor ($refocusing\ mirror\ drain\ current\ -\ sum\ of\ BPM\ current$).

I_{dark}: The dark of the transmitted signal.

I_{dark0}: The dark of the incident signal.

$I_{m,BPM\ dark}$: The dark of the transmitted monitor signal.

$I_{0m,BPMdark}$: The dark of the incident monitor signal.

The error was analyzed with a model in which the diode intensity and the monitor intensity are not separated. The dark error was considered as a constant. Under those conditions, the error is given by:

$$\frac{\Delta T}{T} = \frac{\Delta\left(\frac{I - \overline{I_{dark}}}{I_{m,BPM} - \overline{I_{m,BPM\ dark}}}\right)}{\left(\frac{I - I_{dark}}{I_{m,BPM} - \overline{I_{m,BPM\ dark}}}\right)} + \frac{\Delta\left(\frac{I_0 - \overline{I_{dark0}}}{I_{m,BPM} - I_{0m,BPMdark}}\right)}{\left(\frac{I_0 - \overline{I_{dark0}}}{I_{m,BPM0} - I_{m,BPMdark}}\right)}$$

For each energy, the diode current, the mirror current and the sum of bpm were analyzed. Each region used in the measurements has been evaluated using the ranges of the instruments used for the measurements. The distribution of the measurements and the dark was fitted using a Gaussian curve. The standard deviation σ of the distribution is considered the error.

The transmittance measurements were performed using a G1200 (1200 ll/mm) grating, the measurements were divided in five energies regions depending on the filter used to cover each range. The total extended range is from around 3.02 nm to approximately 29.52 nm (42-410) eV. The results are shown in table B1. The analysis of single measurement by region has been used to estimate the error percentage in transmittance and to plot the results in Figure B.1.

Region	Energy regions (eV)	Relative error by region
1	40 - 75	1.9391560e-03
2	70 - 102	2.8923039e-03
3	98 - 200	1.0996316e-03
4	190 - 300	1.0996316e-03
5	290 - 420	7.9762806e-03

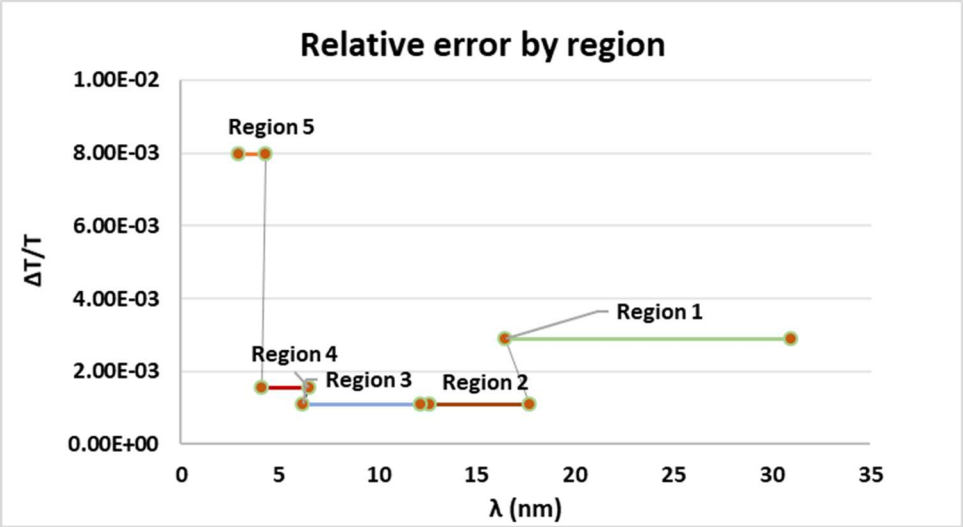

Figure B.1: *transmittance relative error by wavelength region.*

Instrumental uncertainty represents the accuracy of the ammeter readings and can be calculated using the tool specifications provided by the manufacturer. The error is given by ± [gain error + offset error]. For the photocurrent measurement, a multimeter Keithley Model 6517A was used and for the ranges of photocurrent used depending on the energy region the relative error was about 0.2%.

Since the measurements were performed at normal incidence and the samples were placed in an especial holder custom made to fit the measurements chamber buildup holder, the total relative uncertainty of the transmittance measurements was around 1%, neglecting the samples alignment error.

Bibliography

[1] *M. Hatayama et al. High-Transmittance Free-Standing Aluminum Extreme Ultraviolet Filter Jpn. J. Appl. Phys.* ***48*** *122202. (2009).*

[2] *E. Gann, A. T. Young, B.A. Collins, H. Yan, J. Nasiatka, H.A. Padmor, H. Ade, A. Hexemer, C. Wang. Soft x-ray scattering facility at the Advanced Light Source with real-time data processing and analysis. Review of Scientific Instruments 83, 045110 (2012).*

[3] *Y. Saitoh, H. Kimura, Y. Suzuki, T. Nakatani, T. Matsushita, T. Muro, T. Miyahara, M. Fujisawa, K. Soda, S. Ueda, H. Harada, M. Kotsugi, A. Sekiyama, and S. Suga. Performance of a very high-resolution soft x-ray beamline BL25SU with a twin-helical undulator at SPring-8. Review of Scientific Instruments 71, 3254 (2000).*

[4] R. *Wayne, M. Mossessian, D. Mossessian. Efficiency and stray light measurements and calculations of diffraction gratings for the Advanced Light Source. Review of Scientific Instruments 66, 2160 (1995).*

[5] *J.H. Underwood, E.M. Gullikson, High-resolution, high-flux, user-friendly VLS beamline at the ALS for the 50– 1300 eV energy region, Journal of Electron Spectroscopy and Related Phenomena 92, 265–272 (1998).*

[6] *F. Bencivenga, S. Baroni, C. Carbone, M. Chergui, M. B. Danailov, G. De Ninno, M. Kiskinova, L. Raimondi, C. Svetina and C. Masciovecchio. Nanoscale dynamics by short-wavelength four-wave mixing experiments, New Journal of Physics 15 (2013).*

[7] *P.G. O'shea, H.P. Freud, Free-electron lasers: status and applications, Science 292, 1853, (2001).*

[8] *C.J. Bocchetta et al. FERMI@Elettra Conceptual Design Report, 2007. Technical Report ST/F-TN-07/12, Sincrotrone Trieste.*

[9] *M. Zangrando, D. Cocco, C. Fava, S. Gerusina, R. Gobessi, N. Mahne, E. Mazzucco, L. Raimondi, L. Rumiz and C. Svetina. Recent results of PADReS, the Photon Analysis Delivery and Reduction System, from the FERMI FEL commissioning and user operations. J. Synchrotron Rad. 22, 565-570, (2015).*

[10] *C. Tarrio, R. F. Berg, T. B. Lucatorto, B. Lairson, H. Lopez, & T. Ayers. Thermally stable thin-film filters for high-power extreme-ultraviolet applications, The Review of Scientific Instruments, 86(11), 116103 (2015).*

[11] *F. R. Powell, Care and Feeding of Soft X-Ray and Extreme Ultraviolet Filters, Laser-Induced Damage in Optical Materials, SPIE Proc. 1848, 503. (1992).*

[12] *S. B. Hill, N. S. Faradzhev, L. J. Richter, S. Grantham, C. Tarrio, T. B. Lucatorto, S. Yulin, M. Schürmann, V. Nesterenko, T. Feigl. Optics contamination studies in support of high-throughput EUV lithography tools, Proc. SPIE 7969, Extreme Ultraviolet (EUV) Lithography II, 79690M. (25 March 2011).*

[13] *H.A. Macleod. Thin-film Optical Filters, Institute of Physics Publishing, Bristol and Philadelphia, (2001).*

[14] *F. R. Powell, T. A. Johnson. Filter windows for EUV lithography, Proc. SPIE 4343, Emerging Lithographic Technologies V, (20 August 2001).*

[15] *S. Brose, S. Danylyuk, L. Juschkin, C. Dittberner, K. Bergmann, J. Moers, G. Panaitov, (...), D. Grutzmacher. Broadband transmission masks, gratings and filters for extreme ultraviolet and soft X-ray lithography, Thin Solid Films, 520 (15), pp. 5080-5085, (2012).*

[16] *Slemzin, V.A., Goryaev, F.F. & Kuzin, S.V. Spectroscopic diagnostics of the solar coronal plasma. Plasma Phys. Rep. (2014) 40: 855.*

[17] *N. I. Chkhalo, M. N. Drozdov, E. B. Kluenkov, S. V. Kuzin, A. Ya. Lopatin, V. I. Luchin, N. N. Salashchenko, N. N. Tsybin, and S. Yu. Zuev, "Thin-film multilayer filters for solar EUV telescopes," Appl. Opt. 55, 4683-4690 (2016).*

[18] *T. A. Johnson, R. Soufli, E. M. Gullikson, M. Clift. Zirconium and niobium transmission data at wavelengths from 11-16 nm and 200-1200 nm. Proc. SPIE 5538, Optical Constants of Materials for UV to X-Ray Wavelengths, (14 October 2004).*

[19] *D. L. Windt, W. C. Cash, M. Scott, P. Arendt, B. Newnam, R. F. Fisher, and A. B. Swartzlander, Optical constants for thin films of Ti, Zr, Nb, Mo, Ru, Rh, Pd, Ag, Hf, Ta, W, Re, Ir, Os, Pt, and Au from 24 Å to 1216 Å, Appl. Opt. 27, 246-278, (1988).*

[20] *Y. Wu, L. Zhang, H. Cao, X. Zheng, H. Jiao, and L. Chen. Preparation and Characterization of Free-Standing Zr Filter for Soft X-ray Laser Application, in Optical Interference Coatings, OSA Technical Digest (CD), Optical Society of America, (2007).*

[21] *N. I. Chkhalo, M. N. Drozdov, S. A. Gusev, E. B. Kluenkov, A. Ya. Lopatin, V. I. Luchin, N. N. Salashchenko, L. A. Shmaenok, N. N. Tsybin, B. A. Volodin. Freestanding multilayer films for application as phase retarders and spectral purity filters in the soft x-ray and EUV ranges, Proc. SPIE 8076, EUV and X-Ray Optics: Synergy between Laboratory and Space II, 80760O (4 May 2011).*

[22] *V.P. Belik, Y.M. Zadiranov,, N.D. Il'inskaya, et al. Free-standing optical filters for a nanolithography source operating in the 12–15 nm wavelength range, Tech. Phys. Lett. 33: 508, (2007).*

[23] *H. Wu, Y. Wu, G. Lv, Z. Wang, L. Ling, Z. Xia, N. Chen. Preparation and characterization of free-standing Zr, PI and Zr/PI filter, Proc. SPIE 7995, Seventh International Conference on Thin Film Physics and Applications, 79951F (18 February 2011).*

[24] *D. Attwood. Soft X-rays, and extreme ultraviolet radiation, (1999).*

[25] *E. Allaria, L. Badano, S. Bassanese, F. Capotondi, D. Castronovo, P. Cinquegrana, M.B. Danailov, G. D'Auria, A. Demidovich, R. De Monte, G. De Ninno, S. Di Mitri, B. Diviacco, W.M. Fawley, M. Ferianis, E. Ferrari, G. Gaio, D. Gauthier, L. Giannessi, F. Iazzourene, G. Kurdi, N. Mahne, I. Nikolov, F. Parmigiani, G. Penco, L. Raimondi, P. Rebernik, F. Rossi, E. Roussel, C. Scafuri, C. Serpico, P. Sigalotti, C. Spezzani, M. Svandrlik, C. Svetina, M. Trovó, M. Veronese, D. Zangrando, M. Zangrando, The FERMI free-electron lasers, J. Synchrotron Radiat. 22 485–491. doi:10.1107/S1600577515005366, (2015).*

[26] *T. Ishikawa. Accelerator-based X-ray sources: Synchrotron radiation, X-ray free electron lasers and beyond. Phil. Trans. R. Soc. A377: 20180231, (2019). https://doi.org/10.1098/rsta.2018.0231.*

[27] *Free-electron lasers Peter Schmuser ¨ Institut fur Experimentalphysik, Universit ¨ at Hamburg, Germany. https://cds.cern.ch/record/941330/files/p477.pdf*

[28] *X-ray free-electron lasers: An introduction to the physics and main characteristics. P. Musumeci Department of Physics and Astronomy, UCLA. https://www.bioxfel.org/science/resources/397/download/X-ray_FELs_lecture_Musumeci.pdf.*

[29] *V. Bakshi. Status Report on EUV Source Development and EUV Source Applications in EUVL. IEEE XPLORE/document/5760393, (2007).*

[30] *C. Pellegrini, and J. Stöhrr. X-Ray Free Electron Lasers: Principles, Properties and Applications. Nuclear Instruments and Methods in Physics Research Section A: Accelerators, Spectrometers, Detectors and Associated Equipment, Volume 500, Issues 1–3, Pages 33-40, ISSN 0168-9002, (2003). https://doi.org/10.1016/S0168-9002(03)00739-3.*

[31] *F. Parmigiani, D. Ratner. Seeded Free-Electron Lasers and Free-Electron Laser Applications, Synchrotron Radiation News, 29:3, 2-3, (2016). DOI: 10.1080/08940886.2016.1174035.*

[32] R. K. Lam *et al.* Soft X-Ray Second Harmonic Generation as an Interfacial Probe. Phys. Rev. Lett. **120**, 023901, (2018). – DOI: https://doi.org/10.1103/PhysRevLett.120.023901.

[33] *D.L. Windt. IMD - Software for modeling the optical properties of multilayer films, Computers in Physics, 12, (4), pp. 360-370 (1998).*

[34] *D.L. Windt. IMD, Version 5, Installation and User's Manual', in Editor (Ed.) ^(Eds.): 'Book IMD, Version 5, Installation, and User's Manual, (2013).*

[35] *M.A. Monclús, M. Callisti, T. Polcar, L.W. Yang, J. Llorca, J.M. Molina-Aldareguía. Selective oxidation-induced strengthening of Zr/Nb nanoscale multilayers, Acta Materialia, 122, 1-10, (2017).*

[36] *http://www.samaterials.com/content/147-what-are-the-applications-of-niobium,-by Stanford Advanced Materials | May 17, (2017).*

[37] Chemical properties of niobium *https://www.lenntech.com/periodic/elements/nb.htm.*

[38] *Zirconium (Zr) Properties and Applications https://www.azom.com/article.aspx?ArticleID=1190.*

[39] *M. Ohring. The materials science of thin films, (1992).*

[40] *K. Wasa and S. Hayakawa, Handbook of sputter deposition technology: principles, technology, and applications (1992).*

[41] *S. M. Rossnagel, J.J.Cuomo and W.D. Westwood, Handbook of plasma processing technology: Fundamentals, etching, deposition, and surface interactions, (1990).*

[42] *R.F. Bunshah, Deposition technologies for films and coatings: Developments and applications, (1982).*

[43] *W. Kern. Thin film processes I, Academic Press, (2012).*

[44] *M. Suman. Studio dell'interazione della radiazione elettromagnetica con strutture nanometriche per lo sviluppo di ottiche, (2009).*

[45] *A. Baptista, F. Silva, J. Porteiro, J. Míguez, G. Pinto. Sputtering Physical Vapour Deposition (PVD) Coatings: A Critical Review on Process Improvement and Market Trend Demands. Coatings , 8, 402, (2018).*

[46] *G. Binnig, C. F. Quate, and Ch. Gerber. Atomic Force Microscope. Phys. Rev. Lett., 56:930 933, (Mar 1986).*

[47] *T. L. Alford, L. C. Feldman, and J. W. Mayer. Fundamentals of nanoscale film analysis [E-Book], (2007).*

[48] *http://www.genplot.com/rump/index.htm.*

[49] *L.R. Doolittle, Nucl. Instrum. Methods B 9, 344, (1985).*

[50] *PDF-database. JCPDS, International center for diffraction data (ICDD), 1601 Park Lane, Swarthmore, PA 19081, USA*

[51] *D.K. Smith, R. Jenkins. The Rigaku Journal 6, (1989).*

[52] *R. Erni et al. Atomic-Resolution Imaging with a Sub-50-pm Electron Probe. In: Phys. Rev. Lett. 102.9 p. 096101, (Mar. 2009). DOI: 10.1103/PhysRevLett. 102.096101.*

[53] *M. Sardela. Practical Materials Characterization,[E-Book], (2014).*

[54] *D.B. Williams, C. B. Carter. Transmission Electron Microscopy. Boston, MA: Springer US, ISBN: 978-0-387-76500-6, (2009). DOI: 10.1007/9780-387-76501-3.*

[55] *https://chem.libretexts.org/Courses/Franklin_and_Marshall_College/Introduction_to_Materials_Characterization_-_CHM_412_Collaborative_Text/Electron_and_Probe_Microscopy/Transmission_electron_microscopy_(TEM)%3A_TEM_versus_STEM_and_HAADF.*

[56] *T. Walther. Microscopy Methods in Nanomaterials Characterization, chapter 4, edited by S. Thomas, R. Thomas, A. K. Zachariah, R. Kumar. Elsevier, volume 1, (2017).*

[57] *Ernst Ruska-Centre for Microscopy and Spectroscopy with Electrons (ER-C) et al. (2016). FEI Helios NanoLab 400S FIB-SEM. Journal of large-scale research facilities, 2, A60. http://dx.doi.org/10.17815/jlsrf-2-106.*

[58] *Ernst Ruska-Centre for Microscopy and Spectroscopy with Electrons FEI Tecnai G2 F20. Journal of large-scale research facilities, 2, A77. (2016). http://dx.doi.org/10.17815/jlsrf-2-138.*

[59] *J.B. Lumsden, X-ray Photoelectron Spectroscopy, materials characterization, (1986).*

[60] *H. Fiedorowicz, A. Bartnik, R. Jarocki, R. Rakowski, M. Szczurek. Enhanced x-ray emission in the 1-keV range from a laser-irradiated gas puff target produced using the double-nozzle setup, Appl. Phys. B 70, pp. 305, (2000).*

[61] *H. Fiedorowicz, A. Bartnik, H. Daido, I. W. Choi, M. Suzuki, S. Yamagami. Strong EUV emission from a double-stream gas puff target irradiated with a Nd:YAG laser, Optics Communications 184, pp. 161, (2000).*

[62] *A. A. Sokolov, F. Eggenstein, A. Erko, R. Follath, S. Künstner, M. Mast, J. S. Schmidt, F. Senf, F. Siewert, T. Zeschke, F. Schäfers. An XUV optics beamline at BESSY II, Proc. SPIE 9206, Advances in Metrology for X-Ray and EUV Optics V, 92060J (5 September 2014).*

[63] *S. Nannarone, et al. The BEAR Beamline at Elettra, AIP Conf. Proc. 705, 450, (2004).*

[64] *L. Pasquali, et al. The UHV Experimental Chamber for Optical Measurements (Reflectivity and Absorption) and Angle-Resolved Photoemission of the BEAR Beamline at ELETTRA, AIP Conf. Proc. 705, 1142 (2004).*

[65] *A. Lyapin, L. P. H. Jeurgens, P. C. J. Graat, and E. J. Mittemeijer. The Initial, Thermal Oxidation of Zirconium at Room Temperature, Journal of Applied Physics 96 (12), 7126-7135, (2004).*

[66] *R.J. Drese, M. Wuttig. In situ stress measurements in zirconium and zirconium oxide films prepared by direct current sputtering, J. Appl. Phys. 99 (12) 0–5, (2006).*

[67] *K. Sokhey, S. Rai, and G. Lodha, Oxidation studies of niobium thin films at room temperature by X-ray reflectivity, Appl. Surf. Sci. vol. 257, no. 1, pp. 222–226, (2010).*

[68] *C.T. Wu. Intrinsic Stress of Magnetron-Sputtered Niobium Films, Thin Solid Films, vol. 64, pp. 103-110, (1979).*

[69] *P. Prabhat, T. Erdogan, Semrock, Inc., A Unit of IDEX Corporation. Measurement of Optical Filter Spectra, Semrock Technical Notes Series. www.semrock.com/measurement-of-optical-filter-spectra.aspx.*

[70] *https://www1.columbia.edu/sec/itc/ee/test2/pdf%20files/silicon%20basics.pdf.*

[71] *M. Hellenbrandt. The Inorganic Crystal Structure Database (ICSD)—Present and Future, Crystallography Reviews, 10:1, 17-22, (2004). DOI: 10.1080/08893110410001664882.*

[72] *S. Kittiwatanakul, N. Anuniwat, N. Dao, S. A. Wolf, J. Lu. Surface morphology and superconductivity of Nb thin films by biased target ion beam deposition, Journal of Vacuum Science & Technology A **36**, 031507, (2018). https://arxiv.org/ftp/arxiv/papers/1708/1708.03380.pdf.*

[73] *A. M. Valente-Feliciano. NB FILMS: SUBSTRATES, NUCLEATION & CRYSTAL GROWTH. Proceedings of SRF, Chicago, IL USA, (2011). https://accelconf.web.cern.ch/accelconf/SRF2011/papers/tuiob06.pdf.*

[74] *F.G.R. Freitas. A.G.S. Conceição, R. Hübler, G. Soares, E.R. Vitória, R.G. Carvalho, and E.K. Tentardini. Structural and Mechanical Properties of ZrSiN Thin Films Prepared by Reactive Magnetron Sputtering. 21º CBECIMAT - Congresso Brasileiro de Engenharia e Ciência dos Materiais, Cuiabá, MT, Brasil, (09 to 13 of November 2014). http://www.metallum.com.br/21cbecimat/CD/PDF/107-001.pdf.*

[75] *A. Hojabri, J Theor Appl Phys, 10:219, (2016). https://doi.org/10.1007/s40094-016-0218-8.*

[76] *J. Schindelin, I. Arganda-Carreras, E. Frise, et al. Fiji: an open-source platform for biological-image analys, Nature methods 9(7): 676-682, PMID 22743772 (2012). DOI:10.1038/nmeth.2019.*

[77] *D. B. Williams, C. B. Carter. Transmission Electron Microscopy, A Textbook for Materials Science. Chapter 11, Springer, second edition, (2009).*

[78] *RSC Adv. 5, 36129, (2015).*

[79] *B. Varghese, S. C. Haur, C. T. Lim. J. Phys. Chem. C, 112, 10008–10012, (2008).*

[80] *Z. Wang, Y. Hu, W. Wang, X. Zhang, B. Wang, H. Tian, Y. Wang, J. Guan, H. Gu. Fast and highly-sensitive hydrogen sensing of Nb2O5 nanowires at room temperature, International journal of hydrogen energy, , 37, 4526–4532. (2012).*

[81] *P. George, V. Pol and A. Gedanken. Synthesis and characterization of Nb2O5@C core-shell nanorods and Nb2O5 nanorods by reacting Nb(OEt)5 via RAPET (reaction under autogenic pressure at elevated temperatures) technique. Nanoscale Res. Lett. 2, 17–23, (2007).*

[82] *W. Hu, Y. Mi, D. Tian, Y. Zhao, Z. Liu, K. Yo, and Y. Zhu. Synthesis of three-dimensional Nb2O5/NbS2 cabled networks. Mater. Chem. Phys. 109, 184–188, (2007). https://doi.org/10.1016/j.matchemphys.2007.11.026.*

[83] *H. Luo, M. Wei and K. Wei, J. Synthesis of Nb2O5 nanorods by a soft chemical process, Nanomater, 2009(35), 1– 4, (2009).*

[84] *Laser Induced Damage in Optical Materials, edited by Detlev Ristau, Chapter 17, Taylor & Francis Group, ISBN 13: 978-1-4398-7217-8. (2015).*

[85] *I. A. Makhotkin et al. Experimental study of EUV mirror radiation damage resistance under long-term free-electron laser exposures below the single-shot damage threshold. J Synchrotron Radiat. 25(Pt 1):77-84, (2018). doi:10.1107/S1600577517017362*

[86] *M. Benk, "Charakterisierung einer EUV-Strahlungsquelle," Fraunhofer Institute for Laser Technology ILT, (Jan. 2011).*

[87] *O. Hofmann. Optical Design and Experimental Realisation of a high Flux Setup for Measurements of Absolute Conversion Efficiency and Degradation of Luminophores in the Extreme Ultraviolet, Master Thesis, RWTH Aachen. (2016).*

[88] *http://www.rxollc.com/idl/old/imd/A.1.html.*

[89] *Measurements and Error Analysis, Copyright ©, Advanced Instructional Systems, Inc. and the University of North Carolina. (2011). https://www.webassign.net/question_assets/unccolphysmechl1/measurements/manual.html.*